Institut für Materialphysik im Weltraum

Annual Report 2016

DLR

Institut für Materialphysik im Weltraum

Deutsches Zentrum für Luft- und Raumfahrt

Annual Report 2016

Impressum:
Institut für Materialphysik im Weltraum
Deutsches Zentrum für Luft- und Raumfahrt (DLR)
51170 Köln

Tel. +49 2203 601 2331
Fax: +49 2203 61768
e-mail: materialphysik@dlr.de

Cover image: MAPHEUS 06 sounding rocket fully rigged and ready for lift-off waiting for launch in ESRANGE's Skylark tower. Umbilicals provide cooling, vacuum, power and communication to the scientific payload until lift-off. Researchers from DLR's Materials Physics in Space and AeroSpace Medicine Institutes eagerly waiting for their experiments on thermophysical properties of liquid Zr-Ni droplets levitated electrostatically, on demixing of Cu-Co melts (see report on DEMIX module page 5), on monitoring of dendritic growth in Al-Ge melts by x-ray radiography and on the influence on the absence of gravity on the fluidity in cellular membranes.

Contents

1 Reports

1.1 Methods Development

Sample Detection for Microgravity Electrostatic Levitation

D. Bräuer* and C. Neumann

Institut für Materialphysik im Weltraum, Deutsches Zentrum für Luft- und Raumfahrt (DLR), 51170 Köln, Germany

Electrostatic levitators (ESL) allow for investigation of thermophysical properties of melts at high temperatures. Material properties as viscosity or density can be determined with high precision over a wide temperature range, including a deep undercooling. Due to the lack of potential minima in electrostatic fields (Earnshaw Theorem), the sample position is never autostabilizing. A closed feedback loop is mandatory to sustain stable levitation. In this the determination of position data is time critical for the levitation. Therefore, a fast, robust and precise measurement of the three dimensional sample position has to be implemented.

To identify the sample position, either Position Sensitive Detectors (PSDs) or Imaging Devices can be used. The PSDs used in laboratory environments turned out to be unreliable for sounding rocket or parabolic flight due to thermal drift, increased g-levels and vibrations. This was tested during the 25th DLR parabolic flight campaign. A manual adjustment before each measurement, like in laboratory, is not feasible. To overcome those problems the PSDs have been replaced by CCDs (Charge Coupled Device) cameras. First experiences with low resolution CCD-based sample detection are explained in [1]. Nowadays, the performance of camera-systems and image analysis allows for precise detection at high frame rates. With the current setup the position is obtained with an accuracy of $\pm 13.5\,\mu\mathrm{m}$.

To use the acquired images for position control, a real-time image analysis is necessary to determine the sample position. Using a 200 fps acquisition hardware the algorithm needs to perform several steps to derive the sample position from the cameras within 5 ms. Furthermore, for autonomous operation mode it is mandatory to automatically load the next sample and start a new measurement cycle, if the sample has been lost. The criteria for a sample present is the maximum contrast in the image. For lower temperature range a background illumination is needed to offer sufficient contrast. For higher temperatures the illumination needs to be switched off to see the bright sample on a dark background. In the next step the algorithm calculates the sample position. This needs to be robust with respect to sample size, position and shape. For example it needs to find fast moving samples, which no longer appear as a spherical object with clear border to offer a chance for the controller to react properly.

Fig. 1 shows the single steps of the sample detection algorithm. (a) represents the original image acquired. After determination of the illumination status the image is divided into squares of $15\,\mathrm{px} \times 15\,\mathrm{px}$ and the grey values are summed up for each square (b). In the resulting matrix the lowest sum indicates the darkest area. This is an information about the sample position, with the centre of the associated square as a random pixel within the sample boundary. This is used as a starting point for border detection. The algorithm searches along the four main directions for the highest gradient in grey value within a predefined distance (c). Each found maximum gradient indicates the border of the sample (d). With the position of the four border points it is possible to calculate the centre of the sample (e). To test if the sample is found, the radius of the found object can be calculated and compared to the expected one (f).

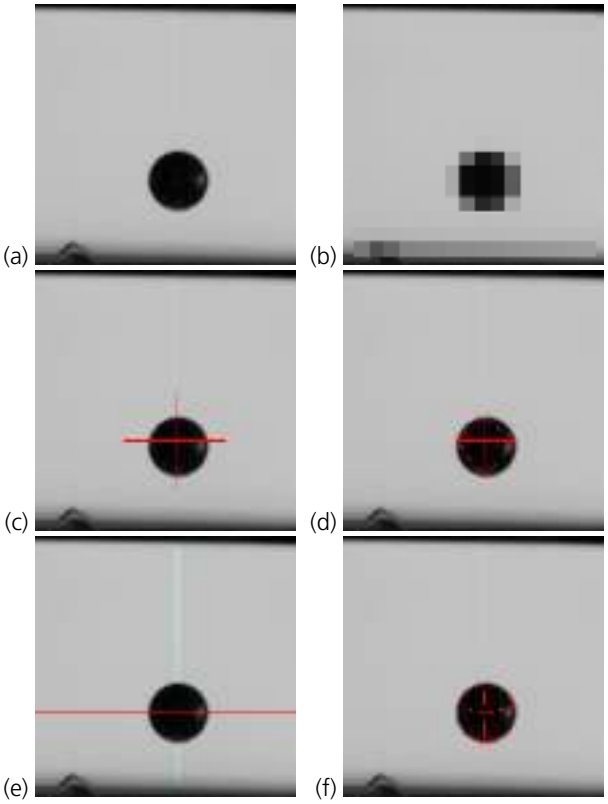

FIG. 1: Different steps performed by the sample detection software to find a sample in front of an illuminated background: (a) acquired image, (b) scaled grey value sums, (c) border detection range, (d) detected edges, (e) calculated centre, (f) calculated radius

For the GOLD-ESL setup the algorithm runs on an Intel Core i7 ITX computer performing the image-detection. It is implemented in NI LabVIEW 2015 using the IMAQdx libraries and is able to perform more than 4000 cycles/s. The detection system was successfully tested in laboratory, at the MAPHEUS-05 sounding rocket and during the 28th DLR parabolic flight.

* Corresponding author: dirk.braeuer@dlr.de

[1] G. Sridharan, S. Chung, D. Elleman, and W.K. Rhim, in: *Proc. SPIE* **1118**, 160–165 (1989).

TEMPUS Parabolic flight campaign

D. Heuskin,* D. Bräuer, Ch. Dreißigacker, M. Engelhardt, G. Lohöfer, K. Prochnow, J. Schmitz, and S. Schneider
Institut für Materialphysik im Weltraum, Deutsches Zentrum für Luft- und Raumfahrt (DLR), 51170 Köln, Germany

With the facility TEMPUS (Containerless Electro-Magnetic Processing Under Microgravity conditions) electrically conductive samples of alloy systems can be processed in microgravity. Without contact to a container, samples are positioned and heated by electromagnetic fields generated by a coil of 18 mm in diameter. First, the sample is melted and while still positioned, the heater field is switched off. The sample cools down and remains liquid (and in most cases undercools below its melting point) until it solidifies. Before it solidifies, stimuli can be applied while diagnostic tools monitor the temperature and capture videos. Those are used to determine thermophysical properties of the examined sample, like viscosity, surface tension, or thermal expansion. For those measurements the oscillating drop method is used, where surface oscillations are triggered by heater pulses. From the dampening of these oscillations the viscosity can be deduced and from their frequency the surface tension is calculated. The rapid advancement of phases solidifying and microstructures forming out of the undercooled melt are captured by a high speed camera.

In September 2016, a parabolic flight of the TEMPUS facility has been performed as part of the 29th DLR campaign. The TEMPUS facility was prepared and operated by DLR-MP. The experiment preparation and operations program was led by MP-EXP. The facility was operated on 4 days with 31 parabolas each. In total experiments from 18 proposals (ESA, DLR-BO and MP) were conducted and 21 samples were processed. One day was dedicated to measurements in high speed camera mode for the observation of solidification. Fig. 1 shows the solidification of $Fe_{50}Co_{50}$. On the 2nd and 3rd day, the camera was used in oscillation measurement mode. The last day was split for high speed Chill Cooling experiments and then configured to oscillation mode.

Besides the scientific aims:

- Qualification of different samples and sample holders (CC) for EML Batch 2 and 3 on ISS
- Measurement of thermophysical properties for industrial casting alloys
- Measurement of solidification rates
- Measurement of the sample electrical conductivities with the sample coupling electronic device

the campaign had technical aims in addition:

- Test of different modulation profiles
- Operability tests for ISS (e.g. levitation behaviour of ferromagnetic samples)

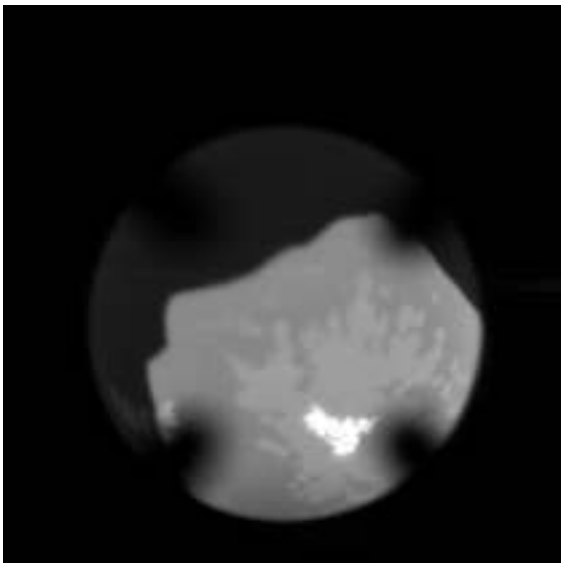

FIG. 1: Double recalescence of $Fe_{50}Co_{50}$ recorded by high speed camera.

The preparation for the parabolic flight included the physical characterization of the samples (materials data compilation, emissivity and coupling data determination). The EML laboratory model is available for flight preparation and is in most functions identical to the core part of EML flight equipment including the digital video system. Parameter sets on the laboratory model on ground can be developed directly in flight format without a further data conversion process. Based on this data, experiment operations were planned with the investigators. A flight schedule for the campaign was iterated and final operation procedures were developed. During the campaign, DLR-MP lead the experiment operations. On-line quick-loop analyses of experiments enabled to apply modifications to the experiment settings during flight. Lessons learned were implemented into the subsequent flight day operations plan in coordination with the investigators and the flight operations team. As a further task, DLR-MP supported the conductivity measurements performed by Georg Lohöfer. Potential ISS EML samples demonstrated their good levitation and positioning abilities and are now qualified for processing in space.

After the flight, the respective facility-, experiment- and video-data were distributed to the investigators. All flight data (raw data, processed data and campaign information) will be long-term archived in the MUSC Hypertest system, which is online and accessible via Web.

* Corresponding author: david.heuskin@dlr.de

Improvements to the TEMPUS parabolic flight facility

D. Bräuer* and D. Heuskin

Institut für Materialphysik im Weltraum, Deutsches Zentrum für Luft- und Raumfahrt (DLR), 51170 Köln, Germany

For over 25 years, the TEMPUS (Tiegelfreies elektromagnetisches Prozessieren unter Schwerelosigkeit) facility has been used to measure thermophysical properties under microgravity [1]. Since the 23rd DLR parabolic flight campaign in September 2013, TEMPUS has been operated by the Institute of Materials Physics in Space. After the last flight of the Airbus A300 in September 2014 it was necessary to change the facility to fulfil the new Novespace safety requirements for parabolic flight experiments on the new Airbus A310.

The operator racks were completely rebuild out of Rexroth Bosch profiles to fit the Novespace standards. This was taken as the start for a overall redesign.

The formerly used LPS-Demonstrator showed some issues during continuous operation on the last campaigns. For the new setup it was possible to use the former TEXUS sounding rocket RF-generator which turned out to be more reliable.

All electrical connections, power supplies, and most of the PCBs were renewed. The power distribution is managed by a single Power Box. It contains the safety features for the AC lines. The former setup used over 15 separate AC/DC converters to power the equipment. This is now done using four high efficient supplies inside the Power Box. The controls for RF, gas atmosphere, coil-cooling, high-speed-camera, and illumination are combined in a single Control Box and can be handled by one operator. The data acquisition was changed to perform more measurements at higher precision. With the new components the overall power consumption could be reduced to less than 60 %.

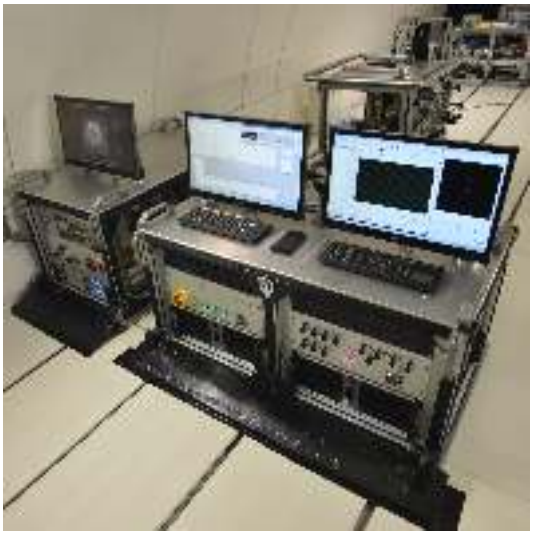

FIG. 1: Front of TEMPUS facility: The rack on the left contains the new LPS power supplies (bottom), the generator cooling system (middle), and components of the gas- and transfer-system. The rack in the middle contains the power box and the control computer. The rightmost rack includes the control box and the video computer.

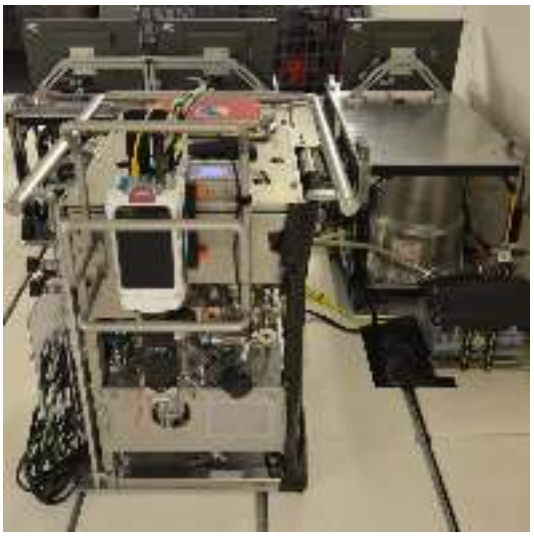

FIG. 2: Back of TEMPUS facility: The experiment unit at the front contains the sample chamber and the Phantom v711. On the right side behind the pre-pump the TEXUS RF-generator can be seen.

The high-speed-camera has been upgraded to a Phantom v711 mounted on the experiment unit. For oscillation measurements, the resolution is increased by 30 % in each direction using up to 1000 fps. For observation of solidification, the captured area is more than twice the previous one. The camera is capable of 79 000 fps using the resolution of previous flights and 40 000 fps by using the new one. This shows significant improvements while observing fast solidifications or double-recalescense. The camera is fully integrated into the control software. The operator can predefine all settings and triggers which are processed by the software. All images are stored to a high speed 512 GB CineMag. This allows for transferring more than 16 GB during two parabolas, which is eight times the amount of the previous system. This means no additional operator and computer is needed to process the videos during flight. Cutting of videos on ground results in less failures.

The new setup was successfully tested at the 29th DLR parabolic flight campaign in September 2016. 21 samples were processed during 124 parabolas. Fig. 1 and Fig. 2 show the facility installed in the Airbus A310.

* Corresponding author: dirk.braeuer@dlr.de

[1] G. Lohöfer, P. Neuhaus, and I. Egry, *High Temp - High Press.* **23** (1991), pp. 333–342.

DEMIX – Sounding rocket module for liquid-liquid demixing of alloys

Ch. Dreißigacker,* S. Asmus, F. Kargl, and M. Kolbe
Institut für Materialphysik im Weltraum, Deutsches Zentrum für Luft- und Raumfahrt (DLR), 51170 Köln, Germany

Solidification of metallic melts has been studied for centuries. In general, the homogeneous melt demixes into a solid phase and the remaining liquid. Less studied is the case when the homogeneous melt demixes into two liquids prior to solidification. When cooled, a homogeneous liquid with a certain composition decomposes at the temperature of the binodal, nucleating droplets of a certain composition in the remaining liquid. If cooling is slow the droplets grow in time continuously changing their composition. The driving force is the minimisation of the interfacial energy between the two liquids. The droplets undergo a similar process like Ostwald ripening of precipitates in the solid. Our purpose is to study demixing of a homogeneous liquid into two liquid phases and the development of these phases in time. After identification of the underlying physical mechanisms, the aim is to model the process.

An experimental observation of liquid-liquid demixing of metallic alloys is not straightforward. In the standard equilibrium demixing scenario droplets cannot easily be frozen in when the material is solidified. This can be overcome by choosing a system that shows a metastable miscibility gap, hence, in the undercooled liquid region. In this case first liquid droplets will form followed by rapid solidification, which freezes the droplets for post-mortem analysis. Co-Cu turned out to be an ideal system since it shows a metastable miscibility gap which can be accessed by undercooling experiments. In ground based experiments, the growth of the liquid droplets is strongly perturbed by convection in the melt and sedimentation. In microgravity demixing experiments this can be overcome. The Co-Cu system has been investigated in the frame of the ESA-MAPs CoolCop and LIPHASE using electromagnetic levitation on the TEXUS 44 sounding rocket and on the International Space Station in MSL-EML. [1] Though giving easy access to the undercooled liquid region and the benefit of controlled fluid-flow only very few samples are processed due to the high cost associated with these experiments.

Here, we present a sounding rocket module which has been developed for the sounding rocket MAPHEUS (Materialphysikalische Experimente unter Schwerelosigkeit) operated by DLR, called DEMIX. DEMIX uses instead of levitation the melt fluxing technique for undercooling of Co-Cu droplets. Hereby, the sample is embedded in glass contained in an Al_2O_3 crucible, which is externally heated in a compact furnace environment. The glass flux serves as a sample purifier and guarantees deep undercooling. Different to EML no stabilizing electromagnetic fields are required avoiding induced fluid flow within the sample.

A first version of DEMIX was operated aboard MAPHEUS-03 as a 14"-payload. An altered nucleation behavior was found compared with previous EML experiments, which requires further samples to be processed. For MAPHEUS-06 the payload was adapted to the new 17" diameter outer structure. A major upgrade was to increase the number of furnaces and samples and thereby the redundancy of the experiments. The module now houses 4 furnace units with 4 samples each in two independent gas-tight environments, which can be controlled separately. It also contains rechargeable battery packs for each furnace and a central data acquisition (daq) device and control unit to control and monitor the experiment. Thereby the module can work autonomously now.

FIG. 1: CAD model of DEMIX with structure in sectional view (top: furnaces in process chambers (transparent), left: umbilical, right: gas tanks, orange: battery packs, green: daq)

A CAD assembly of DEMIX is shown in Fig 1. The top shows the 4 furnace units in the two gas-tight compartments. In the experiments these are first evacuated and then backfilled with Argon. The Argon atmosphere is kept until target temperature is reached at which point Helium is added from the on-board gas-cylinders to increase cooling speed. Further umbilicals can connect to the most important interfaces of the module. The evacuation of the process chamber, filling Ar and He is possible without opening of the module. Further electrical connections for external heating of the furnaces, charging of the battery packs and a USB connection for programming and system control are implemented. Originally intended to supply the system externally before rocket launch the umbilical allows the operation to be completely independent of the rockets infrastructure, eg in the laboratory.

* Corresponding author: christoph.dreissigacker@dlr.de

[1] M. Kolbe, *Demixing of Cu-Co alloys showing a metastable miscibility gap*, in: *Solidification of containerless undercooled melts*, edited by D.M. Herlach, D.M. Matsen, (Wiley-VCH, Weinheim, 2012).

Development of a Hybrid Aerodynamic-Electrostatic Levitator

P. Fopp,[1,*] D. Bräuer,[1] J. Drescher,[1] C.C. Yuan,[2] and F. Kargl[1]

[1] *Institut für Materialphysik im Weltraum, Deutsches Zentrum für Luft- und Raumfahrt (DLR), 51170 Köln, Germany*
[2] *Southeast University, School of Material Science and Engineering, 21189, Nanjing, China*

Al-based alloy systems are of high interest both from a scientific viewpoint as well as for applications in e.g. the aerospace industry. Because systems, such as Al-Ti, Al-Fe, and Al-Zr exhibit phases with high melting points and are highly reactive, measurements of their thermophysical properties over a broad temperature and composition range require containerless processing techniques. Whilst measurements of density and surface tension can be performed on ground, viscosity measurements require microgravity conditions if electromagnetic levitation is used. However, such measurements are expensive and systematic studies are largely precluded. Using electrostatic levitation (ESL) on the ground it was shown that viscosity measurements are in principle possible [1]. For Al-based systems they fail due to sudden surface charge changes related to solid-state phase transformations upon heating. In addition, low vapour pressure systems rapidly evaporate under high vacuum conditions of the standard ESL leading both to a charge loss and non-stoichiometric changes of sample composition. The newly developed Hybrid Aerodynamic-Electrostatic Levitator (HÆL), as shown in Fig. 1, combines aerodynamic and electrostatic levitation techniques. The Japan Aerospace Exploration Agency (JAXA) has already developed a pressurized hybrid electrostatic-aerodynamic levitator for the characterization of oxides [2, 3]. The focus of HÆL is to levitate metallic samples in a high purity Argon 6.0 atmosphere. Generally, in HÆL a sample first is levitated aerodynamically and molten via infrared laser heating (975 nm) before it is forwarded to the electrostatic device to overcome the described charging problem. By means of a high-speed camera and pyrometric measurements we plan to perform precise measurements of density, surface tension and viscosity from the highly undercooled to the highly superheated liquid region.

High demands are placed on the instrument's sealings, since the levitator will operate under 20 bar overpressure after evacuation to 10^{-6} mbar. For the localization of the operating point the Paschen law for Argon turned out to be only a rough approximation (see Fig. 2). It predicts only 1 bar pressure at 20 kV for the choosen electrode configuration instead of at least 15 bar measured experimentally. A first version of the electrode system was microgravity-ESL inspired. After a redesign to an upturned ground-based ESL electrode system HAEL was operational for 20 kV high voltage at 20 bar Argon. During functional tests a 2 mm Al sample, which was aerodynamically pre-levitated and molten, accumulated enough charge to undergo electrostatic levitation.

At present the control system for stable ESL levitation is being implemented and remaining electrical breakthroughs are to be eliminated. It is planned to verify the instrument via thermophysical property measurements of the well-characterized Zr-Ni systems.

FIG. 1: The assembled Hybrid ADL-ESL Levitator in the lab

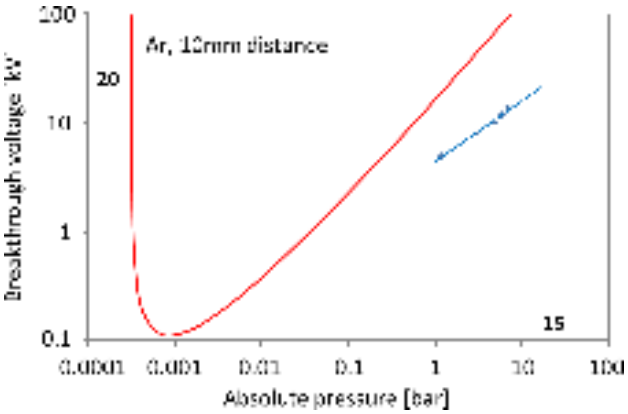

FIG. 2: Measurements (blue) differ from the prediction by the Paschen law (red).

Special thanks go to Fan Yang and Christian Neumann, Stefan Klein, Karsten Binder, Sina Asmus, Marius Meyer, Christoph Dreißigacker, Andreas Hollmann and Michael Balter as well as the institute's workshop team.

* Corresponding author: patrick.fopp@dlr.de

[1] P. Heintzmann, F. Yang, S. Schneider, G. Lohöfer, and A. Meyer, *Appl. Phys. Lett.* **108**, 241908 (2016).
[2] T. Ishikawa, J. Yu, and P. F. Paradis, *Rev. Sci. Instr.* **77**, 053901 (2006).
[3] P. F. Paradis, T. Ishikawa, J. Yu, and S. Yoda, *Rev. Sci. Instr.* **72**, 281 (2001).

Viscosity measurements of metallic melts using the oscillating drop technique

P. Heintzmann, F. Yang,* S. Schneider, G. Lohöfer, and A. Meyer
Institut für Materialphysik im Weltraum, Deutsches Zentrum für Luft- und Raumfahrt (DLR), 51170 Köln, Germany

Despite the importance of liquid viscosity η, its determination, especially for metallic melts, is challenging. Conventionally, this is done via shearing liquids in crucibles. For metallic melts, these measurements become increasingly unreliable due to the chemical reactivity of the melt at elevated temperatures, since the liquid−container reactions may alter the results.

One possibility to overcome these obstacles and handle such materials is the use of containerless processing techniques such as levitation. A technique to measure the viscosity on a levitated liquid droplet is the so called oscillating drop method, based on the undisturbed decay of the oscillation of the droplet. However, the derivation of the viscosity using such technique involves idealised assumptions, which makes it sensitive to experimental conditions.

The aim of the present studied is, hence, to investigate whether and under which experimental conditions the oscillating drop technique provides reliable viscosity data, especially in combination with the electrostatic levitation (ESL) [1]. We studied a binary glass forming Zr-Ni system, where we systematically varied the sample size in the ESL measurements, combined with experiments under reduced gravity conditions, to study the influence of the different experimental conditions.

Fig. 1 upper panel shows the temperature dependent melt viscosity of $Zr_{64}Ni_{36}$ measured under different experimental conditions. The samples with a mass m_s up to $\sim$ 300 mg were used in ESL. Within the measurement uncertainties, the viscosity measured in ESL using small samples ($m_s \leq 100$ mg) shows no sample mass dependence. The obtained values also agree with that measured under reduced gravity conditions using the TEMPUS EML facility, with a sample mass of 1240 mg. In contrast, viscosity data obtained in ESL using higher m_s deviate from the above described results. For $m_s = 160$ mg, the viscosity above 1280 K is lower compared to that obtained from smaller samples. Disagreements are found between the data obtained for $m_s = 300$ mg and that from the smaller samples. However, here the values are higher than that of the smaller samples at 1200 K. In both cases, the deviation increases with increasing temperature, whereas for $\eta > 80$ mPas all viscosity data show good agreement.

For measurements in ESL, where deviations occur, additional excitations can be observed during the decay of the oscillation, best visible in the Fourier transformed spectrum shown in the lower panel of Fig. 1. For the $m_s = 160$ mg sample, a superposition of the main oscillation frequency (at ∼90 Hz) with a further oscillation of lower frequency occurs. Such periodic perturbation during the decay of the oscillation, possibly due to the vibration of the levitation facility and/or the sample, leads to a larger decay constant, and hence to an underestimation of the viscosity. For even higher sample masses, more pronounced beats can be observed in the oscillation amplitudes, leading to a splitting of the oscillation frequency, caused by e.g.: sample rotation. The damping at the presence of these additional oscillation frequencies cannot be attributed to a single oscillation mode, which results in faster decays and an overestimation of the viscosity.

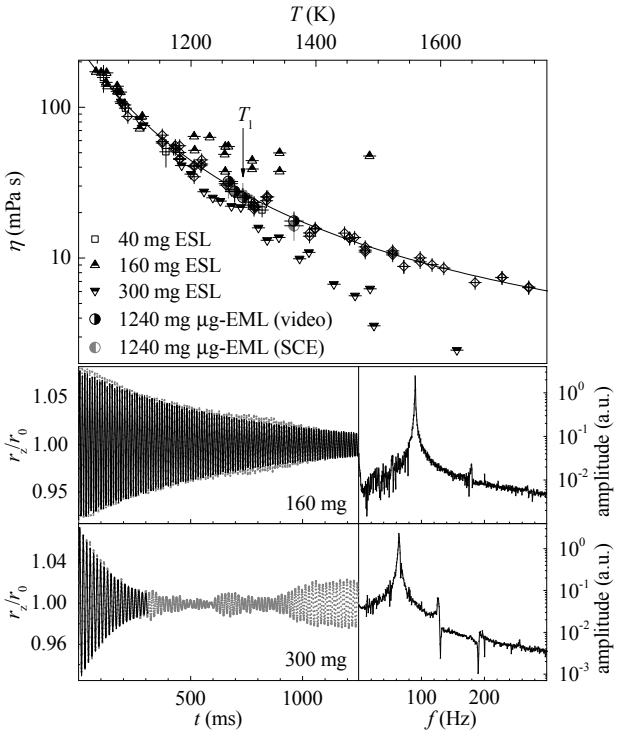

FIG. 1: Upper panel: Temperature dependent viscosity of $Zr_{64}Ni_{36}$ for different sample masses. Open squares and half filled triangles show ESL measurements, half-filled circles are data obtained using the TEMPUS facility. Lower panel: Decay of sample oscillations (left column) using ESL at 1485 K with Fourier transformation (right column) of $Zr_{64}Ni_{36}$ samples.

Therefore, We conclude that reliable viscosity data can be obtained by oscillating drop technique as long as compared to external perturbations, the internal viscous damping of a single oscillation mode dominates. This can be verified by the absence of sample mass dependence of the results. For ground based ESL, this is the case for sample masses below 100 mg and a viscosity range of $10 - 250$ mPas. Since the viscosity of most of metallic glass forming melts lies in this range, ESL is an excellent tool for studying these liquids.

* Corresponding author: `fan.yang@dlr.de`

[1] P. Heintzmann, F. Yang, S. Schneider, G. Lohöfer, and A. Meyer, Appl. Phys. Lett. **108**, 241908 (2016).

Electrostatic Levitation of Metallic Samples in Parabolic Flight

C. Neumann,* D. Bräuer, S. Zimmermann, and A. Meyer
Institut für Materialphysik im Weltraum, Deutsches Zentrum für Luft- und Raumfahrt (DLR), 51170 Köln, Germany

Containerless processing of liquified metal alloys can be performed by means of electrostatic levitation. While a sample levitates in the electrostatic field it is accessible for contactless measurement of thermophysical properties, as viscosity and surface tension are [1]. The viscosity of a sample depends on material and temperature. For some measurements on lower viscose samples, gravity shows disturbing influence. Carrying out such an experiment in microgravity is believed to fix this issue. Therefore a development project was initiated to overcome the technical restrictions to use an electrostatic levitator in microgravity. This project GOLD-ESL aims for parabolic flight and sounding rocket purpose.

First microgravity experiments have been carried out during the 24th DLR parabolic flight campaign in February 2014. Since then the experimental set-up has been integrated into the payload for MAPHEUS sounding rocket [2, 3]. Hardware testing and software calibration for microgravity started at the ZARM drop tower in Bremen 2014, and were continued when the experiment got airborne aboard MAPHEUS-05 in June 2015.

Earlier this year, the 28th DLR parabolic flight campaign was joined. This time the complete rocket payload had to be installed in an upright position in the aircraft. Though designed for more heavily mechanical loads than occur on parabolic flight, the task to fix a 120 kg cylinder is challenging due to the high centre of gravity.

Fig. 1 shows the final set-up, consisting of two separate parabolic flight racks. The one on the left contains the rocket payload. This rack is reinforced by four wire cables. In advance of the campaign the payload was manipulated in two major terms. First, the internal batteries to supply energy have been removed due to in flight rules and guidelines. Secondly, electrics had to be split into several independent circuits, each protected by fast acting fuses, according to the same set of rules. The rack to the right contains all auxiliary equipment needed in flight, such as power supplies, vacuum pumps and the control PC. Via this computer three operators supervise and control the levitation experiments.

This campaign was designated to technological tests and aimed to release preheated but still solid samples into microgravity. And then gain control over sample position by means of electrostatic positioning. Once a sample is positioned stable in the centre, the further test procedure is to continue on heating, up into the liquid phase. Two different sample materials have been used, $Zr_{64}Ni_{36}$ and $La_{80}Cu_{20}$. Both could be stabilized after being released to prove the microgravity ability of the set-up. Laser heating of the sample causes

FIG. 1: The GOLD-ESL Experiment is shown in flight configuration onboard the Zero-G aircraft. On the left the rocket payload is fixed into a rack. On the right the experimenters rack containing auxiliary equipment can been seen.

discharging effect due to evaporation of charged surface particles. Above a certain temperature the sample regains positive charge by thermionic emission. During the parabolic flight campaign, attempts to reach the self-charging temperature regime failed. Different heating rates have been tested. The remaining charge of the samples was insufficient to obtain stable levitation concerning the g-jitter during the parabolas. A much slower heating rate like used in laboratory environments could not be applied because of the short available microgravity time of 22 s. As a result of the parabolic flight, improvements on the recharging of the samples were made. This set-up is part of the payload for the upcoming MAPHEUS-06 campaign.

We would like to thank NOVESPACE and especially Brian Verthier for the professional support in preparation as well as in execution of the parabolic flight campaign, and the DLR Space Administration for this valuable flight opportunity.

* Corresponding author: christian.neumann@dlr.de

[1] W. Rhim, K. Ohsaka, P. Paradis, and R. Spjut, in: *Review of Scientific Instruments 70,* (1999)
[2] A. Stamminger, J. Ettl, G. Blochberger, J. Drescher, A. Griesche, F. Hassenpflug, S. Hoepfner, M. Hörschgen, A. Meyer, C. Neumann, L. Ratke, E. Plescher and R. Willnecker, in: *IAC Proceedings 2009* (60th International Astronautical Congress, Daejeon, 2009).
[3] M. Siegel, F. Kargl, F. Scheuerpflug, J. Drescher, C. Neumann, M. Balter, M. Kolbe, M. Sperl, P. Yu and A. Meyer, in: *Proceedings of the 21st ESA Symposium on European Rocket and Balloon Programmes and Related Research* (2013), ESA Special Publication SP-721, pp. 179–183.

EML experiments on board the ISS

S. Schneider,* J. Schmitz, M. Engelhardt, P. Heintzmann, and M. Lammel
Institut für Materialphysik im Weltraum, Deutsches Zentrum für Luft- und Raumfahrt (DLR), 51170 Köln, Germany

EML is an electromagnetic levitation facility, installed in the European drawer rack (EDR) in the Columbus module on the ISS. With this non-contact method metallic samples are melted and processed under reduced gravity conditions. Experiments on the first Batch (first sample chamber, containing 18 samples) started in 2015 and were finished recently in 2016. Within this Batch 16 different alloys were studied; in 343 melt cycles a variety of scientific measurements were performed:

- Surface tension and viscosity using the oscillating drop method (Fig. 1)
- Specific heat using modulation calorimetry (Fig. 2)
- Growth velocity of the solidification with the high speed video camera
- Investigation of the effect of electromagnetic stirring on solidification and surface tension & viscosity
- Investigation of the solidification and time to crystallization
- Demixing of liquid CuCo samples
- Investigation of the behaviour of oxide particles in solidifying samples

However, from the evaluation of the Batch 1 experiments, it turned out that for some of these samples further investigation is needed. Hence, besides the start of the next experiment series of EML - Batch 2 - additional cycles for Batch 1 will be planned and resumed in 2017.

FIG. 1: Ni-base superalloy excited to surface oscillations by application of a heater pulse

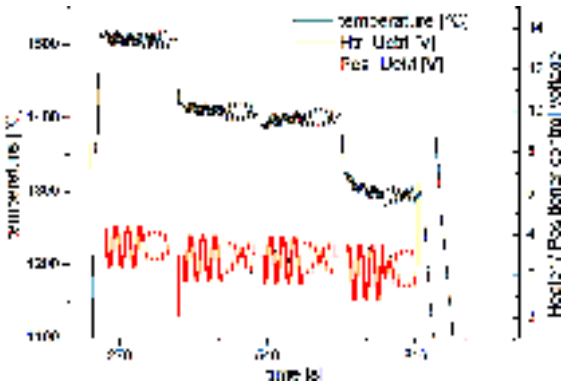

FIG. 2: Specific heat measurement by modulation calorimetry: The power input is modulated and the temperature response of the sample is measured

The experiments are remotely controlled from the ISS-payload control room at MUSC. There, the console operator and the investigating scientist (Principal investigator, PI) of a sample are always advised by user support scientists from the Institute of Materials Physics in Space, who previously developed the complex, semi-automatical experiments together with the PI. The experiments comprise of Experiment Parameter Sets, which stepwise define all possible facility settings to enable an automated experiment run, but also allow for reprogramming and amendment of a planned experiment, when during experiment performance it turns out that different settings are more favourable. So, the PI is enabled to react on recent experiment results in near real time. For instance overheating and hold temperatures can be adapted to the observed sample behaviour, pulse application can be adjusted to undercooling, modulation frequencies optimized, recalescence detection parameters tweaked etc.

In order to ensure a flawless experiment conduction, DLR runs an extensive ground support programme for the experiment preparation. In this programme the EML-samples are characterized, the experiments are planned and defined in Science Protocols, and the temperature-time-profiles are simulated before the Experiment Parameter Sets to control the facility during the experiment performance can finally be developed. Before uploading them to the ISS, their reliability is validated using the ground based EML lab-facility, the Operational Model. These last steps are currently being performed for the upcoming Batch 2.

* Corresponding author: stephan.schneider@dlr.de

Overview of Electromagnetic Levitation experiments on ISS covered by DLR

J. Schmitz,* J. Brillo, M. Kolbe, T. Volkmann, and D. Holland-Moritz
Institut für Materialphysik im Weltraum, Deutsches Zentrum für Luft- und Raumfahrt (DLR), 51170 Köln, Germany

After installation of the EML facility into the European laboratory Columbus on ISS, levitation experiments on a first batch of samples (Batch 1) have been performed. This batch comprises of 18 metals or alloys which are melted and solidified contactlessly and studied with different scientific questions in μg conditions. In cooperation with international project partners from EU, USA and Japan, experiments were scientifically prepared, jointly performed and are now being evaluated.

In the performance of Batch 1, the Institute of Materials Physics in Space takes an important role, since it is scientifically involved in all samples. For 10 samples of this batch, the Institute's scientists took the leadership as PI (Principal Investigator) or coordinator of the respective ESA-MAP projects which are COOLCOP, MAGNEPHAS, METCOMP, and NEQUISOL. These projects focus on following objectives:

- COOLCOP: Undercooling and demixing of copper-based alloys.
  Batch 1 alloys: $2\times Cu_{75}Co_{25}$, $Cu_{89}Co_{11}$ (Fig. 1)
- MAGNEPHAS: Study and modeling of nucleation and phase selection phenomena in undercooled melts: Application to hard magnetic alloys of industrial relevance.
  Batch 1 alloys: $Nd_{18}Fe_{73}B_9$, $Fe_{45}Co_{55}$, $Fe_{50}Co_{50}$
- METCOMP: Metastable solidification of composites: Novel peritectic structures and in-situ composites.
  Batch 1 alloys: $Ni_{98}Ta_2$ + Ta_2O_5, $Ni_{96}Ta_4$ + Ta_2O_5 (Fig. 2)

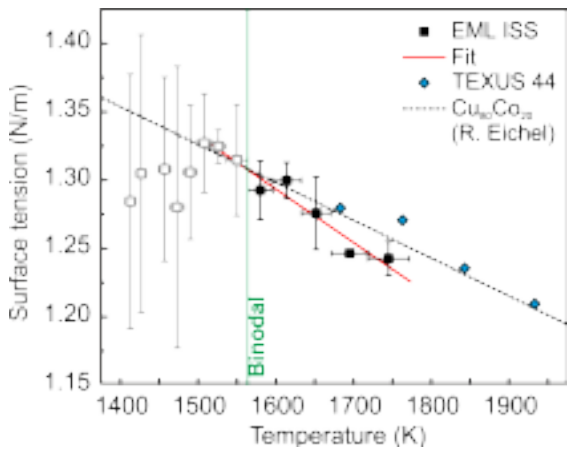

FIG. 1: Evaluation of the surface tension from one thermal cycle on $Cu_{75}Co_{25}$. Data in the single component liquid are in agreement with measurements from TEXUS 44 [1]. Below the Binodal, the uncertainties rise. But as a first hint, surface tension data seem to decrease upon cooling the sample further. Measurements on the other cycles are still under evaluation.

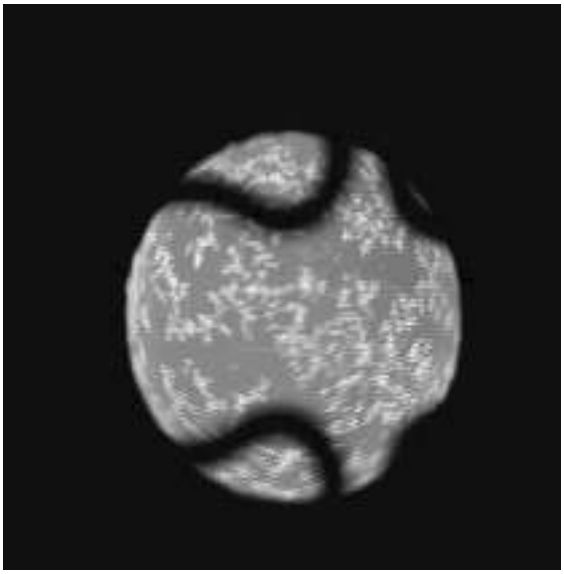

FIG. 2: Particle pushing / engulfment experiment in $Ni_{98}Ta_2$, containing Ta_2O_5-Particles. These are visible as bright spots on the sample's surface. From the microstructure of the solidified sample information on the interaction of particles with the liquid during the solidification process can be gained. Aim is to learn how to reinforce alloys by better dispersion of particles. The microscopic post-mortem examinations will be conducted after the sample will be downloaded from ISS in 2017.

- NEQUISOL: Non-equilibrium solidification, modelling for microstructure engineering of industrial alloys.
  Batch 1 alloys: $2\times Al_{40}Ni_{60}$

Except for the ferromagnetic FeCo alloys, processing worked well. Evaluations are ongoing, first interesting results are being investigated in detail and compared to experiments on further μg platforms and lab based studies.

By combination of experiments in microgravity conditions with their post-mortem analyses and lab based experiments as well as with simulation and theory, a thorough understanding of various fields can be promoted: Nucleation kinetics, the influence of mass flow on growth kinetics, the relation between diffusion dynamics and growth as well as the one between structure of a melt and its atomic dynamics are topics, which can benefit from this combined approach.

In the long term, these results will provide essential building blocks for materials design from the melt.

* Corresponding author: julianna.schmitz@dlr.de
[1] I. Egry et al., J. Mater. Sci. **45**, 209 (2010).

1.2 Liquid and Melt Properties

Density of liquid Ni-Ti and a new optical method for its determination using two cameras in electromagnetic levitation

J. Brillo,[1,*] T. Schumacher,[1] and K. Kajikawa[2]

[1] *Institut für Materialphysik im Weltraum, Deutsches Zentrum für Luft- und Raumfahrt (DLR), 51170 Köln, Germany*
[2] *The Japan Steel Works (JSW) Ltd., Muroran Plant, Muroran-shi, 051-8505 Hokkaido, Japan*

During the past 15 years densities of a large number of liquid monoatomic systems, binary and ternary alloys have successfully been measured in a containerless way, using the optical dilatometry method combined with electromagnetic levitation [1, 2]. However, this method relies on the assumption that, on average, the liquid droplet is symmetric with respect its vertical axis. Then, the sample volume V can be obtained from the following integral, if $< R(\phi) >$ is the edge curve of the sample profile seen by a camera from the side and the brackets denote averaging for each polar angle ϕ over a sufficiently long time, i.e over a number of frames of more than typically 1000:

$$V = \frac{2}{3}\pi \int_0^{\pi} < R(\phi) >^3 \sin(\phi) d\phi \qquad (1)$$

The method is prone to errors originating from a violation of this assumption, due to strong sample rotations, oscillations, or static deformations.
One way of dealing with this challenge is to combine the electromagnetic levitator with a strong magnetic DC field suppressing the fluid flow and, hence, the strong rotations. However, static deformations still remain and might cause systematic errors in the density measurement.
The present work introduces an alternative and comparatively simple concept which effectively solves the problem. We replaced the assumed circular cross section, Q_{circle}, with the real one, Q_{real} by amending Eq. (1) by a factor q. This factor is obtained as

$$q = \frac{< Q_{\text{real}} >}{< Q_{\text{circle}} >}. \qquad (2)$$

In practice, q is determined by using a second camera directed at the sample from the top. It records 1000 frames and a software determines the edge curve of each image from which Q_{real} and Q_{circle} are obtained.
This procedure has been applied for several Ni-Ti samples. Figure 1 shows densities ρ of a $Ni_{50}Ti_{50}$ sample versus temperature T determined once in the conventional way, i.e. by using Eq. (1), and once using the new method with the two cameras. The density calculated from Eq. (1) assuming rotational symmetry are by far too low and exhibit multiple artifacts, so that they are obviously wrong. Applying the second camera and calculating q from Eq. (2) eliminates all the artifacts and the density comes out reasonably realistic. A detailed analysis shows that, despite heavy deviations from the rotational symmetry, the density is obtained this way with an accuracy of better than ± 1.0 %.
Figure 2 shows isothermal densities of Ni-Ti versus the Ti mole fraction at 1400 °C. The data significantly overestimates the ideal solution model. A large negative excess volume has to be taken into account. This is demonstrated by the solid line. Excellent agreement with the data is evident.

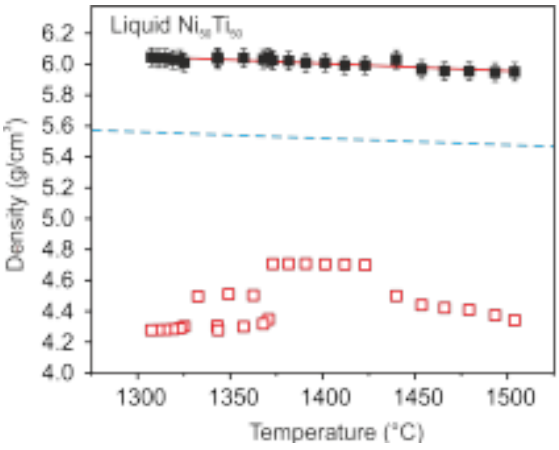

FIG. 1: Density of a levitated $Ni_{50}Ti_{50}$ droplet with strong rotations and a static deformation measured in the conventional way (hollow squares) and with a second camera (solid squares). The dashed line corresponds to an estimation of the density from the ideal solution model.

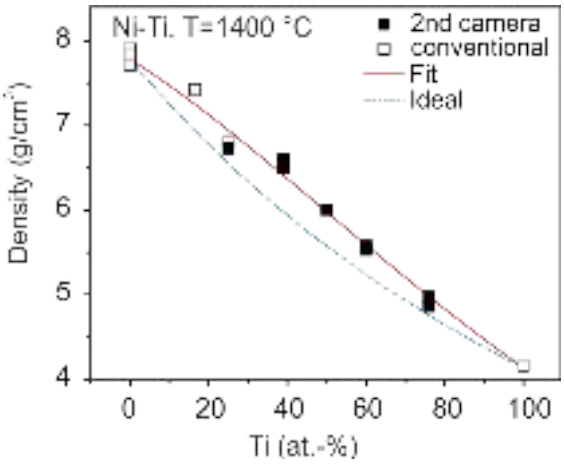

FIG. 2: Isothermal density of liquid Ni-Ti versus the Ti mole fraction at 1400 °C. Data is measured in the conventional way (hollow symbols) and by using the second camera (solid symbols). In addition, calculations of the ideal (dashed line) and regular solution models with a negative excess volume (solid line) are shown.

Funding by JSW is gratefully acknowledged.

* Corresponding author: Juergen.Brillo@dlr.de

[1] J. Brillo, I. Egry, Japanese Journal of Applied Physics **11RD02** 50 (2011).
[2] J. Brillo, *Thermophysical properties of multicomponent liquid alloys* (de Gruyter, Berlin, 2016).

Liquidus surface of the ternary alloy system NiMnGa

B. da Cunha* and J. Brillo

Institut für Materialphysik im Weltraum, Deutsches Zentrum für Luft- und Raumfahrt (DLR), 51170 Köln, Germany

Exhibiting a pronounced magnetic field induced strain the magnetic shape memory alloy (MSMA) Ni_2MnGa is of particular importance for magnetic field controlled actuation and related applications. Predicted as becoming one of the scarcest elements for future technological applications, attempts are made to reduce the Ga content of MSMA preserving their performance parameters. For this purpose, the properties of the ternary alloy system NiMnGa need to be known. As a prerequisite for further thermophysical investigation, a fundamental data basis of the phase transition temperatures and enthalpies has been established for the compositions shown in Fig.1 chosen to be located on lines of constant concentration ratios, as it was done before for the special case of Ni_2MnGa [1].

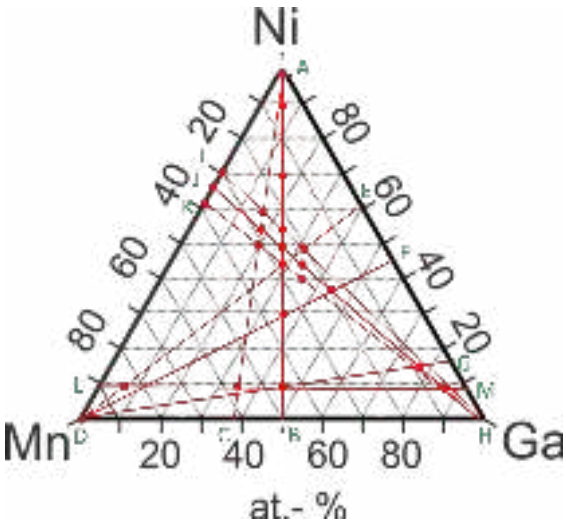

FIG. 1: Ternary compositions of which a DSC analysis has been carried out (red dots), lying on lines of constant concentration ratios (red lines) designated by pairs of letters (green)

The solidus and liquidus temperatures T_S and T_L,respectively, as well as temperatures of phase transitions in the solid state are derived from the measured DSC curves. The solidus temperatures being independent of heating rate β are derived by intersection of the inflexion tangent of each melting peak with the DSC base line while the heating rate dependent liquidus temperatures were determined by extrapolation of the melting peak end temperatures as a function of heating rate β. The liquidus surface of the ternary NiMnGa system interpolated from the experimental data and literature data of the binary boundary systems NiMn, MnGa and NiGa is shown in Fig.2.

In addition, the specific heat at constant pressure $c_p(T)$ as a function of temperature of the compositions lying on A-B as well as H-J have been derived both in the solid and in the liquid phase by comparison of the measured sample- and sapphire reference DSC curves.

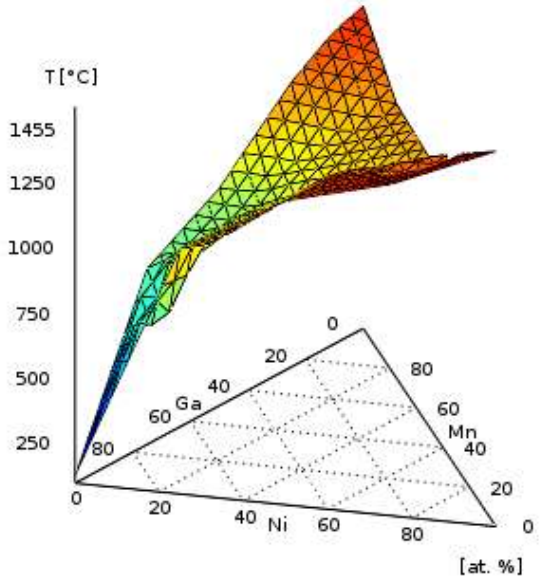

FIG. 2: Experimentally derived liquidus surface of NiMnGa determined by interpolation of measured data and literature data of the binary boundary systems NiMn, MnGa and NiGa.

For the case of the H-J line this is shown in Fig. 3. Further evaluation and interpretation of the data remains to be done.

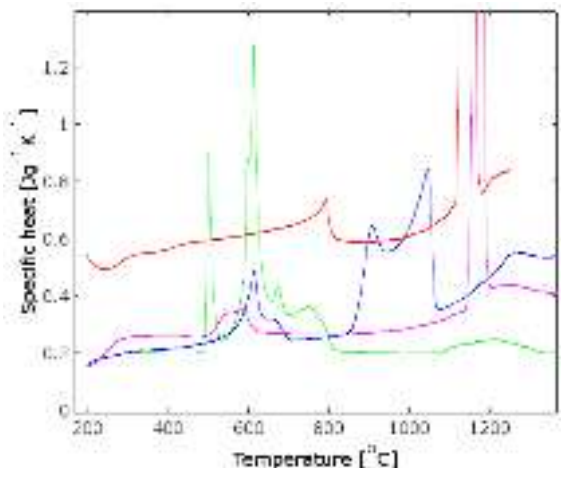

FIG. 3: Specific heat $c_p(T)$ for compositions on line H-J. For clarity, only every second measurement is shown. $Ni_{16.7}Mn_{8.3}Ga_{75}$ (green), $Ni_{37.5}Mn_{18.75}Ga_{43.75}$ (blue) $Ni_{50}Mn_{25}Ga_{25}$ (red), Ni_2Mn (magenta)

* Corresponding author: bernard.baptistadacunha@dlr.de

[1] J. Brillo , H. Behnken , A. Drevermann , Y. Plevachuk, E. Pagounis , V. Sklyarchuk and K. Sturz, Int. Journ. of Heat and Mass Transfer **54**, 4167-4174 (2011)

Investigation of the chemical compatibility between liquid alloys and solid substrates

T. Gläsel,[1,*] J. Brillo,[1] F. Kargl,[1] W. Kraft,[2] and M. Klein Altstedde[2]

[1] *Institut für Materialphysik im Weltraum, Deutsches Zentrum für Luft- und Raumfahrt (DLR), 51170 Köln, Germany*
[2] *Institut für Fahrzeugkonzepte, Deutsches Zentrum für Luft- und Raumfahrt (DLR), 70569 Stuttgart, Germany*

One of the greatest challenges in order to accomplish the energy revolution is the identification of sufficient storage technologies. Phase change materials (PCM) play an increasingly important role due to their high thermal capacities and short conversion times. Solutions involving the solid/liquid phase change of metallic alloys are attractive because, in comparison to phase change materials based on salts, they offer a better heat input and delivery.

Since liquid metals are known for their high chemical reactivity, it is crucial that chemical reactions at the interface are almost avoided in order to gain long-time stability. Additionally, there has to be ideal thermal contact in order to have excellent heat transfer. Hence, the wetting behavior must guarantee a good contact between the container and the PCM - but without chemical reactions. These requirements are to some degree contradictory. Moreover, it is required that potential substrate candidates have melting temperatures above 600 °C and that they are neither toxic nor radioactive.

In order to meet these requirements, a better understanding of the interface is mandatory. The key influences on reactivity, wetting and thermal transport must be identified. Due to their advantageous thermochemical and thermophysical properties, aluminum and magnesium based alloys are identified as interesting candidates for phase change materials. In order to narrow down the number of potential container materials, three different approaches are used.

From a literature research, SiO_2, TiO_2, MgO, Si_3N_4, BN as well as carbides (SiC, TiC, B_4C) are identified as potential substrates. But not all possible systems are covered this way.

In a work by Kostov and Friedrich [1], it is investigated whether different oxide ceramic casting crucibles would react with Ti-Al melts. A simplified method to estimate the reaction enthalpy ΔG_r of an assumed interface reaction is proposed. According to this work there should be no reaction between liquid Ti-Al and solid Al_2O_3 or Y_2O_3. This result could not be validated by our own experimental findings [2].

The investigation of phase equilibria obtained from phase diagram calculations might provide an alternative and might be a more promising approach. In this context, elements that did not show solubility in the area of the composition of the potential phase change material were considered as suitable substrate materials as shown for iron in Fig. 1.

The results obtained by phase diagram calculation and literature research are shown in Fig. 2. The materials in the overlapping area will be considered primarily for further experimental investigations.

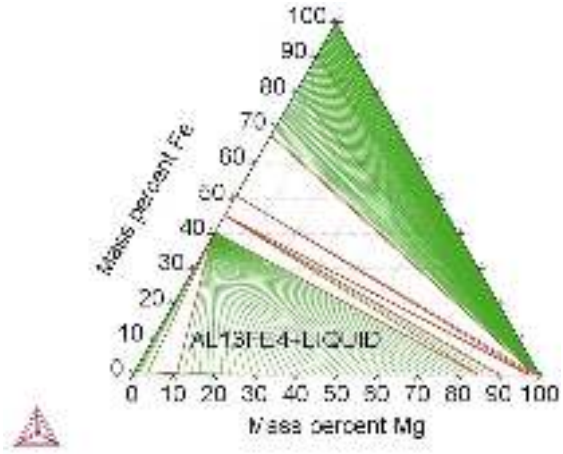

FIG. 1: Isothermal section of the ternary system Al-Mg-Fe at 600 °C

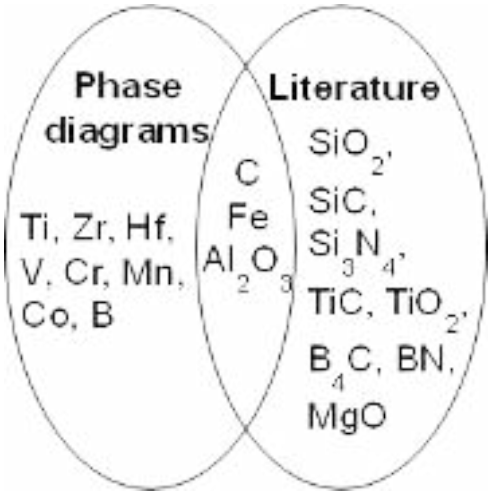

FIG. 2: Potential substrate material candidates obtained by phase diagram calculation and literature research.

The next steps will focus on the experimental characterization of the interfaces. The reactive wetting and influencing factors on it will be analyzed by wetting measurements. Moreover, it will be important to investigate the interfacial heat transfer and the influencing factors on this property in the context of phase change materials for energy storage.

Acknowledgements are given to the DLR Technology Marketing for funding and to the colleagues M. Klein Altstedde and W. Kraft from the DLR in Stuttgart.

* Corresponding author: tina.glaesel@dlr.de

[1] A. Kostov and B. Friedrich, J. Min. Met. **41 B**, 113 - 125 (2005).
[2] private communication F. Kargl and results to be published by Binder et al. in Rev. Sci. Instrum.

Short-range order of glass-forming Ni-Hf melts

D. Holland-Moritz,[1,*] B. Nowak,[1] F. Yang,[1] T. Kordel,[1] D. Brüggemann,[1] and T. Hansen[2]

[1] *Institut für Materialphysik im Weltraum, Deutsches Zentrum für Luft- und Raumfahrt (DLR), 51170 Köln, Germany*
[2] *Institut Laue-Langevin (ILL), 38042 Grenoble, France*

Metallic glasses have attracted considerable attention in both scientific and technological fields. While in preceding investigations the short-range order of melts of binary Zr- or Nb-based glass-forming alloy systems such as Zr-Cu [1], Zr-Ni [2], Zr-Pd [3] or Ni-Nb [4] has been studied, here we present neutron scattering experiments on the short-range order of glass-forming Ni-Hf alloy melts, for which the early transition metal component (Zr or Nb) is replaced by Hf.

In order to avoid possible reactions of the melts with crucible materials and in order to reduce background scattering at materials in the vicinity of the sample, the liquids are containerlessly processed under high vacuum (pressure $<10^{-6}$ mbar) by employing a compact electrostatic levitator specially developed for performing scattering experiments [5]. The neutron scattering experiments were performed by use of the diffractometer D20 at the Institut Laue-Langevin (ILL) using a wavelength of the incident neutrons of λ = 0.94 Å. Total structure factors, S(Q), of three $Ni_{65}Hf_{35}$ melts prepared with natural Ni, ^{58}Ni, and ^{60}Ni were measured. Partial static structure factors are calculated from the three total structure factors within the Faber-Ziman and the Bhatia-Thornton formalism. From the partial structure factors partial pair correlation functions are calculated by Fourier transformation. These provide information on the neighbor distances (radii at which the maxima of the partial pair correlation functions are observed) and on the partial coordination numbers. As an example, fig. 1 shows the partial Faber-Ziman pair correlation functions g_{NiNi}, g_{HfNi} and g_{HfHf} determined for liquid $Ni_{65}Hf_{35}$ at a temperature of T = 1510 K (red curves) together with corresponding results obtained for molten $Ni_{64}Zr_{36}$ at $T = 1385K$ (black curves). Despite the fact that Hf is member of the same group in the periodic table of the elements as Zr and is also characterized by a similar Goldschmidt radius, significant differences in the structure of the Hf and the Zr containing liquid are visible. Most striking are the considerably smaller first and second neighbor distances of R^1_{HfHf} = 3.15 Å and $R^2_{HfHf} = 4.66$Å found for the Hf-Hf pairs in liquid $Ni_{65}Hf_{35}$ as compared to the distances of the Zr-Zr pairs in $Ni_{64}Zr_{36}$ ($R^1_{ZrZr} = 3.31$Å and $R^2_{ZrZr} = 5.02$ Å). Moreover, the first maximum of g_{ZrNi} is considerably sharper than that of g_{HfNi}, indicating a broader distribution of first Hf-Ni distances in $Ni_{65}Hf_{35}$ as compared to that of the Zr-Ni distances in $Ni_{64}Zr_{36}$. On the other hand, the Ni-Ni correlations are similar in both liquids. The nearest neighbor coordination number $Z_{NN} \approx 13.3$ determined for liquid $Ni_{65}Hf_{35}$ is slightly smaller than that determined for $Ni_{64}Zr_{36}$ ($Z_{NN} \approx 13.8$). From the partial coordination numbers Z_{HfHf} = 5.3, Z_{NiHf} = 10.4 and $Z_{NiNi} = 6.2$ the average coordination numbers of the different types of atoms, Ni and Hf, can be calculated. While the smaller Ni atoms are characterized by a nearest neighbor coordination number of $Z_{Ni} = Z_{NiNi} + Z_{HfNi} = 11.8$, the larger Hf atoms exhibit a larger coordination number of $Z_{Hf} = Z_{HfHf} + Z_{HfNi} = 15.7$. This directly implies that not only the chemical but also the topological short-range order around the Ni atoms differs from that around the Hf atoms. Similar differences in the coordination numbers of the different atomic species have also been observed for other glass-forming alloy systems like Ni-Zr and Ni-Nb [4].

Summarizing, we have investigated the short-range order of liquid $Ni_{65}Hf_{35}$ by neutron scattering combined with isotopic substitution. Despite similar atomic radii the short-range order of liquid $Ni_{65}Hf_{35}$ differs from that of liquid $Ni_{64}Zr_{36}$ of similar stoichiometry. This indicates that aspects different from simple arguments of packing, like e.g. chemical or electronic influences, decisively influence the short-range oder of metallic melts. A similar conclusion was drawn from studies on the short-range order of binary Zr-based glass forming melts when exchanging the late transition metal component by atoms of similar size. For instance, it was reported that the short-range order of Zr-Ni melts differs from that of Zr-Cu melts [1].

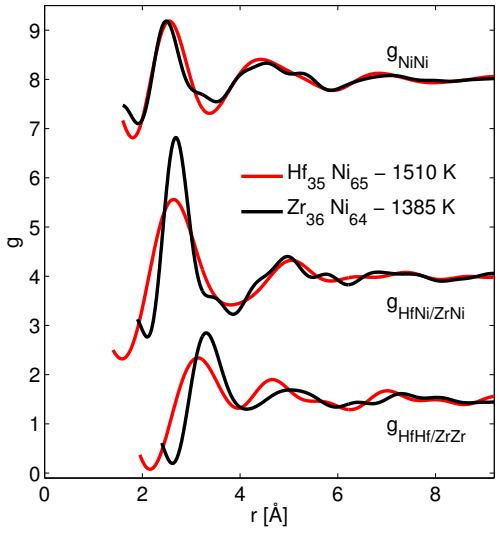

FIG. 1: Partial Faber-Ziman pair correlation functions of liquid $Ni_{65}Hf_{35}$ at T = 1510 K (red) and of $Ni_{64}Zr_{36}$ at $T = 1385$ K (black).

* Corresponding author: dirk.holland-moritz@dlr.de

[1] D. Holland-Moritz et al., EPL **100**, 56002 (2012).
[2] D. Holland-Moritz et al., PRB **79**, 064204 (2009).
[3] S. Klein et al., EPL **102**, 36001 (2013).
[4] D. Holland-Moritz et al., JAP **115**, 203509 (2014).
[5] T. Kordel et al., PRB **83**, 104205 (2011).

Partial Structure Factors Reveal Atomic Dynamics in Metallic Melts

B. Nowak,[1,*] D. Holland-Moritz,[1] F. Yang,[1] Th. Voigtmann,[1,2] T. Kordel,[1] T. Hansen,[3] and A. Meyer[1]

[1] *Institut für Materialphysik im Weltraum, Deutsches Zentrum für Luft- und Raumfahrt (DLR), 51170 Köln, Germany*
[2] *Physik-Department, Heinrich-Heine Universität Düsseldorf, Universitätsstr. 1, 40225 Düsseldorf, Germany*
[3] *Institut Laue-Langevin (ILL), 38042 Grenoble, France*

The dynamical behaviour of individual components in glass-forming metallic liquids varies considerably for differnt systems. One important feature is the dynamical decoupling: the diffusion coefficient of one component is different from that of the others. For binary Zr-Ni melts this effect depends on the composition, since the diffusion of Zr and Ni is equal in $Zr_{64}Ni_{36}$, but becomes decoupled in $Zr_{36}Ni_{64}$ [1]. Up to now the reasons for this behaviour are not understood. Therefore, in this work we investigate how transport properties are correlated to structural features. Mode-coupling theory (MCT) provides predictions about the structure-dynamics relation by using partial structure factors as an input to calculate transport coefficients. Partial structure factors for $Zr_{36}Ni_{64}$, $Zr_{50}Ni_{50}$ and$Zr_{64}Ni_{36}$ have been determined by combining neutron diffraction, electrostatic levitation (ESL) and isotopic substitution [2, 3]. The impact of chemical order has been investigated by using a hard-sphere (HS) model approximation [4]. The self-diffusion coefficients for Zr and Ni calculated by MCT depending on the composition are shown in Fig. 1 (a) as open red triangles respectively circles. The decrease of Ni self-diffusion with increasing Ni concentration is similar to experimental results from quasi-elastic neutron scattering (QNS) (black triangles). The deviation on the absolute scale can be related to the fact that temperature is only an indirect parameter in MCT. However, MCT results are in the Zr-rich composition larger, but in the Ni-rich composition smaller than experimental results. This can be correlated to an increased critical temperature T_C of MCT towards Ni-rich compositions: the error of MCT calculations increases when the temperatures T approaches T_C [5]. Nevertheless, the composition dependent increase of $D_{\mathrm{Ni}}/D_{\mathrm{Zr}}$ towards Ni-rich alloys is observed for experimental tracer measurements as well as MCT calculations (see Fig. 1 (b)). The HS model, where chemical interactions between atoms are neglected, predicts a nearly composition-independent ratio of $D_{\mathrm{Ni}}/D_{\mathrm{Zr}} \approx 2$ (red stars in Fig. 1 (b)). The difference to experimental results respectively MCT calculations in the Zr-rich composition implies that chemical order, neglected by the HS model, plays an important role for the description of the atomic dynamics in liquid Zr-Ni. As a result, strong interactions between Zr and Ni cause an equal diffusion coefficient of Zr and Ni in $Zr_{64}Ni_{36}$ [4]. The increased ratio $D_{\mathrm{Ni}}/D_{\mathrm{Zr}}$ towards Ni-rich melts can be explained by analyzing the structural details, i.e. the fraction of atomic nearest-neighbour pairs. The fraction of Ni-Ni nearest-neighbour pairs (N^{NiNi}) increases continuously (see Fig. 1 (b), blue upright crosses), reaching a value in the Ni-rich alloy which is roughly five times larger as in the Zr-rich composition. The trend is the same as for the ratio $D_{\mathrm{Ni}}/D_{\mathrm{Zr}}$. The interaction between Ni-Ni nearest-neighbour pairs is weaker compared to Zr-Ni pairs. Due to the increase of N^{NiNi} with increasing Ni concentration, there is an increased amount of excess less strongly interacting Ni-Ni pairs of higher mobility in the melt. This leads to a decoupling of the Ni and Zr diffusion when increasing the Ni concentration. These findings are consistent with experimental tracer measurements.

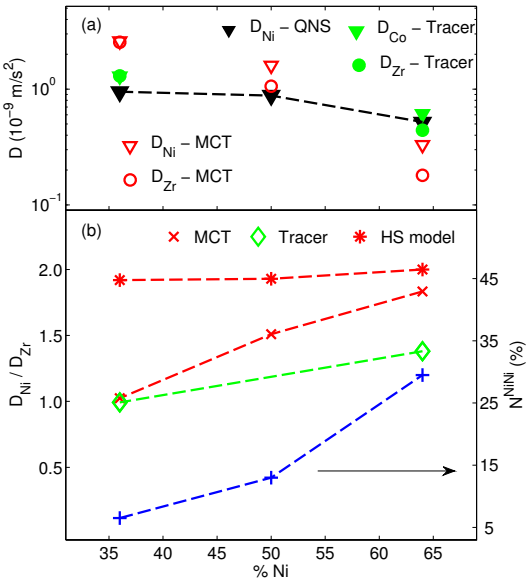

FIG. 1: **(a)** Self-diffusion coefficient of Ni measured by QNS [6] (black triangles) and calculated diffusion coeffiecients of Ni and Zr by MCT (red symbols). Measurments and MCT calculations have been performed at 1380±5 K except for $Zr_{50}Ni_{50}$ (1445 K). Tracer measurements have been carried out for $Zr_{64}Ni_{36}$ and $Zr_{36}Ni_{64}$ at 1388 K (green symbols) [1]. **(b)** Ratio $D_{\mathrm{Ni}}/D_{\mathrm{Zr}}$ out of MCT calculations depending on the composition as well as for HS model approximation. The blue upright crosses are the fraction of atomic nearest-neighbour pairs N^{NiNi}. Lines are guides to the eye.

The above considerations base only on the short-range order as described by partial structure factors. This averaged structural information is able to explain the observed atomic dynamics and hence specific structural arrangements are of minor importance.

* Corresponding author: benedikt.nowak@dlr.de

[1] S. W. Basuki et al., to be published.
[2] D. Holland-Moritz et al., Phys. Rev. B **79**, 064204 (2009).
[3] T. Kordel et al., Phys. Rev. B **83**, 104205 (2011).
[4] Th. Voigtmann et al., EPL **82**, 66001 (2008).
[5] P. Kuhn et al., Phys. Rev. B **90**, 024309 (2014).
[6] D. Holland-Moritz et al., Journal of Physics: Conf. Ser. **144**, 012119 (2009).

Diffusion of mass in Al-rich Al-Ni melts

E. Sondermann,* F. Kargl, and A. Meyer

Institut für Materialphysik im Weltraum, Deutsches Zentrum für Luft- und Raumfahrt (DLR), 51170 Köln, Germany

Diffusion of mass in liquid alloys impacts on the formation and evolution of microstructure during solidification. Cast aluminum alloys contain low concentrations of different alloying elements. Using experimental data, we investigate, whether at low concentrations interdiffusion coefficients can be derived directly from self-diffusion coefficients, or whether cross correlations still impact interdiffusion [1].

Classical interdiffusion measurements using the long capillary technique can be disturbed by effects due to melting and solidification, buoyancy-driven convection and Marangoni-convection.We combine X-ray radiography (XRR) with the shear-cell method, where samples with different concentrations are melted separately and only brought together, after temperature and concentration distribution are homogenized. This prevents segregation and mixing of alloys during heating. XRR allows to detect free surfaces, which cause Marangoni-convection. To suppress buoyancy-driven convection, such measurements were also conducted on the sounding rocket MAPHEUS-4 at a microgravity level better than 10^{-4}g.

Self-diffusion coefficients were measured by quasi-elastic neutron scattering (QENS). This method uses the fact, that the elastic signal of the incoherent intermediate scattering function is broadened by the diffusive motion in liquids. Experiments were conducted at the time-of-flight spectrometer TOFTOF at the neutron source FRM II in Garching, near Munich.

As shown in Fig. 1, Ni-self-diffusion coefficients at 1173 K decrease with increasing Ni-content while D_{AlNi} is mostly constant for Ni-concentrations between 1 and 14 at.% Ni. On ground buoyancy may lead to disturbing convection, but density layering can have a stabilizing effect. In contrast, under microgravity density driven convection is greatly reduced, but persisting convection cannot be damped by density layering. Microgravity experiments, shown as stars in Fig. 1, agree with ground based results within error bars. This confirms, that the diffusion data are undisturbed by convection.

The cross correlation term S is calculated using the Darken-Manning equation

$$D_{\mathrm{AlNi}} = S\Phi(c_{\mathrm{Ni}}D_{\mathrm{Al}} + c_{\mathrm{Al}}D_{\mathrm{Ni}}). \qquad (1)$$

taking the thermodynamic factor Φ from literature.

The determined cross correlation term is below unity, which is typical for systems exhibiting a chemical short-range order. Although $S \to 1$ is expected for $c_{\mathrm{Ni}} \to 0$ the cross correlation term is considerably below unity even at a concentration as low as 2 at.% Ni.

In the temperature range $1033 \leq T \leq 1273$ K the interdiffusion coefficient in $Al_{95}Ni_5$ is slightly lower

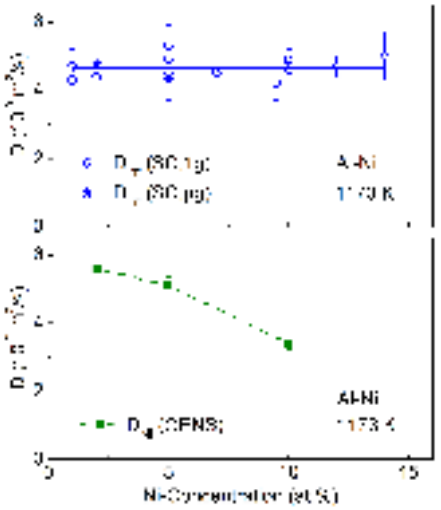

FIG. 1: Top: Interdiffusion coefficients with mean value as solid line as a function of Ni-concentration. Bottom: Self-diffusion coefficients for nickel as a function of Ni-concentration.

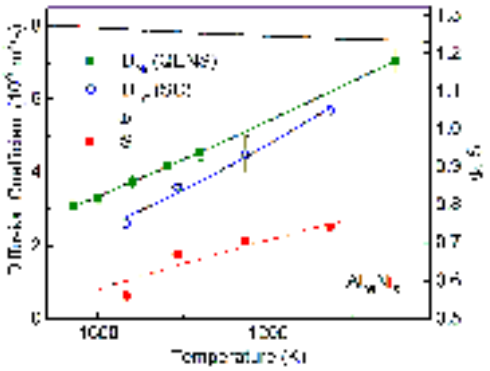

FIG. 2: Self- and interdiffusion coefficients of $Al_{95}Ni_5$ as a function of temperature. Solid lines are fits with the Arrhenius function. Also shown are the thermodynamic factor Φ calculated from literature and the cross correlation term S resulting from experimental values.

than D_{Ni} as can be seen in Fig. 2. The temperature dependence of Ni-self-diffusion and interdiffusion can be well described by the Arrhenius function $D = D_0 \exp(-Q/k_B T)$ with an activation energy Q and a prefactor D_0.

While the thermodynamic factor decreases slightly with temperature, the cross correlation term increases. This means, the influence of cross correlations on interdiffusion decreases as the temperature increases.

* Corresponding author: elke.sondermann@dlr.de

[1] E. Sondermann, F. Kargl and A. Meyer, Phys. Rev. B. **93**, 184201 (2016).

Studying thermodiffusion in liquid alloys by X-ray radiography

E. Sondermann,* F. Kargl, and A. Meyer

Institut für Materialphysik im Weltraum, Deutsches Zentrum für Luft- und Raumfahrt (DLR), 51170 Köln, Germany

Thermodiffusion (also called Soret effect) describes the formation of a concentration gradient induced by a temperature gradient in multicomponent mixtures. This phenomenon is widely studied in aqueous liquids but experimental data for liquid metal alloys are scarce. The study of thermodiffusion in liquid metal alloys contributes towards a better understanding of microscopic processes as e. g. microstructure formation on solidification. Furthermore, this effect can be exploited for the separation of isotopes as well as separating the compounds of an alloy.

In recent years improved theories and simulations were developed for thermodiffusion in liquid alloys but their verification is hampered by the low number of reliable data. Molecular dynamic simulations [1, 2] on thermodiffusion in liquid Al-Ni showed that such simulations are very sensitive to the potential used. Depending on the details of the potential even the direction of the thermodiffusion effect can alter its direction.

Conventional experiments where a heating step to target temperature is followed by annealing and solidification upon cooling are perturbed by additional mass transport outside of the annealing phase. This can be overcome by in-situ observation of the process as implemented for organic liquids using Mach-Zehnder interferometry. For non-transparent metal systems a different technique has to be chosen. We use X-ray radiography (XRR) to determine the concentration distribution in the liquid state. This technique proved to be a powerful tool in the measurement and process control in recent chemical diffusion studies on liquid alloys [3].

We use a high temperature furnace consisting of an Al_2O_3-tube with volume compensation to contain the sample. The furnace has two independently controlled heating zones enabling to set up a temperature gradient.

FIG. 1: X-ray image of the liquid sample (dark rod in the lower center) inside the furnace. No free surfaces or bubbles were observed in the sample. The heating wires of the two independently controlled heating zones can be seen as well.

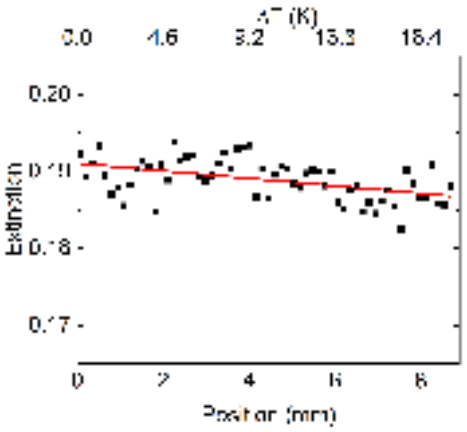

FIG. 2: Extinction as a function of position with linear fit (red line). Higher extinction means higher Ni-content. Therefore it can be concluded that nickel migrates to the colder side.

For binary alloys, the variation of extinction of the X-rays along the rod-shaped sample can be used to determine the direction of the Soret-effect. With appropriate references it will also be possible to determine the concentration profile and calculate the Soret coefficient. In order to obtain a clearly visible concentration gradient, the temperature gradient should be in the order of 5 K/mm. However, a high temperature gradient may lead to buoyancy-driven convection in ground based experiment.

A first experiment on $Al_{78.5}Ni_{21.5}$ clearly shows that nickel diffuses to the cold side. Reversing the direction of the temperature gradient led to a reversion of the the concentration gradient. This shows that it is not a pure sedimentation effect. However, the reversed concentration gradient is less steep which is probably due to the now unstable density layering causing convection.

To obtain benchmark values for the Soret coefficient in liquid alloys we therefore propose to conduct measurements employing XRR in a microgravity environment.

* Corresponding author: elke.sondermann@dlr.de

[1] E. Levchenko, A. Evteev, T. Ahmed, A. Kromik, R. Kozubski, I. Belova, Z.-K. Liu and G. Murch, Phil. Mag. **124**, 54 (2016).

[2] W. Tucker and P. Schelling, Comp. Mat. Sci. **96**, 3054 (2016).

[3] B. Zhang, A. Griesche and A. Meyer, Phys. Rev. Lett. **104**, 35902 (2016).

Composition induced structure change in binary La-based glass-forming melts

Z. Wang,* F. Yang, and A. Meyer

Institut für Materialphysik im Weltraum, Deutsches Zentrum für Luft- und Raumfahrt (DLR), 51170 Köln, Germany

The limited plasticity before catastrophic failure is a long-standing conundrum hindering the wide application of metallic glasses (MGs). Recent study found that the local relaxation behavior can strongly affect the heterogeneous deformation in MGs, even dominate the mechanical performance at room temperature [1]. Furthermore, the local relaxation behavior is also considered to be related with regions of weakly bonding and rich of free volume in MGs. Therefore, altering the local relaxation behavior may provide a practical option to tune the mechanical performance of MGs. For La-based MGs, replacing transition metals Ni and Co with similar sized Cu will bring along a different local relaxation behavior, absent of a separate beta-relaxation peak in the glass state [2]. The reason behind it is still unclear yet but is suspected to be related with chemical interaction effects. Here, we look into these binary La-based glass-forming melts, trying to find out some clue rooted in their liquid structures.

Using the newly developed containerless electrostatic levitation (ESL), densities of these La-based melts can be precisely measured. The excess volume of La-TM alloys is then derived by comparing that with the molar volume of an ideal mixing behavior of the pure elements, as shown in Fig. 1. Interestingly, a positive excess volume is found in La-Cu melts, compared to negative excess volume in La-Ni/Co melts. Consider that these TMs all having similar atomic radii, a relatively loose packing in La-Cu melts is expected.

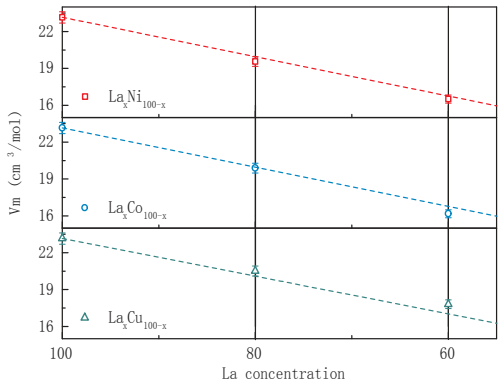

FIG. 1: *Vm* measured at 1073 K for binary La-TM melts. Dashed lines represent values of *Vm* calculated assuming an ideal mixing behaviour.

Further combine ESL with *in-situ* synchrotron X-ray diffraction, total structure factor *S(Q)* of the melts can be obtained to analyse the microscopic structure, as described before [3]. Measured *S(Q)* of $La_{60}Cu_{40}$ is found to be relatively flat above the first peak. Considering that Ni/Co/Cu all exhibit very similar X-ray scattering cross sections, such phenomena should stem from the different structure of the melt. However, *S(Q)* are a sum of partial structure factors contributed by all atomic pairs. To explore the role of a specific atomic pair, we use RMC simulation to retrieve atomic structure of the melt. The computed *S(Q)* curves can perfectly coincide with experiments as shown in Fig. 2.

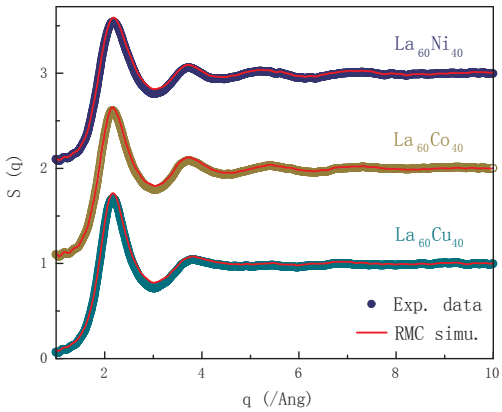

FIG. 2: *S(Q)* measured at 1073 K for binary La-TM melts. Red lines are RMC simulated curves.

From the partial PDFs (PPDFs) calculated from simulated configurations, the biggest difference among these three melts is found in La-TM PPDFs. The peak shape of $La_{60}Cu_{40}$ is wider and distinct from the other two melts. The first peak position of La-Cu PPDFs is also closer to its Goldschmidt radii. The shorter distance compared to Goldschmidt radii implies a strong chemical interaction in La-TM melts, which is more obvious for La-Ni and La-Co. Furthermore, average coordination number (CN) is 10.23 for $La_{60}Cu_{40}$, which is smaller compared to 11.27 for $La_{60}Ni_{40}$ or 11.60 for $La_{60}Co_{40}$. Smaller CN also indicates a relative loose packing in $La_{60}Cu_{40}$, as expected from excess volume difference discussed before.

In short, the structure and atomic packing of La-TM melts will change with different TM element, which is mainly introduced by chemical interactions between La and Ni/Co/Cu. Relatively loose packing and distinct chemical environment of La-Cu melts may also relate with its extraordinary relaxation behavior in the glass state, compared to La-Ni/Co.

* Corresponding author: `z.wang@dlr.de`

[1] Z. Wang, B. A. Sun, H. Y. Bai and W. H. Wang, Nat. Commun., **5**, 5823 (2014).
[2] Z. Wang, H. B. Yu, P. Wen, H. Y. Bai, and W. H. Wang, J. Phys. Condens. Matter, **23**, 142202 (2011).
[3] D. Holland-Moritz, F. Yang, T. Kordel, S. Klein, F. Kargl, J. Gegner, T. Hansen, J. Bednarcik, I. Kaban, O. Shuleshova, N. Mattern, and A. Meyer, EPL, **100**, 56002 (2012).

Normal spectral emissivity and heat capacity measurements of liquid Al-Ti alloys

J.J. Wessing,[1,*] J. Brillo,[1] H. Kobatake,[1] and H. Kobatake[2]

[1] *Institut für Materialphysik im Weltraum, Deutsches Zentrum für Luft- und Raumfahrt (DLR), 51170 Köln, Germany*
[2] *Fukuyama lab, IMRAM, Tohoku University, Sendai, Japan*

For normal spectral emissivity and heat capacity measurements similar levitation techniques were used as for surface tension measurements. Moreover, melt convections such as buoyancy and Marangoni convections induced by nonuniform temperature distributions and observed in electromagnetically levitated samples had to be taken into account as they may significantly influence the caloric measurement results. The measurements were carried out at Fukuyama lab at the Tohoku University, Japan where Kobatake and Fukuyama et al. developed a technique combining EML with noncontact modulated laser calorimetry with the use of a static magnetic field to suppress transitional motions, surface oscillations, and melt convection in the materials [1].

Emissivity of liquid metals, as well as heat capacity and thermal conductivity are among the properties used as input data for numerical simulations. Furthermore, the emissivity is indispensable for the determination of heat capacity and thermal conductivity. The normal spectral emissivity is defined as the ratio of the normal spectral radiance emitted from the sample, $R_s(\lambda, T)$, to the theoretical blackbody radiance from Planck's law, $R_b(\lambda, T)$, at the same wavelength, λ and temperature, T. Thus, the normal spectral emissivity can be obtained by directly measuring the radiance emitted from a molten droplet as a function of the wavelength and temperature using a spectrometer. For heat capacity the temperature response at the bottom surface of the droplet is measured using a single colour pyrometer, where the temperature amplitude ΔT_{ac} and the phase shift φ between the laser signal and temperature response are expressed as follows [2]:

$$\Delta T_{ac} = \frac{\beta}{\omega C_p}\left(1 + \frac{1}{\omega^2 \tau_c^2}\right)^{-1/2} = \frac{\beta}{\omega C_p} f$$

Therein, ω is angular heating frequency of the laser, f signifies a correction function, Cp represents the isobaric heat capacity, $\tau_r(s)$ and $\tau_r(c)$ denote the internal and external thermal relaxation time attributable to both the radiative and the conductive heat transfer in the ambient gas.The term β is evaluated quantitatively using the products of the laser power and the absorptivity. The latter is obtained from normal spectral emissivity at 940 nm assuming Kirchhoff's law.

The normal spectral emissivity and heat capacity were measured for Ti, $Al_{20}Ti_{80}$, $Al_{50}Ti_{50}$ and $Al_{70}Ti_{30}$. Fig. 1 presents the average normal spectral emissivity of liquid Ti as a function of wavelength over experimental temperatures of 1930-1980 K, covering the melting point of 1941 K. Within the measured frequency range and experimental error of 2.2 the temperature dependence is negligible, as reported by Takasuka et al [3] and exhibits a value of 0.37 for a 940 nm laser wavelength.

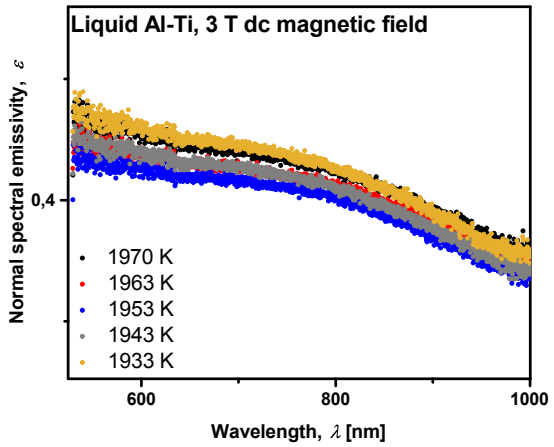

FIG. 1: Normal spectral emissivity of liquid Ti.

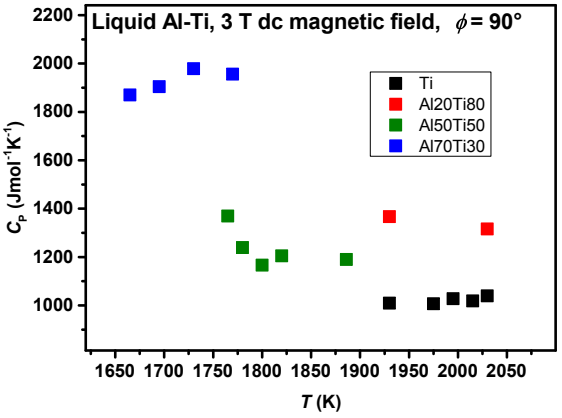

FIG. 2: Temperature dependent heat heat capacity of liquid Al-Ti alloys.

Fig. 2 depicts the isobaric molar heat capacity of liquid Al-Ti alloys. No pronounced temperature dependencies were observed in the experimental temperature range. The largest values for the heat capacity were found for $Al_{70}Ti_{30}$ of about 1927 J/(molK) and the lowest for pure Ti of about 1020 J/(molK).

* Corresponding author: johanna.wessing@dlr.de

[1] H. Fukuyama, K. Takahashi, S. Sakashita, H. Kobatake, T. Tsukada,and S. Awaji, ISIJ Int. **49**, 1436–42 (2009).
[2] K. Yamamoto, T. Abe and S. Takasu, J. Appl. Phys. **30**, 2423-6 (1991).
[3] E. Takasuka, E. Tokisaki, K. Terashima and S. Kimura, Proc. 4th. Asian Thermophys. Prop. Conf. **B1d3**, 89-92 (1995).

Thermophysical properties of liquid Al-Ti alloys and influence of the oxygen partial pressure

J.J. Wessing* and J. Brillo

Institut für Materialphysik im Weltraum, Deutsches Zentrum für Luft- und Raumfahrt (DLR), 51170 Köln, Germany

Al-Ti-based alloys are of enormous technical relevance due to their specific properties. For studies in atomic dynamics and industrial processing the precise knowledge of the thermophysical properties of the liquid phase is crucial, as the vast majority of materials are directly produced from the melt by casting [1]. Among the properties relevant, emissivity, heat capacity and surface tension of the liquid phase are of pronounced importance. Due to the high chemical reactivity of liquid Al and Ti paired with a large solubility of oxygen data on these properties of Ti-based alloys are sparse. Therefore, electromagnetic levitation techniques (EML) are used which enable contact free and containerless processing. The effect of oxygen can be especially pronounced with regards to the surface tension of metals and previous studies have suggested that especially Ti melts might be sensitive to oxygen impurities due to the high oxygen solubility in liquid Ti [2]. This may lead to a reduced surface tension of liquid Ti and could also affect the surface tension of Al-Ti alloys. In this study we present Ti surface tension results in dependence of the oxygen partial pressure in the sample surrounding atmosphere. According to Cummings and Blackburn [3], the surface tension can be expressed using the oscillation frequencies of the liquid samples as follows:

$$\sigma = \frac{3M}{160\pi} \sum_{m=-2}^{2} {\omega^2}_m - 1.9\Omega^2 - 0.3(\frac{g}{a})^2\Omega^{-2}$$

where M is the sample mass, a is the sample radius, g is the gravitational acceleration, and Ω is a correction term which can be calculated from the translational frequencies. High purity Ar and He gases with a purity of 99.999 and Titanium and Magnesium sublimation pumps were used to reduce the oxygen partial pressure in the chamber previous to the measurements.
The measurements carried out at DLR, shown in Fig. 1, represent surface tension, γ measurements at constant temperatures in dependence of the oxygen partial pressure PO_2 monitored and actively set, using an oxygen partial pressure control and sensor system (OSC). Unexpectedly, the surface tension of pure Ti stays constant over a brought PO_2 range. Only by chemically adding additional oxygen in form of TiO_2 a significant effect on the surface tension could be observed. With increasing chemical content of oxygen the surface tension decreases.
For the measurements carried out at Fukuyma lab, Tohoku University, Japan, the surface tension was measured time dependent at low PO_2 values of about 10^{-22} Pa, as depicted in Fig. 2. Additionally, the oxygen content of four samples was chemically analyzed after certain measurement times. With continuous measurement time the surface tension first decreases and then

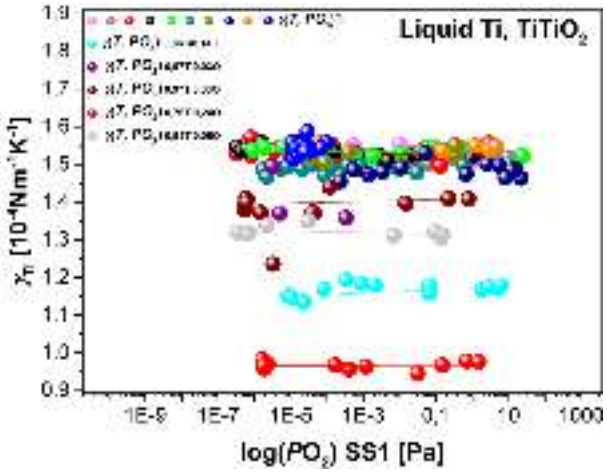

FIG. 1: Surface tension of liquid Ti and TiTiO2 alloys in dependence of oxygen partial pressure.

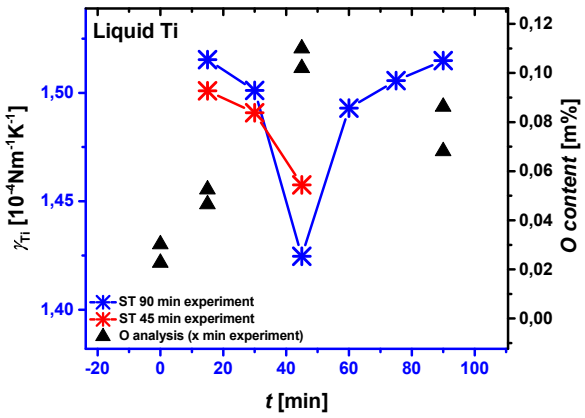

FIG. 2: Time dependent surface tension and oxygen content of liquid Ti.

increases again while the oxygen content increases initially and then decreases slightly. The decrease in the surface tension might be caused by an enrichment of dissolved oxygen in the sample, which, here, equals an higher oxygen content. The increase of the surface tension after around 45 min could indicate some interactions between the bulk and the surface of the sample.

* Corresponding author: johanna.wessing@dlr.de

[1] I. Egry,R. Brooks,H. Moritz,R. Novakovic,T. Matsushita,E. Ricci,S. Seetharaman,R. Wunderlich and D. Jarvis, Int. J. Thermophys. **28**, 1026-36 (2007).
[2] L. Belyanchikov, Russ. Metall. Thermophys. **12**, 1156–1163. (2010).
[3] D. Cummings and D. Blackburn, J. Fluid. Mech. **224**, 395-416 (1991).

Correlation between melt viscosity and glass forming ability of Zr-Ni-Al alloys

M. Seidel,[1] F. Yang,[1,*] S. T. Liu,[1,2] C. C. Yuan,[1] and A. Meyer[1]

[1] *Institut für Materialphysik im Weltraum, Deutsches Zentrum für Luft- und Raumfahrt (DLR), 51170 Köln, Germany*
[2] *Institute of Physics, Chinese Academy of Science, Beijing 100190, People's Republic of China*

Bulk metallic glasses (BMGs) are promising engineering materials for various applications, owing to the unique properties emerged from their amorphous structure. one of the most common approaches to optimise the properties of BMGs is to tune the composition. A special issue here, in contrast to conventional metallic alloys, is the (composition dependent) glass forming ability (GFA). With a few exceptions, while pure metals and binary alloys are usually poor glass formers, alloying a third component can already significantly improves the GFA of the melt. In some cases, even a small amount of an extra component can have large impacts.

Aluminium is a commonly used element for improving the GFA of the melt. For example, starting from the binary Zr-Ni alloys, alloying Al lead to initially a significant increase of the GFA, resulting in the best glass former with a composition close to $Zr_{75}Ni_{25}Al_{15}$. However, the GFA decreases with the further increase of the Al content [1]. This is a typical case showing that the mechanism of the improved GFA upon elements addition is complex and not well understood. Most of the empirical criteria are based on thermodynamic considerations, e.g.: the formation of deep eutectic compositions or as a scavenging agent which removes harmful impurities. However, little attention has been paid to the composition dependent liquid dynamics, which is another important aspect of glass formation.

We present here an investigation of a series of liquid Zr-Ni-Al alloys $Zr_{75-x}Ni_{25}Al_x$ with $0 \leq x \leq 30$, i.e.: a systematic substitution of Zr with Al [2]. Using the containerless processing technique of electrostatic levitation (ESL), we were able to precisely determine the density and viscosity of these chemically highly reactive liquids, accessing deep undercooling without any artefacts caused by sample-container reactions. We hence studied the correlation between viscosity, packing fraction, and the GFA of these melts.

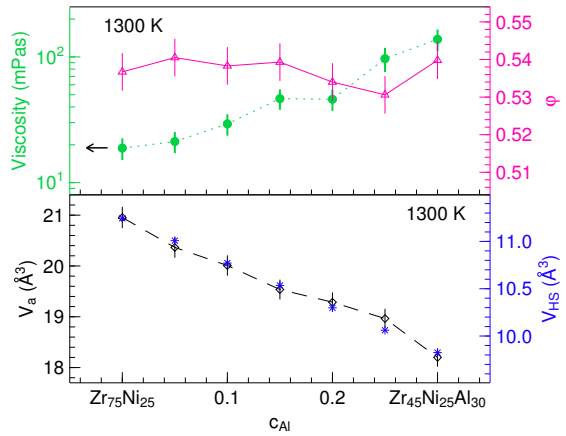

FIG. 1: Composition dependent melt viscosity (full dots) of the binary and ternary Zr-Ni-(Al) alloys as a function of Al content at 1300 K. The molar volume (open diamonds), the packing fraction (triangles) derived from the measured liquid density, and the average hard-sphere atomic volume (stars) at the same temperature are also shown from comparison.

The addition of Al causes a monotonic increase of the melt viscosity, as shown in Fig. 1 for 1300 K, notable already at 5 at% Al. However, the packing fraction $\varphi = V_{\mathrm{HS}}/V_a$, derived by assuming a hard-sphere (HS) like packing, stays almost constant. This is due to the fact that the molar (atomic) volume volume $V_a = \rho N_A/\overline{M}$ and the average HS volume $V_{\mathrm{HS}} = \frac{4}{3}\pi\overline{r^3}$ exhibit very similar composition dependence. Thus, in contrast to the binary Zr-(Ni,Cu) and the NiPd-based melts, a qualitative correlation between higher packing fraction and slower liquid dynamics cannot be found here. This indicates that the liquid dynamics is not only controlled by geometrical packing, but also by the chemical interaction between the alloy components.

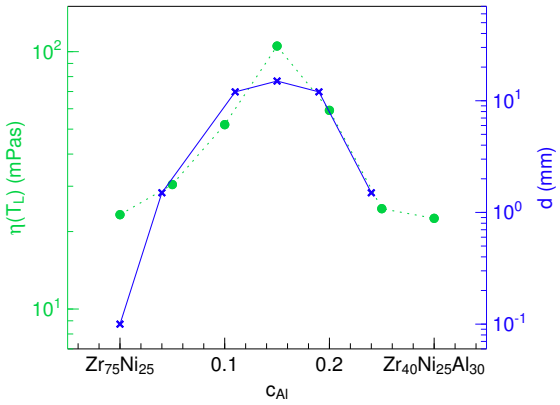

FIG. 2: Correlation between the melt viscosity at the respective liquidus temperature (full dots) and the critical casting thickness of fully amorphous samples (crosses) of the Zr-Ni-Al alloys as a function of the Al content [1].

On the other hand, whereas the liquid viscosity increases with increasing Al content, the viscosity at the respective liquidus temperatures, exhibits a maximum ∼15 at% Al, as shown in Fig. 2. Thus, in this composition range, the GFA seems to be well correlated with the liquid viscosity. This shows that the melt dynamics plays an important role during the glass formation. The improvement of the GFA upon Al addition, with an optimum close to 15 at% Al, can be understood as a result of the interplay between liquid dynamics and the temperature where the melt falls out of equilibrium.

* Corresponding author: `fan.yang@dlr.de`

[1] Y. Li, W. Zhang, C. Dong, J. Qiang, A. Makino, and A. Inoue, Intermetallics **18**, 1851 (2010).
[2] M. Seidel, Master Thesis, Uni Münster (2016).

Atomic dynamics in Zr-based glass forming alloys near the liquidus temperature

S. W. Basuki,[1] F. Yang,[2,*] E. Gill,[1] K. Rätzke,[1] A. Meyer,[2] and F. Faupel[1]

[1] *Institut für Materialwissenschaft – Lehrstuhl für Materialverbunde, Technische Fakultät, Christian-Albrechts-Universität zu Kiel, 24143 Kiel, Germany*

[2] *Institut für Materialphysik im Weltraum, Deutsches Zentrum für Luft- und Raumfahrt (DLR), 51170 Köln, Germany*

How atomic transport in liquid depends on the atomic size, mass, and the liquid composition is of both technological and physical importance. Strong component decoupling is expected to set in as the liquid enters the supercooled regime, where the atomic transport becomes more correlated. This has been frequently interpreted as evidences of dynamic heterogeneity, which is considered to be one of origins of the glass forming ability (GFA) of alloy melts exhibiting only weak, non-directional metallic bondings between the atoms.

However, in a Zr-based multicomponent bulk glass forming liquid $Zr_{46.75}Ti_{8.25}Cu_{7.5}Ni_{10}Be_{27.5}$ (Vit4), a significant component decoupling was observed, extending even into the equilibrium melt. The Zr and Ni self-diffusion coefficients differ by a factor of 4 at the liquidus temperature [1]. In order to understand the origin of this strong decoupling, particularly its correlation with the number of components of the melt and the GFA, we studied the component decoupling in the binary $Zr_{64}Ni_{36}$ and $Zr_{36}Ni_{64}$, as well as the ternary $Zr_{60}Ni_{25}Al_{15}$ alloy melts [2].

Radiotracer technique was applied to measure the Co and Zr diffusion coefficients in the binary $Zr_{64}Ni_{36}$, $Zr_{36}Ni_{64}$, and $Zr_{60}Ni_{25}Al_{15}$ liquids. Co tracer is considered to behave very similarly as Ni, and hence represents here the Ni self diffusion. Combining QNS and radiotracer technique, the obtained diffusion coefficients by radiotracer technique can be compared with that measured by QNS, to rule out the influence of any convective flow and other experimental artifacts. On the other hand, while the study of self diffusion by QNS measurements is limited to elements with sufficient large incoherent neutron scattering cross sections like Ni, radiotracer technique, especially the co-diffusion measurement performed here allows simultaneously measurements of Zr and Ni diffusivities, and hence directly studying the component decoupling.

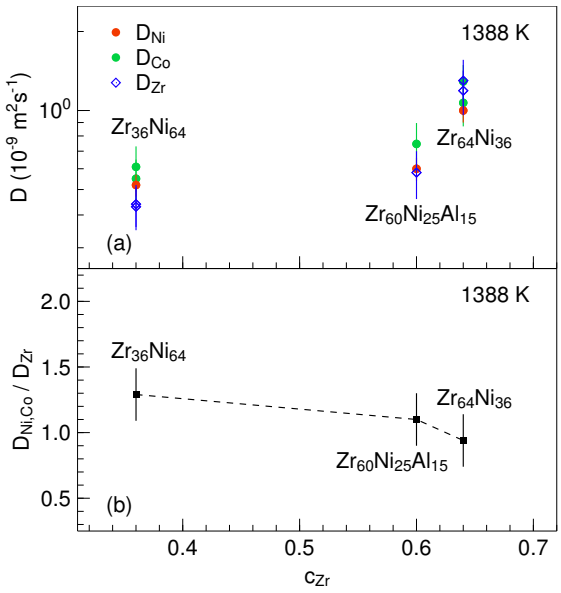

FIG. 1: (a) Measured self diffusion coefficients in the binary $Zr_{64}Ni_{36}$ and $Zr_{36}Ni_{64}$, as well as the ternary $Zr_{60}Ni_{25}Al_{15}$ alloy melts at 1388 K. (b) The ratio between the Ni and Zr self diffusion coefficients in these melts as a function of Zr content. The dashed line is a guide to eyes.

The measured Ni self diffusion coefficient by QNS, and the Co and Zr diffusivities for $Zr_{64}Ni_{36}$, $Zr_{36}Ni_{64}$, and $Zr_{60}Ni_{25}Al_{15}$ at 1388 K are shown in Fig. 1a. The Co self diffusion coefficient obtained by the radiotracer measurements agrees with the Ni diffusion coefficient measured by QNS within the experimental uncertainty, showing that the results are free of artifacts. The Ni self diffusion in the $Zr_{64}Ni_{36}$ melt is faster than that in the $Zr_{36}Ni_{64}$ melt, which can be understood by the higher packing fraction in the $Zr_{36}Ni_{64}$ melt. The addition of Al is known to result in slower atomic dynamics in the $Zr_{60}Ni_{25}Al_{15}$ melt compared to that in $Zr_{64}Ni_{36}$ [3].

Comparing the Zr and Ni self diffusion coefficients, we observed a small, but notable composition dependence of the component decoupling in these alloys, as shown in Fig. 1b. Whereas in the $Zr_{36}Ni_{64}$ melt Zr diffuse by about a factor of 1.3 slower than Ni, the self diffusion coefficient of Zr and Ni is almost identical in the $Zr_{64}Ni_{36}$ and $Zr_{60}Ni_{25}Al_{15}$ melts with higher Zr content. Such component decoupling cannot be explained by the atomic size difference only, but the strong chemical affinity between Zr and Ni plays an important role: At high Zr content, all Ni atoms in the melt are coupled with the Zr atoms, leads to similar diffusion coefficients. In contrast, for the Ni rich composition, the reduced number of Zr-Ni pairs results in a larger decoupling between the Zr and Ni diffusion.

For the multicomponent alloys, the small component decoupling in the ternary $Zr_{60}Ni_{25}Al_{15}$ liquid can also be understood by the strong affinity between the three alloy components. In this sense, the large component decoupling observed in the Vit4 liquid might not be due its (increased) number of components, but is a consequence of the lower Zr content. This requires however further experimental verification.

* Corresponding author: `fan.yang@dlr.de`

[1] S. W. Basuki, A. Bartsch, F. Yang, K. Rätzke, A. Meyer, and F. Faupel, Phys. Rev. Lett. **113**, 165901 (2014).

[2] S. W. Basuki, F. Yang, E. Gill, K. Rätzke, A. Meyer, and F. Faupel, submitted to Phys. Rev. B.

[3] C. C. Yuan, F. Yang, F. Kargl, D. Holland-Moritz, G. G. Simeoni, and A. Meyer, Phys. Rev. B **91**, 214203 (2015).

Relation between Self-Diffusion and Viscosity in Liquid $Ni_{66.7}B_{33.3}$

S. Zimmermann,[1,*] F. Yang,[1] Z. Evenson,[2] and A. Meyer[1]

[1] *Institut für Materialphysik im Weltraum, Deutsches Zentrum für Luft- und Raumfahrt (DLR), 51170 Köln, Germany*
[2] *Forschungsneutronenquelle Heinz Maier-Leibnitz, FRM II, Technische Universität München, 85747 Garching, Germany*

The viscosity η describes the macroscopic transport of momentum by the collective motion of the particles in a liquid. The diffusion D describes a single-particle diffusive transport. In a liquid, usually both are linked by the phenomenological Stokes-Einstein relation [1]. This equation is based on a model of a large sphere immersed in a fluid and moving in it due to the brownian motion of the solvent molecules. In order to calculate required diffusion coefficients from viscosities, or vice versa, Stokes-Einstein equation is often taken as:

$$D = \frac{k_B T}{6\pi r_H \eta}. \qquad (1)$$

Here, r_H is the hydrodynamic radius, T is the absolute temperature and k_B is the Boltzmann constant.
In $Zr_{64}Ni_{36}$ it has been however observed that $D\eta$ = const. in contrast to the Stokes-Einstein relation (equation 1) but in line with Mode-Coupling-Theory (MCT) predictions [2]. In order to study wether other metallic melts also exhibit similar behaviour we investigated the viscosity and the self-diffusion coefficient of nickel D_{Ni} in $Ni_{66.7}B_{33.3}$. This alloy is of great interest due to its lower packing fraction compared to $Zr_{64}Ni_{36}$. D_{Ni} was obtained from quasielastic neutron scattering (QNS) experiments on the time-of-flight spectrometer TOFTOF at FRM II. One of the great benefits of the QNS measurement is that the liquid dynamics is probed on microscopic time scales where convection does not affect the results. Figure 1 shows the Ni self-diffusion coefficient of $Ni_{66.7}{}^{11}B_{33.3}$ as a function of temperature. The liquid viscosity and density of this binary alloy have been measured using electrostatic levitation (ESL) technique, which allows measuring thermophysical properties in undercooled melts, since heterogeneous nucleation sites are absent. The viscosity η of $Ni_{66.7}B_{33.3}$ was determined using the oscillating drop technique. Figure 1 shows the data in the temperature range between 1300 K and 1650 K.

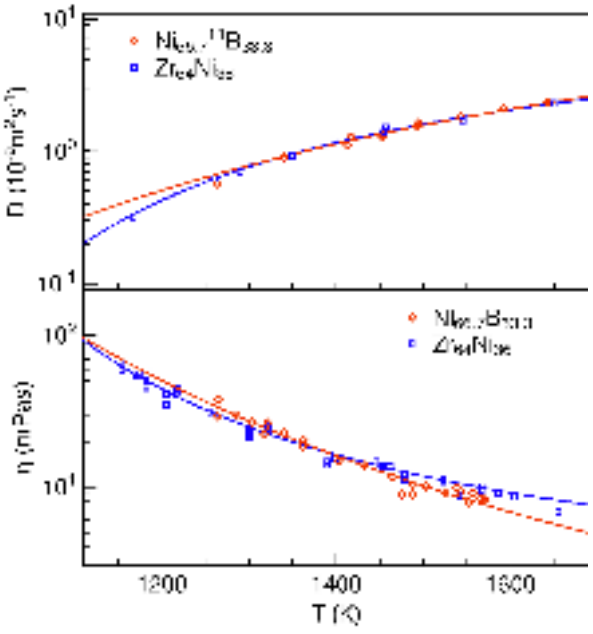

FIG. 1: T dependent Ni self-diffusion coefficient (top) and viscosity (bottom) of $Ni_{66.7}B_{33.3}$ (red squares) and $Zr_{64}Ni_{36}$ [2] (blue diamonds). Corresponding fits of the Vogel-Fulcher-Tammann (VFT) law (solid lines).

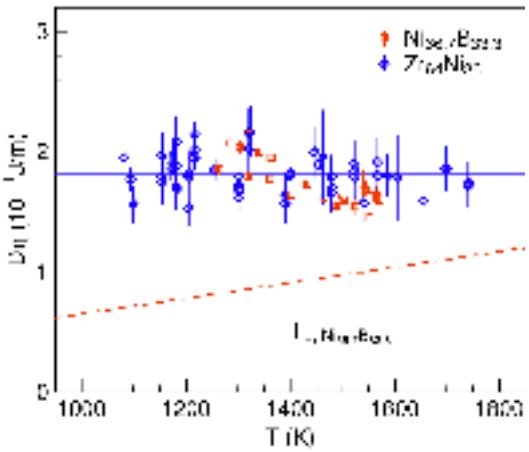

FIG. 2: $D\eta$ of $Ni_{66.7}B_{33.3}$ (red squares) and $Zr_{64}Ni_{36}$ [2] (blue diamonds) as a function of temperature T. The linear fit of the data of $Zr_{64}Ni_{36}$ (solid blue line) is a guide for the eye. The red dashed line correspond to the Stokes-Einstein relation [1] with the hydrodynamic radius $r_H = c_{Ni} r_{Ni} + c_B r_B$.

It is found that both the Ni self-diffusion coefficient and the viscosity of the $Ni_{66.7}B_{33.3}$ melt are similar to that of liquid $Zr_{64}Ni_{36}$ within the experimental uncertainties (see Fig. 1). Figure 2 shows the product of $D\eta$ which indicates that $Ni_{66.7}B_{33.3}$ exhibits a similar trend like $Zr_{64}Ni_{36}$. The red dashed line in figure 2 shows the Stokes-Einstein relation (equation 1) with $r_H = c_{Ni} r_{Ni} + c_B r_B$ with $r_{Ni} = 1.15$ Å, $r_B = 0.8$ Å, $c_{Ni} = 0.667$ and $c_B = 0.333$. The experimental data are underestimated by more than a factor of 2 and also the dependence of the temperature differs.
Further investigations are necessary to examine the relation between self-diffusion and viscosity in liquid $Ni_{66.7}B_{33.3}$. Therefore, the data of D as well of η must be obtained within a larger temperature range.

* Corresponding author: sarah.zimmermann@dlr.de

[1] A. Einstein, Investigation on the theory of the Brownian-movement, (Dover, New York, 1926).
[2] J. Brillo, A. I. Pommrich, and A. Meyer, Phys. Rev. Lett. **107**, 165902 (2011).

1.3 Solidification, Nucleation and Growth

In-situ solute measurement in an Al-Ge alloy using polychromatic X-radiography

M. Becker,[1,*] S. Klein,[1,2] and F. Kargl[1]

[1] *Institut für Materialphysik im Weltraum, Deutsches Zentrum für Luft- und Raumfahrt (DLR), 51170 Köln, Germany*
[2] *Deutsche Gesellschaft für Materialkunde (DGM), Hahnenstr. 70, 60528 Frankfurt am Main, Germany*

In solidification research great effort has been made to understand the growth mechanisms of metallic alloys. Especially for casting applications modelling of equiaxed dendrites in undercooled melts is of great interest. To experimentally verify such growth models in-situ observation of binary model systems by X-radiography has become the method of choice [1]. As the dendrite growth process is significantly influenced by solute diffusion accurate comparison with models requires concentration determination of the melt in the in-situ experiments.

Concentration measurements are common in radiography experiments that use momochromatic synchrotron X-radiation [2]. Concentrations in the melt can be calculated using the known attenuation coefficient of the material. With polychromatic X-ray sources the determination is more complicated as the attenuation of the radiation is wavelength dependent. However, polychromatic sources have some major advantages: they are more easily accessible and more flexible, thus fluidflow can be influcend by different beam orientations.

To overcome the wavelength problem we have developed a calibration method to be able to measure melt concentrations during our in-situ experiments [3]. For this purpose, we measured the intensities of samples of known composition and thickness in many independent experiments. We found an almost linear dependency of concentration with measured image intensity. Through this calibration we obtained an intensity-concentration correlation slope for an Al-24 at.% Ge alloy. Applying this value to other radiopgrahy experiments enables us to map concentrations in the melt.

An example for the concentration conversion is illustrated in Fig. 1. A radiography sequence of a solidifying Al-24 at.% Ge alloy is shown. A slow cooling rate of 1K min^{-1} was applied. The grey scale of the image in Fig. 1a) represents the intensities originally recorded by the CCD detector. The two dendrites appear brighter than the surrounding melt. They are composed mainly of aluminum which attenuates the radiation less strongly than germanium. In general it can be concluded that the brighter parts in the image are richer in aluminum. An important observation is that the melt directly surrounding the dendrites is slightly darker, i.e. germanium richer, than the melt further away from the dendrites. This is due to the germanium that gets rejected from the growing dendrites. As growth proceeds more and more germanium is rejected and diffuses into the melt. In Fig. 1b) the radiography images are converted from gray scale into false colour for better visibility. Our calibration method enable us to assign absolute concentrations to the colour scale making concentration mapping in the melt possible. Note that the images are low-pass filtered for noise reduction and that the color graduation is chosen very roughly. The time between two successive images is 25 seconds. The germanium concentration between the two dendrites increases within 75 seconds from 24 at.% Ge to >25 at.% Ge.

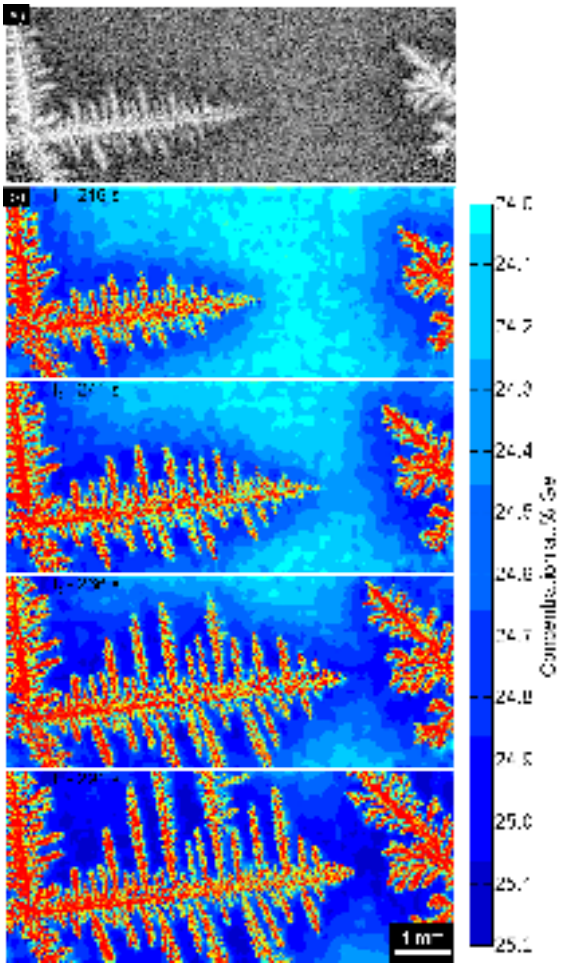

FIG. 1: a) Radiography image of a solidifying Al-24 at.% Ge sample. b) Concentration maps of a radiography sequence.

The combination of in-situ observation and concentration mapping is a valuable tool to investigate the relationship between dendrite growth and solute diffusion. Furthermore, the measurements can be used to compare with growth models predicting dendrite growth.

* Corresponding author: maike.becker@dlr.de

[1] R.H. Mathiesen, L. Arnberg, H. Nguyen-Thi and B. Billia, JOM **64**, 76-82 (2012)
[2] W.U. Mirihanage, K.V. Falch, I. Snigireva, A. Snigirev, Y.J. Li, L. Arnberg and R.H. Mathiesen, Acta Mater. **81**, 241-247 (2014)
[3] M. Becker, S. Klein and F. Kargl, Scripta Mater. **124**, 34-37 (2016).

Growth kinetics in undercooled pure Fe and dilute Fe-1 at.% B

C. Karrasch,[1,2,*] S. Burggraf,[1,2] T. Volkmann,[1] M. Kolbe,[1] and D. M. Herlach[1,2]

[1] *Institut für Materialphysik im Weltraum, Deutsches Zentrum für Luft- und Raumfahrt (DLR), 51170 Köln, Germany*
[2] *Institut für Experimentalphysik IV, Ruhr-Universität Bochum, 44780 Bochum, Germany*

Dendrite growth velocities are measured as a function of undercooling in pure Fe and dilute Fe-1 at.% B [1]. Electromagnetic levitation technique (EML) is used for containerless processing of undercooled melts under $1g$ and μg (reduced gravity in parabolic flight) conditions. The experimental results (see Fig. 1) show a transition of diffusion-limited to thermally controlled growth with the active development of solute trapping (non-equilibrium phenomenon). A sharp interface model by P. GALENKO is used to describe the experimental data taking into account a velocity dependent partition coefficient $k(V)$ [2] which is illustrated in Fig. 2. The concentration of the alloy various pattern of dendrite growth morphology were detected as spiral like (Fe-1 at.% B), zigzagging (Fe-5 at.% B), and U-turn (Fe-10 at.% B) growth. This bent dendrite growth behaviour could also been observed under reduced gravity conditions in parabolic flight.

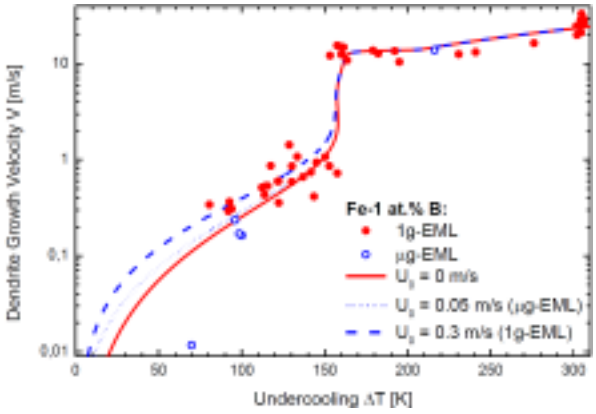

FIG. 1: The dendrite growth velocity as a function of undercooling of Fe99B1 alloy in a semilogarithmic plot measured in $1g$ (solid red circles) and reduced gravity, μg, (open blue circles). The growth velocities at small undercoolings measured in μg are smaller than those measured in $1g$. Even though not in quantitative agreement with calculations both the experiments and computations reveal qualitatively the increase of the dendrite growth kinetics if forced convection is present.

sequences of solute trapping on concentration profiles, changes of the undercooling (contributions of constitutional, thermal, curvature, and kinetic undercooling), and the variation of the dendrite tip radius with increasing undercooling were demonstrated by computations within sharp interface theory. The experiments in reduced gravity confirm previous findings that the reduction of forced convection leads to a reduction of dendrite growth kinetics. Whereas so far dendrite growth was observed to take place always in rectilinearly direction bent dendrite growth was found for differently concentrated Fe-B alloys [3]. Depending on the

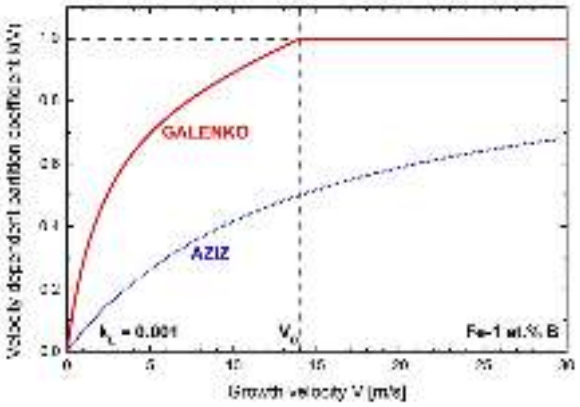

FIG. 2: The partition coefficient k(V) as a function of the growth velocity V, computed according to a model by AZIZ (blue line) and according to a model by GALENKO (red line).

The authors thank Haifeng Wang, Georg Ehlen, Stefan Burggraf, Raphael Kobold, and Jan Gegner, for stimulating discussions and Andreas Meyer for continuous support. The experiments during the parabolic flight campaign were essentially conducted with the help of the TEMPUS-Crew, David Heuskin, Stephan Schneider, and Julianna Schmitz of DLR-MUSC. The work was financially supported by the Deutsche Forschungsgemeinschaft DFG within contract HE1601/26 and ESA within contract 15236/02/NL/SH.

* Corresponding author: christian.karrasch@dlr.de

[1] C. Karrasch, T. Volkmann, M. Kolbe, D.M. Herlach, Acta Materialia (submitted 2016).
[2] P.K. Galenko, Solute trapping and diffusionless solidification in a binary system, Physical Review E 76 (2007) 031606.
[3] C. Karrasch, T. Volkmann, J. Valloton, M. Kolbe, D.M. Herlach, IOP Conference Series: Materials Science and Engineering, Volume 117, conference 1 (2015).

Crystal nucleation in an undercooled melt of glass forming NiZr

R. Kobold,* M. Kolbe, W. Hornfeck, and D. M. Herlach
Institut für Materialphysik im Weltraum, Deutsches Zentrum für Luft- und Raumfahrt (DLR), 51170 Köln, Germany

The reason that liquids can be undercooled significantly below their melting temperature has to do with the process of nucleation in the undercooled liquid. According to classical nucleation theory, a nucleus becomes a stable growing crystal if it energetically overcomes an activation barrier for nucleation. This barrier is generated by the interplay of a surface contribution ($\sim r^2$) and a volume contribution ($\sim r^3$) of the nucleus.

In general, one can distinguish between two nucleation types, the homogeneous nucleation and the heterogeneous nucleation. Homogeneous nucleation is an intrinsic process i.e. it only depends on the properties of the system and every atom in the undercooled liquid is a potential starting point for nucleation. On the contrary, heterogeneous nucleation is an extrinsic process, where only atoms are involved that are located at the interface between an impurity phase and the undercooled liquid. In order to decide, which nucleation type is present, a characteristic pre-exponential factor K_V has to be determined, which in literature is interpreted as a measure for the number of atoms $N_0 = N_A/V_m$ (N_A: Avogadro's number; $(V_{m,A} + V_{m,B})/2 = V_m$: molar volume) that can act as initial point for nucleation. Turnbull [1] proposed that this factor is in the order of $K_V \approx 10^{39}\mathrm{m}^{-3}\mathrm{s}^{-1}$ for homogeneous nucleation, provided that the attachment kinetics of atoms to the solid nucleus are collision limited. If, as mentioned above, solely atoms at an impurity phase are involved in the nucleation process, N_0 is reduced and as a consequence K_V becomes significantly smaller.

Electrostatic levitation (ESL) is applied in order to undercool a liquid spherical sample of intermetallic NiZr with a diameter of $3-4\,\mathrm{mm}$. One single, contaminant free sample is undercooled 200 consecutive times which leads to a distribution function of undercooling temperatures. Within a statistical approach of classical nucleation theory [2] the distribution (histogram) is analyzed yielding parameters e.g. the pre-exponential factor of K_V. A Poisson distribution is presumed in order to calculate a nucleation distribution function which is superimposed onto the histogram, as shown in Fig. 1. By neglecting the temperature dependence of K_V the cumulative distribution function is written as

$$F(T) = 1 - \exp\left(-\frac{VK_\mathrm{V}}{\dot{T}\frac{d\left(\frac{\Delta G^*}{k_\mathrm{B}T_\mathrm{n}}\right)}{dT}}\int_{T_\mathrm{L}}^{T}\left(\frac{CT^2}{\Delta T^2}\right)\right) \quad (1)$$

with $-\Delta G^*/k_\mathrm{B}T_\mathrm{n} = -CT^2/\Delta T^2$. Plotting $\ln(-\ln(1-F(T)))$ versus $T^2/\Delta T^2$ leads to a linear relation giving a slope -*C* and an intercept *b*. With *C* and *b*, obtained from a fit to experimental data, K_V and ΔG^* for critical nuclei formation can be determined. The resulting

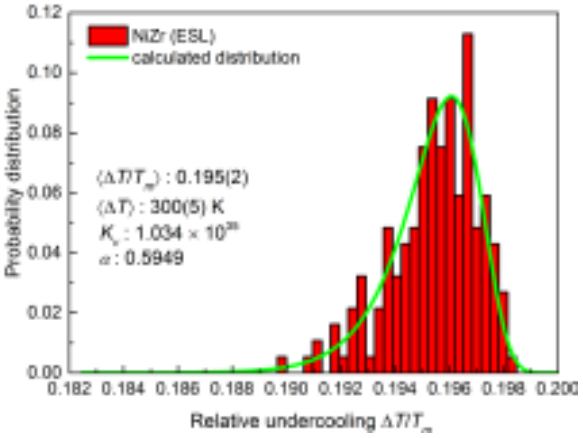

FIG. 1: Normalized frequency of nucleation events versus the relative undercoolings for 200 consecutive solidification cycles with results originating from the statistical analysis.

parameters listed in Fig. 1, which compare well to the expected values for similar metallic systems [3], indicate *homogeneous nucleation*. The pre-exponential factor $K_V \approx 10^{35}$ is distinctly closer to the value of 10^{39} discussed by Turnbull for homogeneous nucleation than to the discussed value of 10^{25} for heterogeneous nucleation. With a measurement accuracy of the pyrometer of $\pm 5\,\mathrm{K}$ at $100\,\mathrm{Hz}$ the error for K_V is negligible. Homogeneous nucleation is plausible for further reasons: 1. the large undercooling temperatures of small variation (average undercooling $\langle \Delta T \rangle = 300\,\mathrm{K}$); 2. the skew distribution of nucleation events with a steep decrease at higher relative undercoolings $\Delta T/T_m$; 3. The value of $\alpha = 0.5949$ which compares reasonably well with the one characterizing polytetrahedral (icosahedral) structures [3]. The latter point is mentioned due to the findings for NiZr described by Hornfeck et al. [4]. They propose a compressed icosahedron as primordial nucleus for the solidification of NiZr at high undercooling temperatures. The gained parameters also enabled a calculation of the solid-liquid interfacial energy $\sigma = 0.2107(6)\,\mathrm{J\,m^{-2}}$, which, for example, is important for modeling the crystal growth velocity as a function of the undercooling.

The authors thank D. Holland-Moritz for fruitful discussions and Andreas Meyer for continuous support. The work was supported by the Deutsche Forschungsgemeinschaft within contract HE1601/28.

* Corresponding author: raphael.kobold@dlr.de

[1] D. Turnbull, Contemp. Phys., **10**, 473 (1969).
[2] V.P. Skripov, Curr. Top. Mat. Sci. **2**, 327 (1977).
[3] G. W. Lee et al., Phys. Rev. B **72**, 174107 (2005).
[4] W. Hornfeck et al., arXiv:1410.2952 (2014).

Solidification velocity of undercooled FeCo alloys

C. Kreischer* and T. Volkmann
Institut für Materialphysik im Weltraum, Deutsches Zentrum für Luft- und Raumfahrt (DLR), 51170 Köln, Germany

To understand the solidification process of a metallic alloy is crucial to predict the materials properties. In the binary model system of iron and cobalt solidification can evolve via a double-step process if crystallization initializes in an sufficiently undercooled melt: The metastable δ-phase (bcc structure) can be formed prior to the stable equilibrium γ-phase (fcc structure). The relative growth velocities of the phases is a significant parameter that determines the solidification process [1].

We performed electromagnetic levitation (EML) measurements for the compositions $Fe_{70}Co_{30}$, $Fe_{60}Co_{40}$, $Fe_{50}Co_{50}$, $Fe_{45}Co_{60}$, $Fe_{40}Co_{60}$, $Fe_{35}Co_{65}$ and $Fe_{30}Co_{70}$. Samples of 6.5 mm diameter were melted, undercooled and solidified. Videos of the solidification were recorded by a high-speed camera with 75000 fps [2].

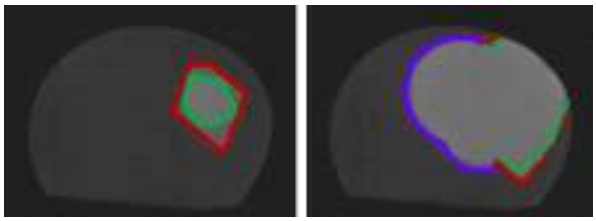

FIG. 1: Snapshots of a solidifying $Fe_{35}Co_{65}$ sample at an undercooling of 190 K. The colours indicate different growth velocities of the phases.

We analyzed three different growth velocities, namely the one of the metastable δ-phase growing into the undercooled melt, the one of the stable γ-phase growing in the mushy zone of δ-dendrites and residual melt and the one of the stable phase growing into the undercooled melt. The undercooling of the melt is the driving force for crystallization which leads to a rise in temperature (recalescence) to achieve the equilibrium state. During crystallization the melting temperature of the crystallizing phase is reached. Consequently, the temperature of the crystallizing phase is independent of the primary undercooling, e.g. the temperature in the mushy zone is always the melting temperature of δ. Due to the double step solidification of FeCo alloys we observe a double recalescence and we can even analyze the three velocities at one and the same sample as shown in FIG. 1.

In FIG. 2 the growth velocities for $Fe_{50}Co_{50}$ are displayed as a function of the undercooling with respect to the equilibrium solidus temperature. The driving forces for crystallization is the undercooling of the respective melting temperature of the phases. Therefore the red line indicates the metastable liquidus temperature. The blue symbols show the growth velocity of the γ-phase growing into the undercooled melt. The higher the undercooling, the higer the driving force and accordingly the growth velocity. At an undercooling of 0 the velocity is also 0. The red symbols represent the growth velocity of the δ-phase into the melt. Since the driving force for δ-solidification is the undercooling with respect to its own melting temperature the velocities are smaller than γ-velocities in this diagram. The green symbols display the velocities of the γ-phase in the mushy zone. Since the temperature of the mushy zone is alway the same, the driving force for crystallization of γ in this zone is always the same as well. It is independent of the primary undercooling and therefore all the data points lie on a horizontal line.

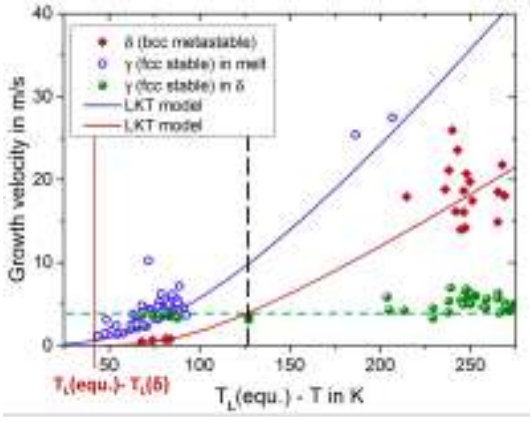

FIG. 2: Growth velocity of $Fe_{50}Co_{50}$ in dependence of undercooling with respect to the equilibrium melting temperature, measured and calculated according to LKT model [3].

The diagram can be diveded into two parts indicated by the black dashed line according to diffenrent solidification pathways of the sample. In the right section the velocity of γ in the mushy zone is slower than the one of δ. This means the sample first solidifies completely as δ and then transforms into γ. In the left section the velocity of γ in the mushy zone is faster than the one of δ. In conclusion γ overtakes δ and grows into the melt. The sample will consist of two different areas: one that was transformed from δ to γ and one that solidified direclty as γ. We presume that the different solidification pathways also influence the microstructure and lastly the properties of the material.

Financial support by the European Space Agency within the project "Magnephas" under contract no. 4200014980 is gratefully acknowledged.

* Corresponding author: carolina.kreischer@dlr.de

[1] R. Hermann, W. Löser, J. Magetism Magnetic Mater. **242-245**, 285 (2002).
[2] J. Rodriguez, C. Kreischer, T. Volkmann and D. Matson, Acta Mater. **122**, 431 (2017).
[3] J. Lipton, W. Kurz, R. Trivedi, Acta Metall. **35(4)**, 957 (1987).

Delay time of the δ-γ phase transformation during the solidification process of undercooled FeCo alloys

C. Kreischer* and T. Volkmann

Institut für Materialphysik im Weltraum, Deutsches Zentrum für Luft- und Raumfahrt (DLR), 51170 Köln, Germany

As described in the previous article the relative growth velocities of the γ- and the δ-phase control the multistep solidification process in FeCo alloys. Besides the growth velocities the delay time between the nucleation of a metastable and a stable phase is a significant parameter that determines the solidification process of many alloys. The results of delay time measurements in FeNiCr alloys, for example, are presented in [1].

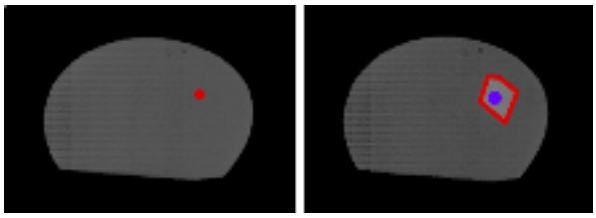

FIG. 1: Nucleation of the δ-phase (red) in the undercooled melt and subsequent nucleation of the γ-phase (purple) within the mushy zone of δ-dendrites and residual melt. The delay time is definded as the time between nucleation of the phases at the same position.

We performed measurements at the electromagnetic levitator (EML) for the compositions $Fe_{70}Co_{30}$, $Fe_{60}Co_{40}$, $Fe_{50}Co_{50}$, $Fe_{45}Co_{60}$, $Fe_{40}Co_{60}$, $Fe_{35}Co_{65}$ and $Fe_{30}Co_{70}$. Samples of 6.5 mm diameter were melted, undercooled and solidified. Videos of the solidification were recorded by a high-speed camera with 75000 fps. As described before, the undercooling of the melt is the driving force for crystallization. During crystallization the melting temperature of the crystallizing phase is reached. Different grey values in the videos correspond to different temperatures. For the analysis of the delay time the change of the grey value for a certain pixel was observed.

FIG.2 shows the delay times for different compositions in a logarithmic scale in dependence of the primary undercooling, i.e. the undercooling with respect to the melting temperature of the stable γ-phase. The delay time lies in the range of milliseconds and varies with the composition and the undercooling.

For Fe rich alloys the delay time is longer than for Co rich alloys. The reason for this is the change of the difference between the melting temperatures of the γ-phase and the δ-phase with the change of composition. For small Co contents the difference becomes small. Consequently, the driving force for γ-crystallization is also small and the stable γ-phase nucleates after a longer delay time.

Moreover, the delay time decreases with increasing primary undercooling for all compositions. We did not expect this dependency, since the stable γ-phase nucleates within the mushy zone, where the temperature is independent of the primary undercooling. During crystallization of δ-dendrites the temperature in the mushy zone is constantly the melting temperature of δ. Thus, the variation of the delay time must be controlled by an interposed factor that in turn is dependent of the primary undercooling. In contrast, the growth velocity of the stable γ-phase in the mushy zone is independent of the primary undercooling as described in the previous article.

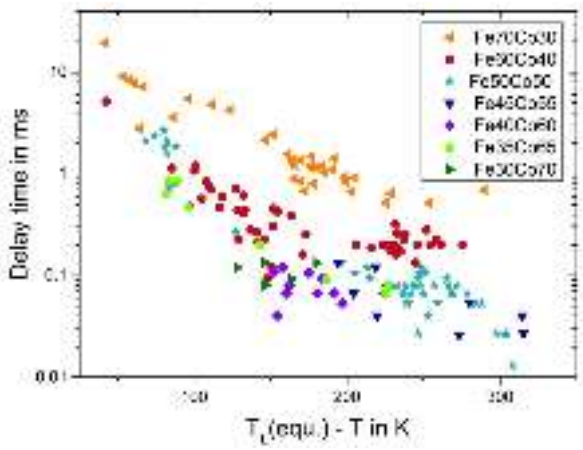

FIG. 2: Delay time (logarithmic scale) in dependence of undercooling with respect to the equilibrium liquidus.

To sum it up, the delay time as well as the growth velocities of the involved phases determine the solidification pathway of FeCo alloys. They both depend on the primary undercooling and the composition of the alloy. Whereas the growth velocity of the γ-phase in the mushy zone is independent of the primary undercooling, the delay time varies with the undercooling.

Financial support by the European Space Agency within the project "Magnephas" under contract no. 4200014980 is gratefully acknowledged.

* Corresponding author: carolina.kreischer@dlr.de

[1] D. Matson, R. Hyers, T. Volkmann, J. Jpn. Soc. Microgravity Appl. **27**, 238 (2010).

Microstructure of undercooled and solidified eutectic and hypoeutectic Ni-Sn alloys

M. Wegener,[1,*] A. Munawar,[2] and M. Kolbe[1]

[1] *Institut für Materialphysik im Weltraum, Deutsches Zentrum für Luft- und Raumfahrt (DLR), 51170 Köln, Germany*
[2] *School of Chemical and Materials Egineering, NUST, 44000 Islamabad, Pakistan*

Near-equilibrium solidification microstructures have been widely investigated, as the solidification behaviour has an important impact for the casting industry. In binary eutectics, the involved phases solidify cooperatively, which leads often to a lamellar composite microstructure. In non-equilibrium conditions, during solidification from an undercooled melt, a morphological transition from regular lamellar eutectic to anomalous eutectic has been observed in many binary eutectics [1]. A number of mechanisms has been proposed to describe the anomalous eutectic formation, which are still subjects to debate [2]. Common to all is that they relate anomalous eutectic formation to eutectic and dendritic growth, which usually have different kinetics.

Containerless, electromagnetic processing has been used to undercool and solidify the eutectic alloy $Ni_{813}Sn_{187}$.The solidification front has been observed in-situ using a high-speed videocamera in order to determine the crystal growth velocity as a function of melt undercooling. The microstructure of the solidified sample was characterized using scanning electron microscopy and electron back scatter diffraction (EBSD). The growth velocity shows a sudden increase at undercooling larger than 140 K (Fig. 1). Microstructure analyses reveal a transition from a regular eutectic to an anomalous eutectic microstructure [1].These results

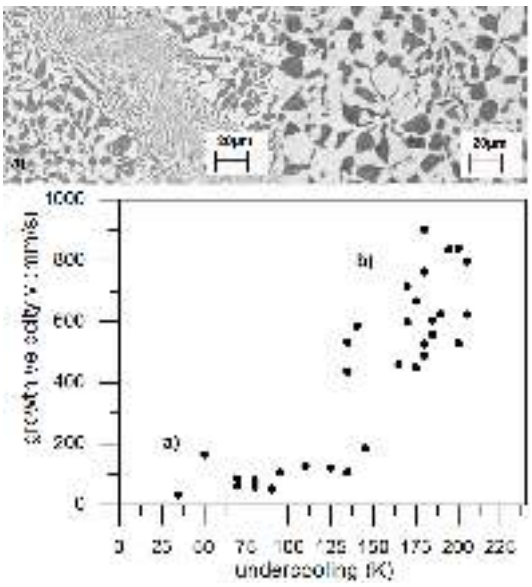

FIG. 1: Bottom: Growth velocity against undercooling for $Ni_{813}Sn_{187}$ shows a sudden increase in undercoolings lager than 140K. a) Regular eutectic matrix with islands of anomalous eutectic microstructure are observed for low undercoolings. b) With higher undercoolings the microstructure shows completly anomalous eutectic behaviour.

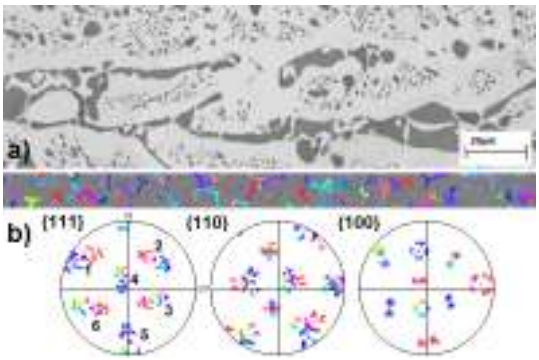

FIG. 2: a) SEM image of a hypoeutectic $Ni_{813}Sn_{187}$ sample. b) EBSD mapping of the microstructure. The measured orientations correspond to the orientation of the high temperatur Ni_3Sn phase, which metabolise during a solidstate phase transition at lower temperatures.

are in good agreement with previous data by Yang et al [3]. A dual origin for the anomalous eutectic microstructure is suggested to describe the transition in the microstructure and the growth velocity. For low undercoolings and consequently small growth velocities the growth of an eutectic dendrite is assumed, at higher undercoolings and faster growth velocities solidification and fragmentation of Ni-rich dendrites causes the anomalous eutectic microstructure.

Additionally the solidification behavior of hypoeutectic compositions, containing more tin, was investigated. Primarly dendrites of Ni_3Sn are growing, exhibit small Ni-fragments in their center. EBSD-analysis of these Ni-fragments shows that they are not randomly oriented (Fig. 2b). The inverse pole figures can be described as having few correlated single crystal orientations (1-6) with satellite structure. This presumably reflects a cooperative growth of Ni and Ni_3Sn at high temperatures, followed by fragmentation of these fine structures and precipitation of the Ni-particles in strong correlation to the Ni_3Sn high temperature phase. Ni_3Sn then transforms at lower temperature (1170 K) into a low temperature phase. Further investigations are required to fully unveil this complex solidification behaviour.

* Corresponding author: mareike.wegener@dlr.de

[1] M. Wegener, Master thesis: "Die Mikrostruktur unterkühlter und erstarrter eutektischer Ni-Sn-Legierungen", Institut für Materialphysik im Weltraum (DLR) and RWTH Aachen (2016).
[2] M. J. Li K. Nagashio K. Kuribayashi. Acta Mater 50 (2002) 3239-3250
[3] C. Yang J. Gao Y. K. Zhang M. Kolbe D.M. Herlach Acta Mater 59 (2011) 3915-3926

Dissipation by a crystallization process

Sven Dorosz,[1] Thomas Voigtmann,[2,3,*] and Tanja Schilling[1]

[1] *Physics and Materials Science Research Unit, Université du Luxembourg, L-1511 Luxembourg, Luxembourg*
[2] *Institut für Materialphysik im Weltraum, Deutsches Zentrum für Luft- und Raumfahrt (DLR), 51170 Köln, Germany*
[3] *Department of Physics, Heinrich-Heine-Universität Düsseldorf, 40225 Düsseldorf, Germany*

Crystallization from the metastable fluid is a non-equilibrium process. Standard approaches such as transition-state theory use quasi-equilibrium concepts and do not account for the fact that any irreversible process of finite duration is inevitably subject to dissipation [2]. We use Monte Carlo (MC) computer simulations to quantify this dissipation for a system of Brownian hard spheres (diameter σ, free diffusion time t_0) that crystallizes under compression at a constant rate $\dot{P}$ for a duration τ; for details see Ref. [1].

The work W performed on the system in the NPT ensemble is given by $dW = V(t)\dot{P}\,dt$, where $V(t)$ is the volume response of the system to the external driving $\dot{P}$. After subtraction of the equilibrium Gibbs free-energy difference ΔG between the initial and final state, the dissipated energy remains,

$$W_{\text{diss}} = \int_0^\tau \dot{P}V(t)\,dt - \Delta G\,. \qquad (1)$$

The volume evolution of two typical trajectories is shown in Fig. 1 (solid lines). Dashed lines indicate the well-known equations of state of the liquid and the crystal used to evaluate ΔG. The dissipated energy W_{diss} (shaded areas) is a fluctuating quantity governed by non-equilibrium fluctuation theorems [1, 2]. It consists of three contributions: (I) is the work associated with compression of the metastable liquid. (III) is a contribution from defects in the crystal. Contribution (II) yields the non-equilibrium dissipation q^c associated with the crystallization process proper.

The average response $\zeta := \langle q^c\rangle/\dot{P}$ is shown in Fig. 2. It can be interpreted as a generalized friction coefficient

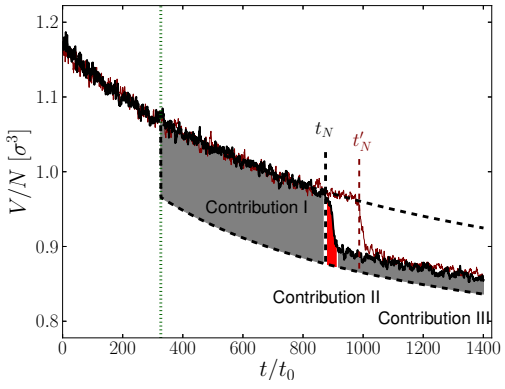

FIG. 1: Specific volume $V(t)/N$ along two typical simulation trajectories of a hard-sphere system compressed with a rate $\dot{P} = 0.01065\,k_BT/\sigma^3 t_0$ (solid lines). Induction times are labeled t_N and t'_N. A vertical line marks the coexistence point. Shaded areas indicate the different contributions to the dissipated energy, Eq. (1).

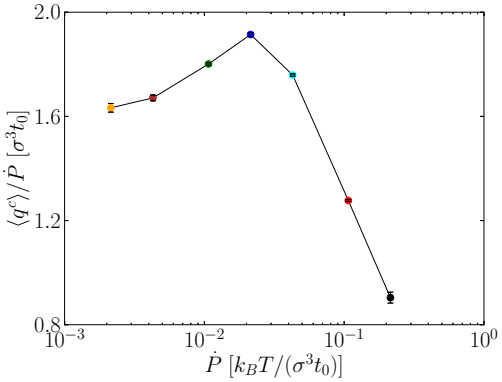

FIG. 2: Crystallization loss, i.e. the average energy per particle dissipated during crystallization relative to the external driving rate, $\zeta(\dot{P}) = \langle q^c\rangle/\dot{P}$, as a function of compression rate $\dot{P}$ (full symbols, with lines to guide the eye).

that characterizes the resistance of the melt to phase transformation. The value at $\dot{P} \to 0$ is an immanent system property, the *quasi-static crystallization loss*.

At driving forces above a threshold $\dot{P}^*$ the crystallization loss $\zeta(\dot{P})$ drops sharply with increasing $\dot{P}$. This marks the cross-over from the quasi-static to a strongly driven regime of crystallization. The effects of the external driving start to dominate the crystallization process once the compression rate is faster than the typical thermal energy density can be redistributed through collective particle rearrangements.

The strongly driven melt, $\dot{P} > \dot{P}^*$, relaxes faster into the crystal phase than in the quasi-static case. This accelerated crystallization mechanism proceeds through non-equilibrium relaxation channels, in particular the formation of meta-stable crystal structures (bcc instead of fcc). As suggested by Landau theory [3], to form the equilibrium fcc requires a larger set of reciprocal lattice vectors, i.e., a larger set of local density fluctuations to be sampled. It is plausible that this takes more time, so that bcc is favored kinetically at large driving rate. The tendency to form metastable crystal structures in rapid solidification is also well known from metallic melts [4].

* Corresponding author: thomas.voigtmann@dlr.de

[1] S. Dorosz, Th. Voigtmann, and T. Schilling, EPL **113**, 10004 (2016).
[2] D. J. Evans and G. P. Morriss, *Statistical Mechanics of Nonequilibrium Liquids* (Cambridge University Press, Cambridge, UK, 2008); U. Seifert, Rep. Prog. Phys. **75**, 126001 (2012).
[3] S. Alexander and J. McTague, Phys. Rev. Lett. **41**, 41 (1978).
[4] D. M. Herlach, Metals **4**, 196 (2014).

1.4 Granular Matter and Related

Analysis of dynamic light scattering measurements on fluidized granular media

Ph. Born,* S. Reinhold, J. Schmitz, and M. Sperl
Institut für Materialphysik im Weltraum, Deutsches Zentrum für Luft- und Raumfahrt (DLR), 51170 Köln, Germany

Advancing granular rheology and understanding the nonlinear transitions in agitated or flowing bulk granular media requires well defined dynamic states of granular media and suited characterization methods. Achieving a steady and homogeneous agitated state of granular media is hindered by the interplay of agitation, dissipation and gravitation. Dynamic homogeneity requires agitation of each individual particle or, for very low dissipation, at least randomly varying agitation. In consequence, only fluidization by the interstitial fluid like in gas- or liquid-fluidized beds has the chance to achieve a homogeneous agitated state. However, gravitation imposes consolidation stresses, and fluidized granular media form hydrodynamic unstable states which separate into regions with low and high density on ground. Fluidization of granular media in microgravity can minimize consolidation stresses and facilitate homogeneous states.

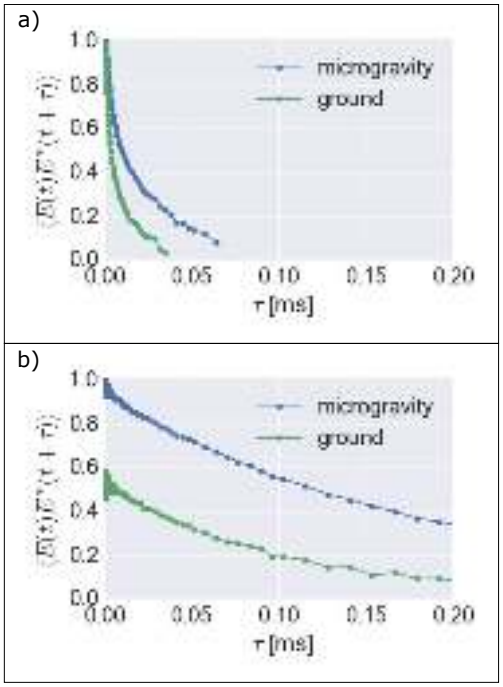

FIG. 1: Electric field correlation functions of fluidized granular media as obtained during drop tower flights and on ground. The field correlation functions are the part of the IACF which is caused by microscopic particle motions. Measurements at filling fractions of 0.48 are displayed in a). Measurements at filling fractions of 0.6799, close to the filling fraction of full arrest of 0.68, are displayed in b). Microscopic motion is always faster on ground, which can be seen from the faster decay in correlation. Average particle motion becomes slower at higher packing fraction in both cases. The intercept of the field correlation reduces at high filling fraction on ground, which indicates that some parts of the sample became so slow that on the time scales of the measurements no motion was detectable any more.

Characterization of such fluidized states is impeded by the opaque nature of granular media. Opaqueness is the result of multiple scattering of visible light within the sample and prevents imaging of particles and particle displacements within the bulk. Application of diffusing-wave spectroscopy (DWS) to fluidized granular media may deliver information on particle displacements even within the bulk as well as having moderate instrumental demands suited to microgravity experiments. DWS connects temporal intensity fluctuations of multiple scattered coherent light to displacements of microscopic scattering centers relative to each other by the intensity autocorrelation function (IACF).

Application of DWS to fluidized granular media requires to take the large particle size into account. In established dynamic light scattering theory for microscopic particles, a displacement by a particle does not change the intensity of the light scattered by this particle. In contrast, the intensity of the light scattered by an particle depends strongly on the position of the particle relative to the illuminating light beam in granular media. This mechanism turns DWS sensitive to particle number fluctuations, in addition to being sensitive to particle displacements relative to each other [1]. This effect can be used to monitor homogeneity of fluidized states of granular media.

We applied this new evaluation methodology to fluidized granular media on ground and in microgravity. Microgravity and fluidization had been achieved in drop tower flights [2]. The setup allows to perform DWS measurements on gas-fluidized media at various filling fractions of the sample cell. The DWS measurements revealed markedly different behavior of fluidized granular media close to the filling fraction of full arrest (see Fig. 1). The sample on ground takes partially stays arrested due to the gravitational consolidation pressure, while the remaining fractions take a low-density state. The sample in microgravity can still be homogeneously fluidized, which is indicated by absence of number density fluctuations and fully developed microscopic dynamics [3].

Concluding, microgravity allows the steady and homogeneous dynamic states required to apply suitable adapted diffusing wave spectroscopy.

The authors thank the team of the ZARM drop tower GmbH for valuable support during realisation of the setup and the measurement campaigns.

* Corresponding author: philip.born@dlr.de

[1] P. Born, S. Reinhold and M. Sperl, Phy. Rev. E. **94**, 032901 (2016).
[2] P. Born, J. Schmitz, M. Bußmann and M. Sperl, Microgravity Sci. Technol. **28**, 413 (2016).
[3] P. Born, J. Schmitz and M. Sperl, in preparation, (2017).

Force transmission and plastic deformation of granular columns

Ph. Born,[1,*] J. Haeberle,[1] S. Pitikaris,[1] M. Sperl,[1] and H. Chen[2]

[1]*Institut für Materialphysik im Weltraum, Deutsches Zentrum für Luft- und Raumfahrt (DLR), 51170 Köln, Germany*
[2]*Institut für Umformtechnik und Leichtbau, Technische Universität Dortmund, 44227 Dortmund, Germany*

Granular media have properties that make them distinct from classical states of matter. Granular may neither be fully solid, liquid or gaseous, but may take states akin each of these. This property leads to notorious displeasing behavior of granular media, which may segregate and demix their components during processing, or may clog pipes and silos during transport. Still, the properties of granular media also enable new applications and technologies. A recent idea is to use granular media as a shapeless solid in hot forming of hollow profiles [1]. Hot forming of hollow steel profiles is presently limited by the forming fluid. An internal fluid is required in forming of hollow profiles to provide inner pressure for shaping the blank tube into a die. This fluid has to withstand extended temperature ranges without undergoing phase transitions, which is hard to met with conventional liquids. Gases have limited use as forming fluid due to sealing problems, extended storage of work in the compressed gas and insufficient heat transport [1].

Granular media of ceramic or oxidic particles can overcome these limitations. Sealing and temperature stability are no issues, and granular media can adapt the shape of the die and thus can form the tube.

Still, granular media have inherent limitations to the use as forming media. Forces are transmitted through granular media along discrete particle contacts, which form networks of force chains (see Fig. 1). Additionally, the particles bear frictional contacts, which can take up large fractions of the applied load. Granular media can be treated as homogeneous media only on scales much larger than the particles, and exhibit a non-hydrostatic distribution of pressure within the granular medium and at container walls. Plastic deformation is inherently non-uniform and is determined by the internal friction angle and the external stress field.

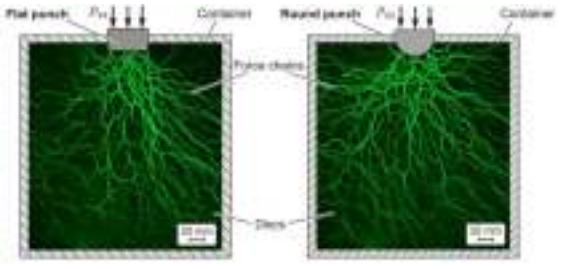

FIG. 1: Visualization of force chains in a granular medium by stress birefringence in 2D. The brightness of a particle is an indicator of the stress field inside of a disc-shaped particle. A network of discrete force chains develops upon indentation by a punch. Only a fraction of all particles is involved in the formed force network. The development of the force chain network is compared at the same displacement of two different indenters. The force chain pattern spreads more homogeneously throughout the granular medium upon indentation by a cylindrical indenter.

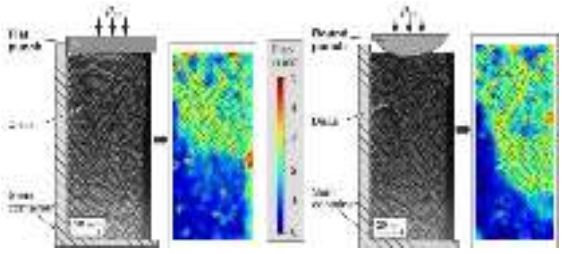

FIG. 2: Visualization of plastic deformation of a granular column in 2D. The differences in the force chain patterns also lead to different plastic deformation upon removal of one of the rigid walls. The displacement maps (right of imagages) show that particles have displaced nearly throughout the packing after moving the cylindrical indenter one disc diameter. Displacement is more localized in the case of the flat indenter.

The external stress field in forming of hollow profiles is to a large extent determined by the piston. We investigate in 2D experiments with stress-birefringent discs the development of the force chain pattern and the plastic deformation of granular columns as function of the piston shape [2]. The force chain network spreads more homogeneous through a confined granular medium under indentation by a cylindrical indenter (see Fig. 1). This indicates a homogeneous stress field in the granular medium. The plastic deformation imposed by the stress field is investigated by removing one side wall in the experiment (see Fig. 2). Plastic deformation, probed by the displacement of the particles, can be verified in larger areas of the sample under action of cylindrical piston than under action of a flat piston.

The forming ability of granular media depends on the possibility to uniformly distribute pressure inside the blank tube and to adapt to arbitrary shapes of the dies. This forming ability could be identified as function of the piston shape. Identification of this parameter helped optimization of hot forming of hollow steel profiles [2].

The authors thank the project team "Granular media-based tube press hardening" at TU Dortmund for stimulating discussions and ideas. Funding by the German Research Foundation (DFG) under grant numbers BO 4174/2-1 and SP 714/12-1 is gratefully acknowledged.

* Corresponding author: philip.born@dlr.de

[1] H. Chen, A. Güner, N. Ben Khalifa, and A. E. Tekkaya, J. Mater. Process. Technol. **228**, 145 (2016).
[2] H. Chen, S. Hess, J. Haeberle, S. Pitikaris, P. Born, A. Güner, M. Sperl, and A. E. Tekkaya, CIRP Ann. - Manuf. Technol. **65**, 273 (2016).

Aerogel-filled metals: a syntactic cellular material

S. Steinbach,[1,*] A. Dennstedt,[1] A. Orth,[2] and L. Ratke[3]

[1]*Institut für Materialphysik im Weltraum, Deutsches Zentrum für Luft- und Raumfahrt (DLR), 51170 Köln, Germany*
[2]*European Astronaut Centre, Linder Höhe, 51147 Köln, Germany*
[3]*Institut für Werkstofforschung, Deutsches Zentrum für Luft- und Raumfahrt (DLR), 51170 Köln, Germany*

Light-weight porous metals can be produced by casting liquid metal around inorganic particles or hollow spheres of low density, or by introducing such materials into a metallic melt by stirring or squeezing [1]. If the space holder is removed, an open porous sponge results. If the granules remain in the metallic product after casting a syntactic foam is achieved. The advantage of all types of metal-based syntactic materials are low density, high-specific stiffness, good potential for kinetic energy absorption after the onset of plastic deformation and high surface area. Although metallic foams are and can be perfectly used especially as cores for sandwich panels, there still is room for improvement both in processing techniques as well as properties.

In this paper a new super-light, thermally resistant filler material is presented and tested to produce light-weight aluminium alloy composites with good yield strength and energy absorption potential: the pore space between nano-structured silica-aerogel granulates is infiltrated with Al-alloy melts. Aerogels are nano-structured, open porous materials made via sol-gel processing (for details see Aegerter et al. [3]). They have a very low thermal conductivity of $0.012 \mathrm{Wm^{-1}K^{-1}}$ and consist of silica particles connected in 3D. Since these filler materials have vanishing density ($100 \mathrm{kgm^{-3}}$), they need not to be removed from the final cast product. As an aerogel material, we used Lumira^{TM} particles from Cabot.

Different methods [2] were used to prepare metal-aerogel syntactic foam composites: centrifugal casting, squeeze and suction casting. The last method gave the best results, using an $\mathrm{Al}-11\mathrm{wt.\%Si}$ melt infiltrating steel tubes of circular cross-section (inner diameter of 47 mm, wall thickness of 1.5mm and a length of 500mm) (Fig. 1) filled with aerogel granulate. The 3D structure of the Al-composite materials produced were examined [2] with an X-ray tomography system. Mechanical tests with the produced materials were performed: The composite material has a density of around 900 kg $\mathrm{m^{-3}}$, a yield stress of 8 MPa and absorbs 8 kJ $\mathrm{kg^{-1}}$ mechanical energy.

FIG. 1: Syntactic Al–Aerogel foams after dismantling of the steel tube.

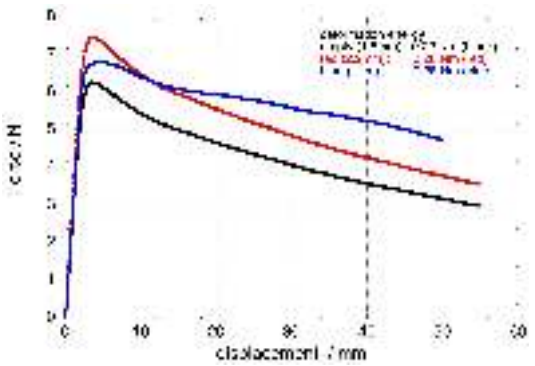

FIG. 2: Comparison of load deflection curves of two empty rectangular steel bars with different wall thicknesses (see legend) and a thin-walled bar filled with an aerogel syntactic foam. Energy absorption is shown in the legend.

Fig. 2 shows that a filled steel bar still has a higher energy absorption than an empty and also a bar with a higher wall thickness. The load-deflection curves of the empty tubes behave as expected: First, there is a linear increase in force needed to bend the bars elastically, followed by a short yielding and then the maximum in force is reached once buckling starts, which then is followed by a decrease in force needed to further bend the bar. The metal-aerogel core inside the steel tubes introduces a long period of deformation before the force decreases. The huge stress required to further deform the filled tubes after the onset of deformation is the essential advantage of the filled tubes. This difference leads to an increase in total energy absorption and is important for example in case of the crash of an A or B pillar or the stringer. We have shown that syntactic metal foams using silica aerogels as a filler in liquid metals can be produced leading to a metallic foam like structure with good mechanical properties. Further development is possible, especially using low-pressure die casting as a versatile and cheap technique. Improvement is also possible with respect to pore volume using a suitable size spectrum of aerogel particles. And of course, other aerogels aside from silica could also be used, for example carbon.

* Corresponding author: `sonja.steinbach@dlr.de`

[1] J. Banhart, Prog. Mater. Sci. **46**, 559-632 (2001).
[2] A. Orth, S. Steinbach, A. Dennstedt and L. Ratke, Mater. Sci. Technol., DOI 10.1080/02670836.2016.1195971 (2016).
[3] M. Aegerter, N. Leventis and K. M. M. eds., *Aerogels handbook* (Springer, New York, 2011).

1.5 Theory and Simulation

Sedimentation of Particles in Glass Forming Liquids

H. Cárdenas[1,*] and Th. Voigtmann[1,2]

[1] *Institut für Materialphysik im Weltraum, Deutsches Zentrum für Luft- und Raumfahrt (DLR), 51170 Köln, Germany*
[2] *Physik-Department, Heinrich-Heine-Universität Düsseldorf, Universitätsstraße 1, 40225 Düsseldorf, Germany*

The complex dynamics of glass-forming liquids at a macroscopic level is characterized by non-Newtonian effects i.e. viscoelasticity and shear thinning, that depend on slow collective microstructural relaxation processes [1]. We use a phenomenological model to discuss their rheology by incorporating the interaction between slow relaxation and flow induced rearrangements in the fluid. A Maxwell-type constitutive equation is used to define the non-Newtonian stress tensor ($\boldsymbol{\sigma}$) needed to close the Navier-Stokes equations:

$$\overset{\triangledown}{\boldsymbol{\sigma}}(t) = G_\infty \boldsymbol{D}(t) - f(\vec{r},t)\boldsymbol{\sigma}(t) \tag{1}$$

$\overset{\triangledown}{\boldsymbol{\sigma}}$ is the upper-convected time derivative to account for the change of tensorial stresses due to flow advection. $\boldsymbol{D}$ and G_∞ are the symmetric shear-rate tensor and the low-frequency Maxwell plateau modulus, respectively.

A local relaxation rate $f(\vec{x},t)$ called fluidity governs the system rheology [2]. The fluidity follows a diffusion-relaxation equation:

$$\partial_t f(\vec{r},t) = -\frac{1}{\tau_f}\left(f(\vec{r},t) - \frac{1}{\tau_M(\dot{\gamma}(t))}\right) + \frac{\xi^2}{\tau_f}\Delta f(\vec{r},t) \tag{2}$$

To capture the competition between the quiescent structural relaxation $1/\tau$ and flow-induced relaxation we set $1/\tau_M = 1/\tau + |\dot{\gamma}|/\gamma_c$, where $\dot{\gamma}$ is the local flow rate. γ_c is a model parameter that signalizes the typical strain when local structures (nearest-neighbors cages in a fluid) break [1].

Heterogeneities in the flow are accounted by using the diffusion term $\xi^2/\tau_f \Delta f(\vec{x},t)$ in Eq. 2. This controls how far fluidized regions spread along their neighbors [2]. Our model reproduces typical non-Newtonian flow effects, e.g. plug flows in channels due to yield stress, shear banding, and pronounced memory effects like residual stress.

We are interested in studying the flow dynamics in the presence of external bodies. A resolved method called Fictious Domain Method (FDM) developed by [3] is used, where forces acting on the particle are calculated, i.e. no drag models are used. This is done by coupling a Lagrangian Discrete Element Method (DEM) to track the bodies and Computational Fluid Dynamics (CFD) to solve the flow, introduced by [4].

Model parameter τ_f will tell how fast the fluidity will reach steady state and ξ how localized the fluidization is. For small ξ the fluidization will be more localized, increasing the particle velocity, and for high τ_f the particle will slow down because of slow fluidization. The influence on the fluid-velocity profile is shown in Fig. 1.

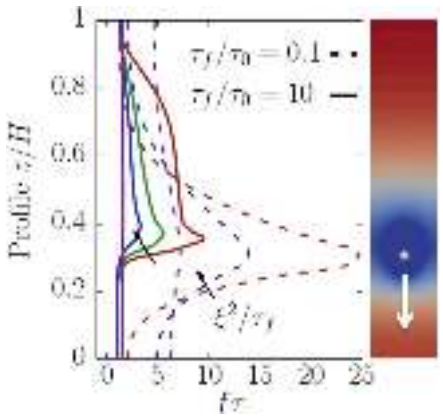

FIG. 1: Fluidity profile for different τ_f and ξ parameters.

When 2 particles sediment, initially separated by a certain vertical distance, our model can reproduce the drafting-kissing-chaining effect. The following particle is accelerated by the wake of the leading one, until they touch and form a stable pair before they reach the bottom. Fig. 2 shows how shear thinning enhances chaining formation due to the acceleration of the following particle, in comparison to a viscoelastic fluid with no shear thinning phenomenology.

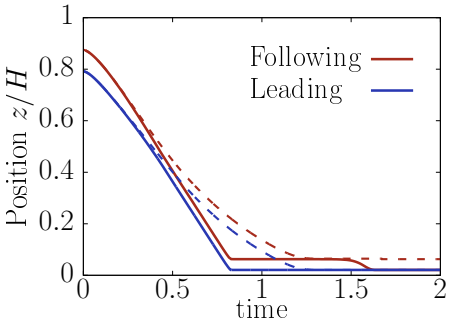

FIG. 2: Position of leading and following particle in time during sedimentation for a shear thinning fluid (solid lines) and viscoelastic (non shear thinning) fluid (dashed lines).

We use CFD-DEM-coupling and OpenFOAM to perform all mentioned calculations.

* Corresponding author: heliana.cardenas@dlr.de

[1] Th. Voigtmann. Nonlinear glassy rheology. Curr Opin Colloid Interface Sci, **19**, 549 (2014).
[2] G.Picard, A. Ajdari, L. Bocquet, F. Lequeux. Phys. Rev. E,**66**, 051501, (2002).
[3] A. Shirgaonkar, M. MacIver, N. Patankar. Journal of Computational Physics, **228** 2366 (2009).
[4] S. Pirker, A. Hager, Ch. Kloss, Ch. Goniva. Parallel open source CFD-DEM for resolved particle-fluid interaction. Ninth International Conference on CFD in the Minerals and Process Industries, October 2012.

Equilibration and Aging of Liquids of Non-Spherically Interacting Particles

Luis Fernando Elizondo-Aguilera*

Institut für Materialphysik im Weltraum, Deutsches Zentrum für Luft- und Raumfahrt (DLR), 51170 Köln, Germany

In this contribution [1], we have extended the so-called non-equilibrium self-consistent generalized Langevin equation (NE-SCGLE) theory of irreversible processes in liquids [2] in order to describe the positional and orientational thermal fluctuations of the instantaneous local concentration profile $n(\mathbf{r},,t)$ of a suddenly-quenched colloidal liquid of particles interacting through non spherically-symmetric pairwise interactions, whose mean value $\overline{n}(\mathbf{r},\Omega,t)$ is constrained to remain uniform and isotropic, $\overline{n}(\mathbf{r},\Omega,t) = \overline{n}(t)$. Such self-consistent theory is cast in terms of the time-evolution equation of the covariance $\sigma(t) = \overline{\delta n_{lm}(\mathbf{k};t)\delta n^{\dagger}_{lm}(\mathbf{k};t)}$ of the fluctuations $\delta n_{lm}(\mathbf{k};t) = n_{lm}(\mathbf{k};t) - \overline{n_{lm}}(\mathbf{k};t)$ of the spherical harmonics projections $n_{lm}(\mathbf{k};t)$ of the Fourier transform of $n(\mathbf{r},\Omega,t)$ [3]. The resulting theory describes the non-equilibrium evolution after a sudden temperature quench of both, the static structure factor projections $S_{lm}(k,t)$ and the two-time correlation function $F_{lm}(k,\tau;t) \equiv \overline{\delta n_{lm}(\mathbf{k},t)\delta n_{lm}(\mathbf{k},t+\tau)}$, where τ is the correlation *delay* time and t is the *evolution* or *waiting* time after the quench.

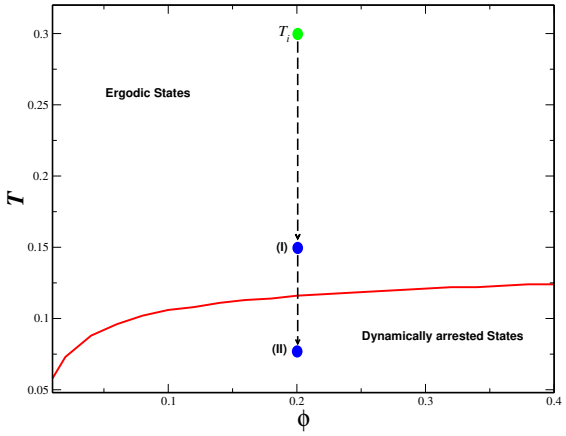

FIG. 1: Dynamical arrest line (solid curve) in the (ϕ, T) state space of the system of interacting dipoles with fixed positions. This line is the boundary between the region of ergodic states, at which the system is predicted to reach thermodynamic equilibrium, and the predicted region of dynamically arrested states. Each of the two superimposed vertical dashed arrows represent the quench of the system from an initial temperature T_i (green dot) to a final temperature T_f (blue dots), in one case above (**I**) and in the other case below (**II**) the dynamic arrest line.

As a concrete and illustrative application of this theory we have used the resulting self-consistent equations to describe the irreversible processes of equilibration or aging of the orientational degrees of freedom of a system of strongly interacting classical dipoles with quenched positional disorder. For this, we have introduced a simplified model of such interacting dipoles which starts from a dipolar fluid, where the consitutent

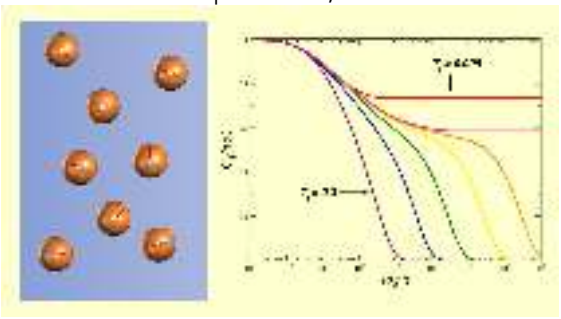

FIG. 2: Snapshots of the orientational autocorrelation function, $C_1(\tau;t) \equiv \frac{1}{3}\lim_{k\to 0}\sum_{m=-1}^{1} F^S_{1m}(k,\tau;t)$, as a function of correlation time τ , corresponding to an isochoric ($\phi = 0.2$) quench, from $T_i = 0.3$ to $T =_f= 0.095$ as a sequence of waiting times t

particles are artifially quenched in positions, and thus, fixed and randomly distributed in space. Then, we apply the NESCGLE equations to investigate the slow orientational dynamics as well as the aging and equilibration processes of the system near its "spin glass"-like transitions after a sudden temperature quench.

As a consequence of our analysis we can determine the regions in the state space of the system (spanned by the control parameters (ϕ, T), where ϕ denotes the volume fraction and T^* the temperature, see Fig. 1) where it is predicted to reach thermodynamic equilibrium (ergodic state) and those regions where conditions of dynamical arrest prevent the system to reach equilibrium (non-ergodic state).

L.F.E.A. acknowledge funding from the German Academic Exchange Service (DAAD) through the DLR-DAAD programme under grant No. 212 and to Thomas Voigtmann for useful discussions and critical comments.

* Corresponding author: `luis.elizondo@dlr.de`

[1] E. C. Cortés Morales, L.F. Elizondo-Aguilera and M. Medina Noyola, J. Phys.Chem. B 2016, **120**, 7975-7987.

[2] L. E. Sánchez-Díaz, P. E. Ramírez-González and M. Medina-Noyola, Phys. Rev. E **87**, 052306 (2013).

[3] L.F. Elizondo-Aguilera, P. F. Zubieta-Rico, H. Ruíz Estrada, and O. Alarcón-Waess, Phys. Rev. E, **90**, 052301 (2014).

Glass-Transition Asymptotics in SCGLE and MCT

Luis Fernando Elizondo-Aguilera* and Thomas Voigtmann

Institut für Materialphysik im Weltraum, Deutsches Zentrum für Luft- und Raumfahrt (DLR), 51170 Köln, Germany

In this contribution [1], we discuss a set of general features of the glass-transition scenario as predicted by two independent first principles approaches, namely, the mode coupling theory (MCT) [2] and the self-consistent generalized Langevin equation (SCGLE) theory of dynamical arrest [3]. By writing the latter in an adequate form, we show that it can be referred to as a class of MCT. Since both formalisms lead essentially to the same time evolution equations for the density correlation functions, $F(q,t)$ and $F_S(q,t)$, and only differ at the level of their independent approximations for the so-called memory kernels, a series of important features for the long time asymptotic solutions, originally developed in the context of MCT, emerge for the SCGLE approach, which allow us to investigate the source of the main differences and affnities between both approaches and regarding their predictions to particular systems.

Although this is a theoretically oriented work, we illustrate the relevance in our derivations by consider the concrete application of both approaches to describe the glass transition asymptotics of two representative model systems, namely, a hard-spheres (HS) fluid and the so-called generalized Gaussian core model. We discuss the resulting differences in terms of the q-vector dependence of asymptotic long time properties such as the self and collective ergodicity parameters, $f_S(q) \lim_{t\to\infty} F_S(q,t)$ and $f^c(q) = \lim_{t\to\infty} F(q,t)$, or the critical amplitudes $h(q)$ and $h_S(q)$.

L.F.E.A. acknowledge funding from the German Academic Exchange Service (DAAD) through the DLR-DAAD programme under grant No. 212.

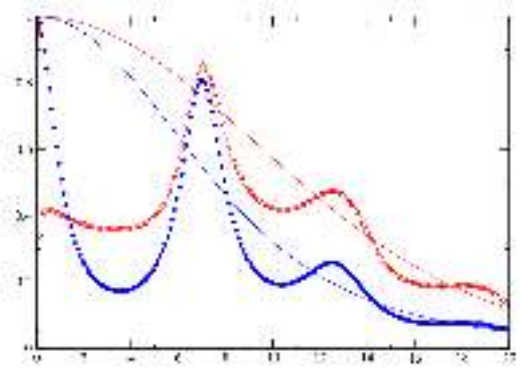

FIG. 1: Nonergodicity parameters, $f_s(q)$ (lines) and $f^c(q)$ (symbols) of the HS fluid as predicted by MCT and SCGLE theories at their respective critical points: Collective both oscillate in phase with static structure factor. The difference at $k \to 0$ between MCT and SCGLE is clearly visible and the major qualitative difference between the results. In general, SCGLE predicts slightly larger localization length than MCT (curves are narrower in q-space).

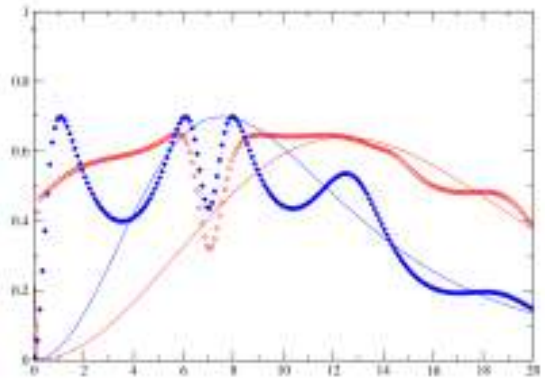

FIG. 2: Critical amplitudes $h(q)$ (symbols) and $h^s(q)$ lines for the hard-sphere system with PY structure factor, for MCT (red) and SCGLE (blue) at their respective critical points. Again, SCGLE result decays faster at large k. Both amplitudes have a "dip" around $q_{\max}$, i.e., where $f^c(q)$ is maximum: when the plateau is high, the next-order asymptote needs to have a smaller amplitude because the correlation function is bounded. SCGLE amplitude $h(k)$ has interesting peak at low k.

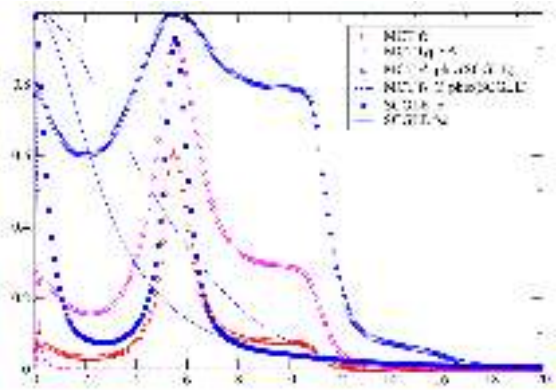

FIG. 3: $f^c(q)$ and $f^{s,c}(q)$ for the generalized Gaussian core model GCM4. Open symbols: MCT results for $f^c(q)$; dashed lines: MCT $f^s(q)$. Filled symbols, solid lines: SCGLE.

* Corresponding author: luis.elizondo@dlr.de

[1] L.F. Elizondo-Aguilera and Th. Voigtmann, to be submitted.

[2] W. Götze an Th. Voigtmann, Phys. Rev. E, **67**, 021502 (2003).

[3] R. Juárez-Maldonado and M. Medina-Noyola, Phys. Rev. E **77**, 051503 (2008).

General overview of glassy dynamics and arrested states in binary mixtures of hard-spheres: dynamical decoupling, mixed states and bifurcation

Luis Fernando Elizondo-Aguilera*

Institut für Materialphysik im Weltraum, Deutsches Zentrum für Luft- und Raumfahrt (DLR), 51170 Köln, Germany

Asymmetric binary mixtures of colloidal hard spheres are an important class of model systems able to display a rich variety of arrested states, ranging from repulsive glasses, gels, mixed states and attractive glasses which are far from being completely understood. In a series of two contributions to be reported soon, [1, 2], combining molecular dynamics simulations, theoretical calculations and available experimental data, we provide a general overview of the various arrested states occurring in a largely-asymmetric binary mixture of hard-spheres. We discuss the fundamental relevance of determining the dynamics of both species in the description of the whole dynamical arrest scenario. Our findings are consistent with the predicted existence [3–5] of three different transition lines that converge at a higher-order singularity in the parameters space of the mixture (see Fig. 1). These three lines separate the fluid (ergodic) region from the two predicted distinct types of glassy states. As the system is driven towards each of the two transition lines bordering the ergodic region, the density correlations of each species exhibit distinguishable decay patterns and different dynamical decoupling effects (see Figs. 2 and 3).

L.F.E.A. acknowledge funding from the German Academic Exchange Service (DAAD) through the DLR-DAAD programme under grant No. 212 and to Thomas Voigtmann for useful discussions and critical comments.

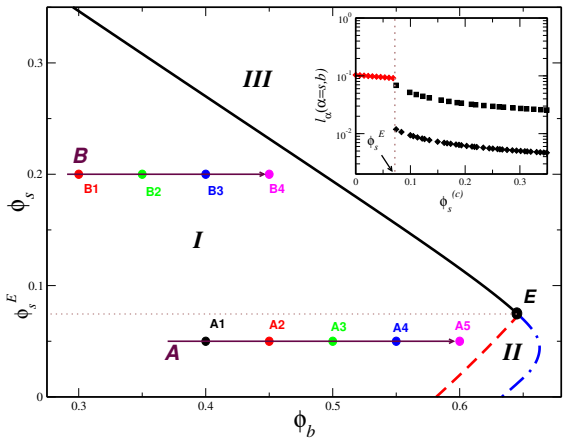

FIG. 1: Dynamical arrest diagram (solid, dashed and dashed-dot lines) for the binary mixture of hard-spheres with aspect ratio $\delta \equiv \sigma_S/\sigma_B = 0.2$ predicted by the SCGLE theory. Paths A and B describe the points of the parameters space also studied by means of MD simulations. Regions I, II and III denote the ergodic, mixed and fully arrested states, respectively. Inset: localization lengths, $l_\alpha, (\alpha = b, s)$, of the two species along the (black) solid line and the dashed line

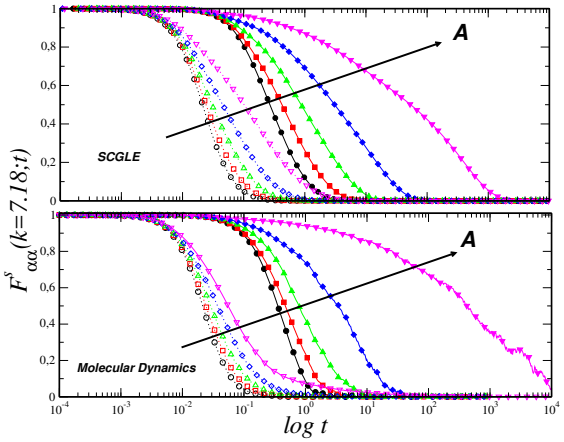

FIG. 2: Self ISFs for the binary mixture along path *A* in Fig. 1. The upper panel display the predictions from the SCGLE theory whereas the lower panel contains the corresponding results from molecular dynamics.

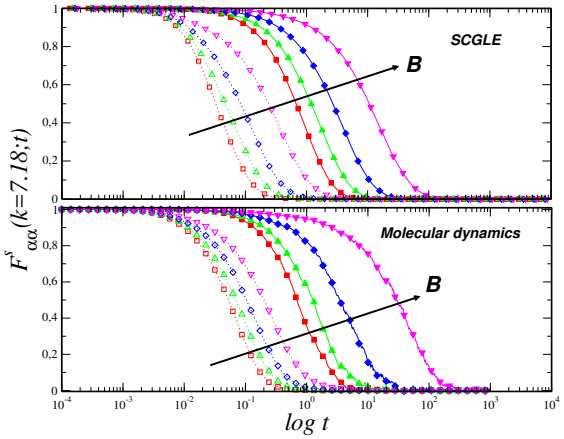

FIG. 3: Self ISFs for the binary mixture along path *B* in Fig. 1.. The upper panel display the predictions from the SCGLE theory whereas the lower panel contains the corresponding results from molecular dynamics.

* Corresponding author: `luis.elizondo@dlr.de`

[1] L. F. Elizondo-Aguilera, *et.al.* to be submitted
[2] L. F. Elizondo-Aguilera, *et.al.* to be submitted
[3] R. Juárez-Maldonado and M. Medina-Noyola, Phys. Rev. E **77**, 051503 (2008).
[4] W. Götze an Th. Voigtmann, Phys. Rev. E, **67**, 021502 (2003).
[5] Th. Voigtmann, EuroPhys. Lett. **96** (2011) 36006

Active Microrheology of Dense Microswimmer Suspensions

Alexander Liluashvili* and Thomas Voigtmann

Institut für Materialphysik im Weltraum, Deutsches Zentrum für Luft- und Raumfahrt (DLR), 51170 Köln, Germany

The dynamics of self-propelled particles in dense environments and the collective behavior of suspensions of such microswimmers is studied. Systems of artificial microswimmers are ideally suited to address the high-density dynamics of active particles. In recent years, a number of experimental model systems have emerged, such as half-capped Janus Particles whose surface-mediated energy conversion provides a mechanism of directed motion superimposed on rotational diffusion. To a large extent, the dynamics of these microswimmers is captured by relatively simple computer-simulation models. They have become a prime model setup to study the statistical physics of systems whose dynamics is intrinsically out-of-equilibrium and in violation of the usual fluctuation-dissipation-theorem (FDT) relations. In this project we provide a theory using the mode-coupling theory of the glass transition (MCT) [**?**] in the integration-through-transients (ITT) framework to describe these microswimmers mathematically.

We consider a system of hard disks in 2 dimensions having a self-propulsion velocity in the direction of their own orientation. The dynamics is fully determined by the coupled overdamped Langevin equation for the position vector of each particle $\boldsymbol{x}_i$, and the orientation ϕ_i.

$$d\boldsymbol{x}_i = D_t \boldsymbol{F}_i dt + v_0 \boldsymbol{o}_i dt + \sqrt{2D_t} d\boldsymbol{W}_i^x,$$
$$d\phi_i = \sqrt{2D_r} dW_i^\phi,$$
D_t, D_r Diffusion constants $\boldsymbol{o}_i = \left(\cos(\phi_i), \sin(\phi_i)\right)$,
$\boldsymbol{F}_i = -\boldsymbol{\partial}_i U(\{\boldsymbol{x}_1, \cdots, \boldsymbol{x}_N\})$ v_0 self-propulsion.

After transforming the coupled stochastic differential equation to a Focker-Plank equation and using the adjoint Smoluchowski operator, we can write down the time dependent density correlator.

$$\boldsymbol{S}_{l,l'}(\boldsymbol{q}, t) = \frac{1}{N} \left\langle \rho_l(\boldsymbol{q})^* \, e^{\Omega^\dagger t} \rho_{l'}(\boldsymbol{q}) \right\rangle.$$

Following the steps similar to the paper [**?**] we derive the final equation of motion for the density correlator. We remove the wave-number dependence for better readability.

$$\partial_t \boldsymbol{S}(t) = -\hat{\boldsymbol{\omega}} \boldsymbol{S}^{-1} \boldsymbol{S}(t) - \int_0^t dt' \boldsymbol{m}^{\mathsf{T}}(t - t') \, \hat{\boldsymbol{\omega}}_{\mathsf{T}}^{-1} \left[\partial_{t'} \boldsymbol{S}(t') + \hat{\boldsymbol{\omega}}_{\mathsf{R}} \boldsymbol{S}(t')\right], \quad (1)$$

with the frequency function $\hat{\boldsymbol{\omega}}$ splitted in its translational and rotational parts. After the Mode Coupling (**MCT**) approximation the memory function can be determined, which is bilinear in the density correlator.

$$\boldsymbol{m}^{\mathsf{T}}(t) \overset{\mathsf{MCT}}{\sim} \boldsymbol{S}(t)\boldsymbol{S}(t).$$

Equation (1) is the starting point of our numerical calculations. The numerical calculations with the required precision for accurate results are very demanding and high performance computers are needed. The calculations were done mainly on the Supercomputer in Jülich. The most important quantity in our theory is the dynamical density correlator matrix $\boldsymbol{S}$, which contains information about translational properties of the particles as well as the rotational properties.

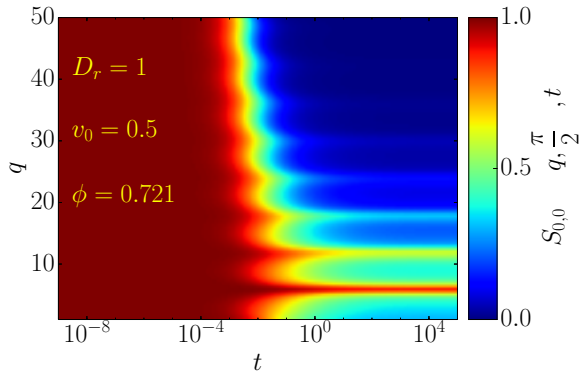

FIG. 1: Dynamical density correlator for the full theory.

In Figure (1) a typical picture of $S_{0,0}$ in a glassy state is plotted. Increasing the self-propulsion velocity v_0 to a value above some critical velocity v_c, would melt the glass and after some relaxation time τ the correlator would decay to zero. Further we want to show the influence of the rotational diffusion D_r on the relaxation time τ which is plotted in the Figure (2).

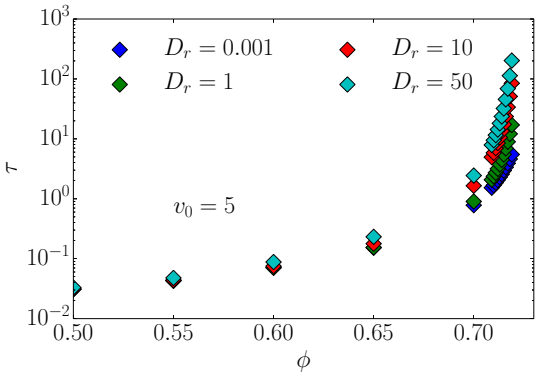

FIG. 2: Relaxation time τ as a function of density ϕ.

* Corresponding author: `alexander.liluashvili@dlr.de`

Dense Microswimmer Systems in Model Porous Media

J. Ónody[1,*] and Th. Voigtmann[1,2]

[1] *Institut für Materialphysik im Weltraum, Deutsches Zentrum für Luft- und Raumfahrt (DLR), 51170 Köln, Germany*
[2] *Fachgruppe Physik, Heinrich-Heine Universität Düsseldorf, 40225 Düsseldorf, Germany*

We model *microswimmers* by hard disk in two dimensions with a rotational degree of freedom. In addition the disks undergo a self-propulsion motion due to a constant velocity in the direction of orientation (*cf.* [1]). The microswimmers evolve in a *porous medium*, which is modeled by obstacles that are given by a frozen configuration of immobile hard disks. The schematic setting can be seen in figure 1 and was discussed for passive particles in [2].

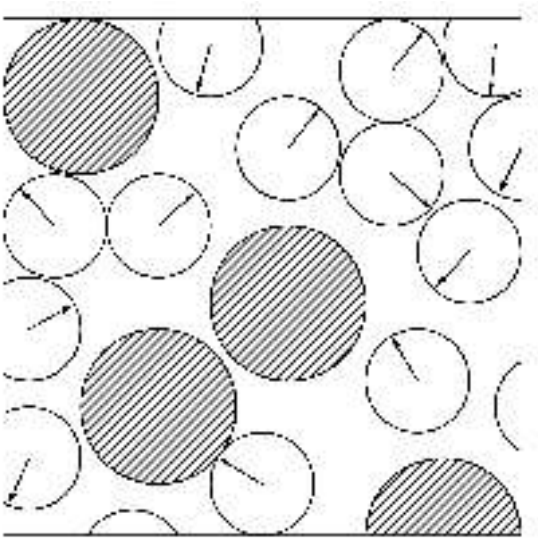

FIG. 1: Microswimmers modeled by hard disks with orientations and active motion, embedded in a porous background given by a frozen obstacle configuration.

The *density correlator* of the system at time t is defined as:

$$S_{\vec{q},l,l'} = \overline{\left\langle \rho^*_{\vec{q},l}\rho_{\vec{q},l'}(t)\right\rangle}. \tag{1}$$

Here, $\rho_{\vec{q},l}(t) = \sum_{j=1}^{N} e^{i\vec{q}\cdot\vec{r}_j(t)+il\theta_j(t)}$, is the Fourier-transformed microscopic density of the N microswimmers with momentum $\vec{q}$ and angular momentum l at time t. In analogy we define a density for the M obstacles: $\rho^{\text{obs.}}_{\vec{q}} = \sum_{j=1}^{M} e^{i\vec{q}\cdot\vec{x}_j}$. Due to the inhomogeneity of the system, we need to average twice. The *braket*-average corresponds to the random motion of the microswimmers in a given obstacle configuration and in addition we have to average over all possible, randomly distributed obstacle configurations (*bar*-average). Since, $\langle\rho\rangle \neq 0$, due the obstacles, we obtain the splitting ($\rho = \langle\rho\rangle + \delta\rho$):

$$\begin{aligned} S_{\vec{q},l,l'} &= S^{\text{con.}}_{\vec{q},l,l'} + S^{\text{blc.}}_{\vec{q},l,l'} \\ &= \overline{\left\langle \delta\rho^*_{\vec{q},l}\delta\rho_{\vec{q},l'}(t)\right\rangle} + \overline{\left\langle \rho^*_{\vec{q},l}\right\rangle\langle\rho_{\vec{q},l'}\rangle}. \end{aligned} \tag{2}$$

The first term of the density correlator, which we are mainly interested in, can be interpreted as the part of the microswimmers that is able to propagate through connected paths in the porous medium. Its evolution can be found, after applying the *Mori-Zwanzig projection-operator formalism* and the *Mode-Coupling-theory approximations* [3], to be (written in matrix notation, c ≡ connected)

$$\begin{aligned} \partial_t \mathbf{S}^{\text{c}}_{\vec{q}}(t) = &-\mathbf{S}^{\text{c}}_{\vec{q}}(t)\left(\mathbf{S}^{\text{c}}_{\vec{q}}\right)^{-1}\boldsymbol{\omega}^{\text{c}}_{\vec{q}} \\ &- \int_0^t dt'\ \left(\partial_{t'}\mathbf{S}^{\text{c}}_{\vec{q}}(t')\right)\left(\boldsymbol{\omega}^{\text{c}}_{\vec{q}}\right)^{-1}\mathbf{m}^{\text{c}}_{\vec{q}}(t-t'), \end{aligned} \tag{3}$$

with the frequency $\boldsymbol{\omega}^{\text{c}}_{\vec{q}}$ arising, because we are working in the *Smoluchowski picture*. The *memory kernel* is given by:

$$\begin{aligned} m^{\text{c}}_{\vec{q},l,l'}(t) = \sum_{\vec{k}+\vec{p}=\vec{q},l_1,l_2} &\mathcal{V}^{\text{c, hom.}}_{\vec{k},l_1,l_2} S^{\text{c}}_{\vec{k},l_1,l_2}(t) S^{\text{c}}_{\vec{p},l-l_1,l'-l_2}(t) \\ &+ \mathcal{V}^{\text{c, por.}}_{\vec{k},l_1,l_2} S^{\text{c}}_{\vec{k},l_1,l_2}(t) S^{\text{b}}_{\vec{p},l-l_1,l'-l_2}. \end{aligned} \tag{4}$$

The quadratic term in the density correlator is present in the homogeneous setting already, but as an import result one obtains a linear term, additionally. The vertices are not given explicitly here.

We will use the theory to explore the interplay of active swimming, dynamical arrest due to nearest-neighbor caging (the glass transition), and particle localization due to the heterogeneous medium (localization transition).

* Corresponding author: `jonathan.onody@dlr.de`

[1] R. Schilling and T. Scheidsteger, Phys. Rev. E **56**, 2932 (1997).
[2] V. Krakoviack, Phys. Rev. E **75**, 031503 (2007).
[3] W. Götze, *Complex Dynamics of Glass-Forming Liquids - A Mode-Coupling Theory* (Oxford University Press, New York, 2009).

2 Publications and Patents

2.1 Peer-Reviewed Publications

[1] A. Atashpendar, T. Schilling, and T. Voigtmann, *Sequencing chess*, EPL **116**, 10009 (2016).

[2] M. Becker, S. Klein, and F. Kargl, *In-situ solute measurements with a laboratory polychromatic microfocus X-ray source during equiaxed solidification of an Al-Ge alloy*, Scripta Materialia **124**, 34 (2016).

[3] P. Born, M. Bussmann, J. Schmitz, and M. Sperl, *Drop tower setup for dynamic light scattering in dense gas-fluidized granular media*, Microgravity Science and Technology **28**, 413 (2016).

[4] P. Born, S. Reinhold, and M. Sperl, *Probing density fluctuations in fluidized granular media with diffusing wave spectroscopy*, Physical Review E **94**, 032901 (2016).

[5] J. Brillo and G. Kolland, *Surface tension of liquid Al–Au binary alloys*, Journal of Materials Science (2016), DOI:10.1007/s10853-016-9794-x.

[6] H. Chen, S. Hess, J. Haeberle, S. Pitikaris, P. Born, A. Güner, M. Sperl, and A. E. Tekkaya, *Enhanced granular medium-based tube and hollow profile press hardening*, CIRP Annals – Manufacturing Technology **65**, 273 (2016).

[7] A. Choudhury, Y. C. Yabansu, S. R. Kalidindi, and A. Dennstedt, *Quantification and classification of microstructures in ternary eutectic alloys using 2-point spatial correlations and principal component analyses*, Acta Materialia **110**, 131 (2016).

[8] A. Dennstedt, A. Choudhury, L. Ratke, and B. Nestler, *Microstructures in a ternary eutectic alloy: devising metrics based on neighbourhood relationships*, IOP Conference Series: Materials Science and Engineering **117**, 012025 (2016).

[9] S. Dorosz, T. Voigtmann, and T. Schilling, *Dissipation by a crystallization process*, Europhysics Letters **113**, 10004 (2016).

[10] M. Engelhardt, A. Meyer, F. Yang, G. Simeoni, and F. Kargl, *Self and Chemical Diffusion in Liquid Al-Ag*, Defect and Diffusion Forum **367**, 157 (2016).

[11] Z. Evenson, F. Yang, G. Simeoni, and A. Meyer, *Self-diffusion and microscopic dynamics in a gold-silicon liquid investigated with quasielastic neutron scattering*, Applied Physics Letters **108**, 121902 (2016).

[12] P. Heintzmann, F. Yang, S. Schneider, G. Lohöfer, and A. Meyer, *Viscosity measurements of metallic melts using the oscillating drop technique*, Applied Physics Letters **108**, 241908 (2016).

[13] D. Herlach, T. Palberg, I. Klassen, S. Klein, and R. Kobold, *Overview: Experimental studies of crystal nucleation: Metals and colloids*, Journal of Chemical Physics **145**, 211703 (2016).

[14] J. Hötzer, P. Steinmetz, M. Jainta, S. Schulz, M. Kellner, B. Nestler, A. Genau, A. Dennstedt, M. Bauer, H. Köstler, and U. Rüde, *Phase-field simulations of spiral growth during directional ternary eutectic solidification*, Acta Materialia **106**, 249 (2016).

[15] G. Lohöfer, *Heat balance in levitation melting – Sample cooling by forced gas convection in Argon*, High Temperatures – High Pressures **45**, 255 (2016).

[16] G. Lohöfer, *On the relation between Nusselt and Péclet number in high Péclet number convective heat transfer*, International Journal of Thermal Sciences **109**, 201 (2016).

[17] Y. Luo, B. Damaschke, S. Schneider, G. Lohöfer, N. Abrosimov, M. Czupalla, and K. Samwer, *Contactless processing of SiGe-melts in EML under reduced gravity*, npj Microgravity **2**, 1 (2016).

[18] H. Mizuno, K. Saitoh, and L. Silbert, *Elastic moduli and vibrational modes in jammed particulate packings*, Physical Review E **93**, 062905 (2016).

[19] H. Mizuno, L. Silbert, and M. Sperl, *Spatial Distributions of Local Elastic Moduli Near the Jamming Transition*, Physical Review Letters **116**, 068302 (2016).

[20] H. Mizuno, L. Silbert, M. Sperl, S. Mossa, and J.-L. Barrat, *Cut-off nonlinearities in the low-temperature vibrations of glasses and crystals*, Physical Review E **93**, 043314 (2016).

[21] A. Orth, S. Steinbach, A. Dennstedt, and L. Ratke, *Aerogel-filled metals: a syntactic cellular material*, Materials Science and Technology (2016), DOI:10.1080/02670836.2016.1195971.

[22] T. Palberg, P. Wette, and D. Herlach, *Equilibrium fluid-crystal interfacial free energy of bcc-crystallizing aqueus suspensions of polydisperse charged spheres*, Physical Review E **93**, 022601 (2016).

[23] H. L. Peng, H. R. Schober, and T. Voigtmann, *Velocity autocorrelation function in supercooled liquids: Long-time tails and anomalous shear-wave propagation*, Physical Review E **94**, 060601(R) (2016).

[24] H. L. Peng and T. Voigtmann, *Decoupled length scales for diffusivity and viscosity in glass-forming liquids*, Physical Review E **94**, 042612 (2016).

[25] Y. Plevachuk, V. Sklyarchuk, I. Shtablavyi, S. Mudry, J. Brillo, H. Kobatake, A. Yakymovych, S. Fürtauer, B. Skolyszewska-Kühberger, K. W. Richter, H. Flandorfer, and H. Ipser, *Liquid Co–Sn alloys at high temperatures: structure and physical properties*, Physics and Chemistry of Liquids **54**, 440 (2016).

[26] K. Saitoh and H. Mizuno, *Anomalous energy cascades in dense granular materials yielding under simple shear deformations*, Soft Matter **12**, 1360 (2016).

[27] H. R. Schober and H. Peng, *Heterogeneous diffusion, viscosity, and the Stokes-Einstein relation in binary liquids*, Physical Review E **93**, 052607 (2016).

[28] T. Sentjabrskaja, E. Zaccarelli, C. D. Michele, F. Sciortino, P. Tartaglia, T. Voigtmann, S. U. Egelhaaf, and M. Laurati, *Anomalous dynamics of intruders in a crowded environment of mobile obstacles*, Nature Communications **7**, 11133 (2016).

[29] E. Sondermann, F. Kargl, and A. Meyer, *Influence of cross correlations on interdiffusion in Al-rich Al-Ni melts*, Physical Review B **93**, 184201 (2016).

[30] S. Steinbach, L. Ratke, G. Zimmermann, and O. Budenkova, *Formation of intermetallic phases in AlSi7Fe1 alloy processed under microgravity and forced fluid flow conditions and their influence on the permeability*, IOP

Conference Series: Materials Science and Engineering **117**, 012019 (2016).

[31] P. Steinmetz, J. Hötzer, M. Kellner, A. Dennstedt, and B. Nestler, *Large-scale phase-field simulations of ternary eutectic microstructure evolution*, Computational Materials Science **117**, 205 (2016).

[32] P. Steinmetz, M. Kellner, J. Hötzer, A. Dennstedt, and B. Nestler, *Phase-field study of the pattern formation in Al-Ag-Cu under the influence of the melt concentration*, Computational Materials Science **121**, 6 (2016).

[33] M. Stolpe, I. Jonas, S. Wei, W. Hambree, Z. Evenson, F. Yang, A. Meyer, and R. Busch, *Structural changes during a liquid-liquid transition in the deeply undercooled $Zr_{58.5}Cu_{15.6}Ni_{12.8}Al_{10.3}Nb_{2.8}$ bulk metallic glass forming melt*, Physical Review B **93**, 014201 (2016).

[34] T. Wang and M. Sperl, *Thinning and thickening in active microrheology*, Physical Review E **93**, 022606 (2016).

[35] J. J. Wessing and J. Brillo, *Density, Molar Volume, and Surface Tension of liquid Al-Ti*, Metallurgical and Materials Transactions A (2016), DOI:10.1007/s11661-016-3886-8.

[36] A. Yazdi and M. Sperl, *Glassy Dynamics of Brownian Particles with Velocity-Dependent Friction*, Physical Review E **94**, 032602 (2016).

2.2 Books and Book Chapters

[1] J. Brillo, *Thermophysical Properties of Multicomponent Liquid Alloys* (de Gruyter Oldenbourg, Berlin, Germany, 2016).

3 Presentations

3.1 Institute Seminar

Speakers that have contributed to the institute's seminar in 2016.

Prof. Dr. Thomas Rainer Heimburg, Niels Bohr Institute, Copenhagen, Denmark (Jan 12, 2016): Physics of Nerves

Prof. Dr. Bernadett Weinzierl, DLR-PA (Jan 28, 2016): Long-range transport of aerosols: new insight from airbone measurements and model simulations

Sylvia McLain, University of Oxford, UK (Feb 16, 2016): How drugs enter the brain: atomic scale insight into how drugs cross the blood brain barrier

Dr. Shaun McFadden, University of Ulster (Mar 1, 2016): Macro-to-Meso: Modeling of Alloy Solidification and the Role of Crystal Grows Kinetics

Dr. Nils Warnken, University of Birmingham (Mar 3, 2016): Studies on aspects of the solidification path of single crystal superalloys 12.04.16

Dr. Eric Josef Ribeiro Parteli, Universität zu Köln (Apr 12, 2016): Modeling sand dunes

Dr. Denis Gratias, IRCP Chimie-Paris Tech, Paris, France (Apr 19, 2016): Defects in alloys with structures based on Z-modules: from twins to metadislocations

Prof. Dr. Berenike Maier, University of Cologne, Germany (Apr 26, 2016): Genetic control of bacterial mechanics

Prof. Dr. Heinz-Wilhelm Hübers, DLR Berlin (May 3, 2016): High Resolution Terahertz Spectroscopy with SOFIA

Dr. Sven Eckert, Helmholtz Center Dresden Rossendorf, Germany (May 10, 2016): The interaction between fluid flow and dendritic solidification – research activities at HZDR

Dr. Mierke Schwabe, DLR CP-OP (May 17, 2016): Dusty Plasma Research

Prof. Klaus Kroy, Universität Leipzig (May 18, 2016): Hot Brownian Motion

Prof. Takeshi Egami, University of Tennessee, Knoxville, USA (Jun 1, 2016): Atomistic origin of viscosity in liquids and colloids

Prof. Harald Behrens, Universität Hannover (Jun 7, 2016):

Dr. Christian Karrasch, DLR-MP (Jun 21, 2016): Solidification Kinetics in Undercooled Pure Iron and Iron-Boron Alloys under Different Fluid Flow Conditions

Dr. Philip Born, DLR-MP (Jun 30, 2016): Shining light on dense granular media

Dr. Hui Chen, TU Dortmund (Aug 2, 2016): Enhanced granular medium-based tube press hardening

Prof. Dr. Johann Plank, Construction Chemistry, TU München (Aug 9, 2016): Impact of Mircrogravity on Cement Hydration in the First Seconds

Dr. Denis Schütz, Anton Paar, Graz, Austria (Oct 5): Rheology of Fluidized Granular Matter

Prof. Dr. G. Last, KIT Karlsruhe (Oct 11, 2016): Stationary hard-core models in infinite volume

Dr. Scott Waitukaitis, Leiden University, The Netherlands (Nov 8, 2016): Rabbits, Planets, Volcanos, Dust Devils: The Surprising Physics of Granular Tribocharging

Dr. Konstantinos Boboridis, European Commission Joint Research Centre Karlsruhe (Nov 15, 2016): High-temperature thermophysics of nuclear fuel

Dr. Vincent Martinez, University of Edinburgh (Nov 28, 2016): Studying Soft Matter using Differential Dynamic Microscopy

Dr. Andre Schella, Max-Planck-Institut für Dynamik und Selbstorganisation, Göttingen (Dec 6, 2016): Charged Granular Particles

Prof. Dr. Javier Rodriguez Rodriguez, Universidad Carlos III de Madrid, Spain (Dec 13, 2016): The Physics of Beer Tapping

Prof. Dr. Marco Heinen, Universidad de Guanajuato, Leon, Mexico (Dec 14, 2016): Fractal Liquids

Prof. Dr. Thomas Voigtmann, DLR-MP (Dec 21, 2016): Sampling Chess

3.2 Talks given by institute members

Invited talks of institute members given at international conferences, symposia, and seminars.

Dendritic Growth Kinetics and Solutal Field Evolution Investigated by In-Situ X-Radiography of Al-Ge Alloys
M. Becker; Materials Science and Engineering Congress 2016, Darmstadt, Germany, September 2016.

Scattering with THz radiation
P. Born; Imaging Particles, FAU Erlangen, Erlangen, Germany, April 2016.

Sensitivity of DWS
P. Born; Soft Matter Dynamics Workshop, DLR-MP, Cologne, Germany, September 2016.

Dynamic light scattering from fluidized beds with and without gravity
P. Born; DCF-Seminar, MPI-DS, Gttingen, Germany, September 2016.

Dynamic Light Scattering from Large Particles
P. Born; Nice Optics, Nice, France, October 2016.

Thermophysical properties of high temperature liquid metals and their determination
J. Brillo; Frit-Haber-Institut der Max-Planck-Gesellschaft, Berlin, Germany, March 2016.

Surface tension of binary and ternary alloys
J. Brillo; 11th International Workshop on Subsecond Thermophysics, Krakow, Poland, June 2016.

Density of liquid Ni-Ti and a new optical method for its measurement using two cameras
J. Brillo; 11th Asian Conference on Thermophysical Properties (ACTP), Yokohama, Japan, October 2016.

Undercooling and demixing of liquid Co-Cu alloys under microgravity
J. Brillo; Tohoku-Symposium, Sendai, Japan, October 2016.

Oberflächenspannung flüssiger Al-Au Legierungen
J. Brillo; Arbeitskreis Thermophysik, Austrian Instite of Technology (AIT), Vienna, Austria, April 2016.

Strength of tailored granular media in a gas-fluidized bed
J. Haeberle; CMD 26, Groningen, The Netherlands, September 2016.

Binary Zr-based compounds: ordering, nucleation, dendrite growth, microstructures
D. M. Herlach; TMS Annual Meeting, Michel Rappaz Honorary Symposium on Frontiers in Solidification, Nashville, USA, February 2016.

Undercooled Melts: Ordering, Nucleation, Dendrite Growth, Mirostructure Evolution
D. M. Herlach; KU Leuven, Belgium, November 2016.

Short-range order and solidification behaviour of undercooled metallic melts investigated by diffraction of synchrotron radiation
D. Holland-Moritz; International Workshop Metallurgy with Synchrotrons, Nancy, France, March 2016.

Short-range order and atomic dynamics in undercooled melts
D. Holland-Moritz; ESA TT Solidification EML Meeting, Burg Schnellenberg, Germany, May 2016.

Short-Range Order and Atomic Dynamics in Binary Glass-Forming Alloy Melts
D. Holland-Moritz; Ley Laboratory of Electromagnetic Processing of Materials, Northeastern University, Shenyang, China, September 2016.

Short-Range Order and Atomic Dynamics in Binary Glass-Forming Alloy Melts
D. Holland-Moritz; EMN Meeting on Metallic Glasses, Kuala Lumpur, Malaysia, September 2016.

MAPHEUS – Materialphysikalische Experimente in Schwerelosigkeit
F. Kargl; Vortragsreihe Planetarium am Insulaner, Berlin, February 2016.

Aerodyanmic Levtiation: Thermophysical Properties of Slags
F. Kargl; TT SOL-EML international Workshop, Burg Schnellenberg, May 2016.

In-situ investigation of equiaxed dendrite growth in Al-based alloys employing lab-based X-radiography
F. Kargl; GDR "SAM" Solidification des Alliages Métalliques, Grenoble, France, December 2016.

Quasicrystal nucleation in an intermetallic glass-former
R. Kobold; 16th International Conference on Liquid and Amorphous Metals, Bad Godesberg, Germany, September 2016.

Influence of the levitation technique on measurements of surface tension and viscosity by the oscillating drop method
G. Lohöfer; International Conference on Subsecond Thermophysics, Krakow, Poland, June 2016.

The Benefit of Experiments in Weightlessness
A. Meyer; SKOLTECH, Moscow, Russia, May 2016.

Diffusion of Mass in Multicomponent Alloys
A. Meyer; 12th International Conference on Diffusion in Solids and Liquids, Split, Croatia, June 2016.

Intrinsic Proton Dynamics in Hydrous Silicate Melts as seen by QENS at elevated Temperature and Pressure
A. Meyer; Workshop on 50 Years of Neutron Backscattering Spectroscopy, Munich, Germany, September 2016.

In-situ experiments revealing a structural transition in bulk glass forming metallic liquids
A. Meyer; EMN Meeting on Metallic Glasses, Kuala Lumpur, Malaysia, September 2016.

How Neutron Scattering improves the understanding of liquid alloys and their solidification
A. Meyer; CREMLIN Workshop on Demands of European neutron users in materials science for the instrumentation of the upcoming PIK neutron science centre, Kiel, Germany, September 2016.

Diffusion of Mass in Multicomponent Liquid Alloys
A. Meyer; Materials Science & Technology Conference 2016, Salt Lake City, USA, October 2016.

Experimente in Schwerelosigkeit – Forschen ohne Oben und Unten
A. Meyer; Sternwarte Erkrath, Germany, November 2016.

Structural and dynamical investigations on Hf35Ni65 metallic melts by neutron-scattering
B. Nowak; 16th International Conference on Liquid and Amorphous Metals (LAM-16), Bonn, Germany, September 2016.

Influence of the Chemical Short-Range Order on the Dynamics in Binary Glass-Forming Melts
B. Nowak; MRS Fall Meeting 2016, Boston, USA, November 2016.

Electromagnetic Levitator EML on ISS: Experiment Preparation, Installation and Operation
S. Schneider; TMS 2016, Nashville, USA, February 2016.

Containerless Processing in ISS: Status of Experiments in ESA's EML, the Electromagnetic Levitator
S. Schneider; 67th IAF Congress, Gudalajara, Mexico, September 2016.

Granular Matter(s) in Space
M. Sperl; DLR-IKI Symposium, Munich, Germany, March 2016.

Dense Granular Matter in Low and Zero Gravity
M. Sperl; WE-Heraeus Physics School: Research in Microgravity, Bad Honnef, Germany, July 2016.

Nonlinear Sound Propagation in Granular Packings in Low Gravity
M. Sperl; Workshop on Granular Behavior in Microgravity, Beijing, China, August 2016.

Wave Propagation in Granular Packings in Microgravity
M. Sperl; 3rd International Conference on Packing Problems, Shanghai, China, August/September 2016.

Theory of Multiple Glass States in Simple Liquids
M. Sperl; The 16th International Conference on Liquid and Amorphous Metals (LAM-16), Bonn, Germany, September 2016.

RegoLight, Sintering Regolith with Solar Light
M. Sperl; European Commission Earth Analog workshop, Brussels, October 2016.

3D Printing on th Moon Using Lunar Soil and Solar Radiation
M. Sperl; Werkstoffkolloquium, Cologne, Germany, December 2016.

Wissenschaft ohne Oben und Unten – Experimente in Schwerelosigkeit
M. Sperl; Symposium Institut für Raumfahrtsysteme, Stuttgart, Germany, December 2016.

History Dependence in Soft Glasses
Th. Voigtmann; Keynote lecture, International Congress on Rheology, Kyoto, Japan, August 2016.

Slow Dynamics of Active Particles
Th. Voigtmann; 2nd Workshop on Matter Out of Equilibrium, Guanajuato, Mexico, August 2016.

Slow Dynamics of Active Particles
Th. Voigtmann; CMD 26, Groningen, The Netherlands, September 2016.

History-Dependent Material Properties
Th. Voigtmann; International Soft Matter Conference, Grenoble, France, September 2016.

Nonlinear Response in Crystallization
Th. Voigtmann; International Conference on Nonlinear Response in Complex Matter, Primošten, Croatia, September 2016.

Slow Dynamics of Active Particles
Th. Voigtmann; International Conference on Microswimmers, Bonn, Germany, October 2016.

Combining Scales in Glassy Rheology
Th. Voigtmann; International Conference on Multiscale Modelling of Materials, Dijon, France, October 2016.

Structural and dynamical evolution in binary and ternary La-based glass-forming melts
Z. Wang; The 16th International Conference on Liquid and Amorphous Metals (LAM-16), Bonn, Germany, September 2016.

Thermophysical properties measured by electromagnetic levitation (EML) in comparison with thermodynamic models
J. Wessing; 172nd ISIJ Meeting, Osaka University, Japan, September 2016.

Microscopic dynamics and thermophyical properties of dense metallic melts
F. Yang; The 16th International Conference on Liquid and Amorphous Metals (LAM-16), Bonn, Germany, September 2016.

Dynamics of metallic glass-forming melts dominated by chemical interactions
F. Yang; EMN Meeting On Metallic Glasses, Kuala Lumpur, Malaysia, September 2016.

Influence of Fluid Flow and Iron Intermetallic Phase on the Microstructure of Directional Solidified Al-Si-Cu Alloys
N. Zhang; Junior EUROMAT, Lausanne, Switzerland, July 2016.

3.3 Doktorandenrunde

The PhD students of the institute organize a seminar as part of their graduate program.

Christian Karrasch (Jan 14, 2016): Solidification kinetics in undercooled pure Fe and Fe-B alloy melts under different fluid flow conditions

Sebastian Pitikaris (May 9, 2016): Elastic properties of granular assemblies

Carolina Kreischer (May 9, 2016): Crystallization and transformation in undercooled Fe-Co alloys

Heliana Cárdenas (Jun 30, 2016): Sedimentation of particles in glass forming liquids

Maike Becker (Jun 30, 2016): The effect of solutal field evolution on dendritic growth in Al-Ge alloys observed by X-radiography

Patrick Fopp (Oct 10, 2016): A newly developed aerodynamic-electrostatic Hybrid-Levitator

Benedikt Nowak (Oct 10, 2016): Structural and dynamic investigations on $Hf_{35}Ni_{65}$ metallic melts by neutron-scattering

4 Lecture Courses and Lectures

Physik für Ingenieure (Bauingenieurwesen, UTRM, SEPM)
Ruhr-Universität Bochum, 2 SWS (WS 2015/16)
D. Holland-Moritz

Heterogene Gleichgewichte
RWTH Aachen, 2 SWS (WS 2015/16)
F. Kargl, J. Brillo

Oberseminar Materialphysik im Weltraum
Ruhr-Universität Bochum, 2 SWS (WS 2015/16)
A. Meyer

Stochastic Processes
Heinrich-Heine-Universität Düsseldorf, 4 SWS (WS 2015/16)
Th. Voigtmann

Introduction to X-ray and Neutron Scattering
Ruhr-Universität Bochum, 2 SWS (SS 2016)
D. Holland-Moritz

Theory of Soft Matter
Heinrich-Heine-Universität Düsseldorf, 4 SWS (SS 2016)
Th. Voigtmann

5 Graduations

Bachelor

- Christoph Hansen, *Konstruktion, Aufbau und Inbetriebnahme eines Wirbelbetts zur Granulatfluidisierung*, Hochschule Bonn Rhein Sieg.
- Sarah Carola Nefzger, *Verhaltensänderung von granularen Medien durch Modifikation der Partikeloberfläche*, Hochschule Bonn Rhein Sieg.
- Frederike Schrödel, *Depolarisierte dynamische Lichtstreuung an anisotropen kolloidalen Partikeln*, Uni Bonn.
- Patrick Lehmann, *Anpassungskonstruktion eines Gradientenofens zur Echtzeituntersuchung gerichteter Erstarrung metallischer Schmelzen*, FH Köln.
- Alberto Franck Chiengue Tchapnda, *Entwicklung eines mechatronischen Moduls für eine Höhenforschungsrakete zur Messung der Schallausbreitung in Granulaten mit nichtlinearem Übertragungsverhalten*, Hochschule Bonn Rhein Sieg.
- Tom Schumacher, *Dichteanalyse von flüssigen Ni-Ti Legierungen mit Hilfe der elektromagnetischen Levitation mittels einer neuen Messmethode*, TH Köln.

Diploma and Master

- Helen Margaux Bachmann, *Untersuchungen zur Mikrostruktur eutektischer CoSi-Legierungen aus der unterkühlten Schmelze*, Hochschule Osnabrück.
- Steffen Behnert, *Implementierung und Validierung eines Magnetfelderzeugers an einem Isothermalofen*, TH Köln.
- Andreas Hollmann, *Thermophysikalische Eigenschaften von levititerten CaO-MgO-SiO2 Schmelzen*, Universität Hannover.
- Dennis Brüggemann, *Untersuchungen von unterkühlten Metallschmelzen durch Beugungstechniken*, Ruhr-Universität Bochum.
- Alex Kamphuis, *Non-Linear Wave Propagation in Granular Media*, University of Twente.
- Lucien Barad, *Development of a process for 3D printing by SLM (Selective Laser Melting) of a ceramic powder (regolith) for lunar applications*, EEIGM.
- Marie Pedrazzani, *Influence of thermal cycling on sintered lunar regloith*, EEIGM.
- Romain Marchant, *Feasibility study on solvent cast 3D printing for space applications*, EEIGM.
- Olfa Lopez, *Development of powder-based 3D printer for space applications*, EEIGM.
- Mareike Wegener, *Mikrostruktur unterkühlter und erstarrter eutektischer Ni-Sn Legierungen*, RWTH Aachen.
- Marissa Seidel, *Mass transport in ternary Zr-Ni-Al Alloys*, Westfälische-Wilhelms-Universität Münster.

PhD Theses

- Christian Karrasch, *Solidification Kinetics in Undercooled Pure Iron and Iron-Boron Alloys under Different Fluid Flow Conditions*, Ruhr-Universität Bochum.
- Raphael Kobold, *Crystal growth in undercooled melts of glass forming Zr-based alloys*, Ruhr-Universität Bochum.

6 Awards

- Maike Becker, price for best student and post-doc poster, International Conference on Multiscale Materials Modelling, Dijon
- Olfa Lopez, 1st prize in the competition "Les Entrepreneuriales en Lorraine"
- Olfa Lopez, 1st prize in the competition "Génération Développent Durable" (organized by ANALE, La Recherche, and the French Ministry of National Education and Research)
- Olfa Lopez, 1st prize "Entreprendre 2016"
- Olfa Lopez, 2nd prize in the competition "Creativ'Est" (organized by Science Politiques)

7 Fellows

Visiting fellows at the institute:

- Stefan Burggraf: Ruhr-Universität Bochum (2013–2017)
- Dr. Luis Fernando Elizondo Aguilera: DLR-DAAD postdoctoral fellow (2015–2017)
- Dr. Ali Kaouk: DLR-DAAD postdoctoral fellow (2016–2017)
- Dr. Christian Karrasch: Ruhr-Universität Bochum (2012–2016)
- William King: University of Alberta, Canada (5/2016–12/2016)
- Dr. Nishant Kumar: DLR-DAAD postdoctoral fellow (2016–2017)
- Olfa Lopez: DLR-DAAD PhD fellow (2016–2019)
- Dr. Nafiseh Masoumzadeh Jouzdani: DLR-DAAD postdoctoral fellow (2016–2017)
- Prof. Douglas Matson: Tufts University, USA (3/2016–8/2016)
- Alexandre Meurisse: DLR-DAAD PhD fellow (2015–2017)
- Dr. Hideyuki Mizuno: DLR-DAAD postdoctoral fellow (2014–2016)
- Dr. Hailong Peng: Ruhr-Universität Bochum (2015–2016)
- Dr. Yuriy Plevachuk: DLR-DAAD fellow (2016)
- Dr. Zheng Wang: DLR-DAAD postdoctoral fellow (2015–2017)
- Dr. Anoosheh Yazdi: DLR-DAAD postdoctoral fellow (2016)
- Nannan Zhang: DLR-DAAD PhD fellow (2014–2017)
- Dandan Zhao: Northeastern University Shenyang (2016–2018)

8 Visits

Longer visits of institute members to other institutions:

- Elke Sondermann: University of Newcastle, Australia (September–October 2016)
- Johanna Wessing: Tohoku University Sendai, Japan (August–November 2016)

9 Events and Campaigns

- Sino-German Drop Tower Campaign, January 2016: granular gas experiment.
- 28th DLR Parabolic Flight Campaign, March 2016: granular sound experiment, electrostatic levitation GOLD-ESL, and 3D-printing experiment.
- International Space Station (ISS), EML Batch 1.2b experiments, April–June 2016
- Drop Tower Campaign, July 2016: gas–liquid separation
- International Space Station (ISS), EML Batch 1.2c experiments, October–December 2016
- Frequent measurement campaigns at Forschungsneutronenquelle Heinz-Maier-Leibnitz (FRM II), Garching, TU München: Neutron time-of-flight spectrometer ToF-ToF and neutron radiography beamline ANTARES.
- Frequent measurement campaigns at Institut Lauge-Langevin (ILL), Grenoble, France: High flux neutron diffractometer D20, neutron time-focussing time-of-flight spectrometer IN6, and small momentum transfer diffractometer D16.
- Frequent measurement campaigns at the European Synchrotron Radiation Facility (ESRF), Grenoble, France: Materials science beamline ID15.
- Measurement campaigns at Hasylab, DESY Hamburg: USAXS beamline BW4.

10 Workshops organized by the institute

Glastag (DLP-MP, 4/5 April 2016)

A traditional meeting of researchers working on the dynamics of amorphous materials and melts, held annualy. The 2016 event was organized by Matthias Sperl jointly with the DFG Research Unit FOR 1394 "Nonlinear Response to Probe Vitrification". The members of the Research Unit presented their work, in addition to international guests with invited talks. After the Glastag, a school for young researchers was held, with a lecture by Fan Yang from the institute.

Mauro Sellitto, ICTP Trieste, Italy: Cooperative facilitation dynamics

Andreas Meyer, DLR-MP: Liquid-liquid transitions in metallic melts

Jin Sun, University of Edinburgh, UK: Shear thickening of dense suspensions – mechanisms, flow regimes and polydispersity

Stefan Luding, University of Twente, The Netherlands: Granular Rheology and Jamming

Matthias Krüger, MPI f. Komplexe Systeme, Stuttgart: Frenetic Aspects of Second Order Response

16th International Conference on Liquid and Amorphous Metals (Bonn Bad Godesberg, September 4–9, 2016)

LAM is a longstanding cycle of major conferences in the field that was started in 1966. The 2016 event was organized by Dirk Holland-Moritz and Florian Kargl from the institute, with financial support from Deutsche Forschungsgemeinschaft (DFG). The conference attracted 138 participants.

The conference aims to provide a forum for scientists interested in liquid and amorphous metals in order to discuss recent advances and future directions in this intriguing field of condensed matter physics, chemistry and materials sciences. Apart from papers on metallic systems, the LAM conferences traditionally also welcome contributions on liquid and amorphous semi-conductors as well as on molten salts. Invited and plenary (boldface) talks were:

Jürgen Eckert, Erich Schmid Institute of Materials Science, Leoben, Austria: Tailoring structure formation and properties of glass-forming systems

Takeshi Egami, University of Tennessee, Knoxville, USA: Atomistic origin of viscosity in liquids

Lindsay Greer, University of Cambridge, Cambridge, UK: New perspectives on glasses and glass formation from liquids

Frans Spaepen, Harvard University, SEAS, Cambridge MA, USA: How Liquids and Glasses Came Into Their Own

Cynthia A. Volkert, University of Göttingen, Germany: Early Plasticity in Metallic Glasses

Chrisitane Alba-Simionesco, Laboratoire Léon Brillouin, Saclay, France: The glass formation: a very local structural event

Sven Eckert, Helmholtz-Zentrum Dresden-Rossendorf, Germany: Electromagnetic control of liquid metal flows and solidification processes

Adriano Filipponi, Università degli Studi dell'Aquila, L'Aquila, Italy: The structure of liquid metals probed by X-ray absorption spectroscopy

Jianrong Gao, Northeastern University, Shenyang, China: Liquid-liquid decomposition and rapid solidification of undercooled Co-Cu melts under high magnetic fields

Annett Gebert, IFW Dresden, Germany: Electrochemical properties of metallic glasses and related composites

Jeong Sook Ha, Korea University, Seoul, Korea: Liquid metal for stretchable devices

Louis Hennet, CEMHTI-CNRS UPR3079, Orléans, France: Levitation techniques: 20 years of experiments at synchrotron and neutron sources

Masanori Inui, Hiroshima University, Hiroshima, Japan: Structure of liquid metals disentangled by inelastic X-ray scattering

Jian-Zhong Jiang, Zhejiang University, Zhejiang, China: Atomic structure evolution in metallic melts

Hidemi Kato, Tohoku University, Sendai, Japan: High aspect grating by imprinting metallic glasses with less viscous workability

Pavel R. Levashov, Joint Institute for High Temperatures of the Russian Academy of Science, Moscow, Russia: Quantum simulation of liquid metals: predicted properties and problems

Haozhe Liu, Harbin Institute of Technology, Harbin, China: Metallic glass under compression: Searching for "universal" behavior patterns using synchrotron X-ray techniques

Kazuhiro Matsuda, Kyoto University, Kyoto, Japan: Inelastic X-ray scattering study on the electronic state in fluid alkali metals

Alexander Mayer, Chelyabinsk State University, Chelyabinsk, Russia: Atomistic and continuum modeling of dynamic tensile fracture of metal melts

Genri Norman, Joint Institute for High Temperatures of the Russian Academy of Science, Moscow, Russia: Two glass transitions in liquid metals - Molecular modelling

Yuriy Plevachuk, Ivan Franko National University, Lviv, Ukraine: Influence of nanoparticle admixtures on thermophysical and mechanical properties of lead-free solder alloys

Annie Pradel, Institut Charles Gerhardt UMR 5253, Montpellier, France: Telluride glasses and amorphous films: structural investigation and potential applications

Maria Dolores Ruiz-Martín, Universitat Polytècinica de Catalunya, Barcelona, Spain: Structure and dynamics of Zr2Co melts

Junji Saida, Tohoku University, Sendai, Japan: Structural rejuvenation with the change of mechanical properties in Zr-based metallic glass by post annealing

Ari Paavo Seitsonen, Ècole Normale Supérieure, Paris, France: Investigation of dynamics and structure in liquid (alkali) metals via density functional theory-based molecular dynamics

Fuyuki Shimojo, Kumamoto University, Kumamoto, Japan: Ab initio molecular-dynamics study of structural and dynamic properties of disordered materials

Philipp Sperling, SLAC, Menlo Park, USA: Free-electron X-ray measurements of collisional-damped plasmons in isochorically heated warm dense matter

Peter Švec, Slovak Academy of Sciences, Bratislava, Slovakia: Structure-property relationship in rapidly quenched alloys correlated with melt precursor processing

Jean-François Wax, LPMD, Université Paul Verlaine, Metz, France: Analyzing the dynamic structure of liquid metals and alloys

Fan Yang, DLR-MP: Microscopic dynamics and thermophyical properties of dense metallic melts

Soft Matter Dynamics (DLR-MP, September 2016)

Philip Born from the institute together with Marco Baribanti organized this workshop on granular materials in space, with 21 participants from 7 countries.

Marco Braibanti, ESA, Noordwijk, The Netherlands: Soft Matter Dynamics: Granular Materials investigations

Nicolas Vandewalle, University of Liege, Belgium: Vibration induced phenomena in granular matter

Matthias Sperl, DLR-MP: Research at DLR-MP in Cologne

Reinhard Höhler, Université Pierre et Marie Curie Paris, France: Optical Diagnostics test of the Soft Matter Dynamics hardware

Jérôme Crassous, Université de Rennes, France: Models for light scattering in granular materials

Stefan Luding, Universiteit Twente, The Netherlands: Simulation of Granular Media

Philip Born, DLR-MP: Sensitivity of DWS

Jérôme Crassous, Université de Rennes, France: Measuring ℓ^*

Stefan Luding, Universiteit Twente, Netherlands: Agitation methods for granular media

Mathias Schröter, FAU Erlangen, Germany: Control of particle interactions

Vipgran ESA Topical Team Meeting (DLR-MP, September 2016)

Philip Born from the institute and Nicolas Vandewalle organized this topical-team meeting with 10 participants from 4 countries.

Olivier Minster, ESA, Noordwijk, The Netherlands: Status of VIPGRAN

Nicolas Vandewalle, University of Liege, Belgium: Results of PFC64

Peidong Yu, DLR-MP: Shock-wave propagation measurement in low gravity

Mathias Schröter, FAU Erlangen, Germany: Shear cell for VIPGRAN

Nicolas Vandewalle, University of Liege, Belgium: Moving wall for VIPGRAN

Eric Falcon, University of Liege, Belgium: PFC65 parameters, Transfer of VIPGRAN to Bordeaux

PhD Student Day (Doktorandentag, DLR-MP, December 8, 2016)

The PhD students working at the institute presented their ongoing work and discussed their progress and their working conditions with the Institute Director.

Tina Gläsel, DLR-MP: Investigation of the properties of liquid-solid-interfaces at high temperatures

Bernard Baptista da Cunha, DLR-MP: Thermophysical properties of liquid magnetic shape memory alloys

Johanna Wessing, DLR-MP: Thermophysical properties of liquid Al-Ti alloys

Patrick Fopp, DLR-MP: News from HÆL

Mareike Wegener, DLR-MP: Morphological transition in Al based alloys observed with in-situ X-ray radiography

Maike Becker, DLR-MP: Solidification kinetics in Al-Cu and Al-Ge alloys investigated by in-situ X-ray radiography

Carolina Kreischer, DLR-MP: Crystallization and transformation of the metastable phase in FeCo-alloys

Benedikt Nowak, DLR-MP: Influence of the Chemical Short-Range Order on the Dynamics in Binary Glass-Forming Melts

Sarah Zimmermann, DLR-MP: Relation between self-diffusion and viscosity in Ni66.7B33.3 in comparison to other dense liquids

Heliana Cárdenas, DLR-MP: Fluidity model for glass forming liquids

Alexander Liluashvili, DLR-MP: Active Microrheology of Dense Microswimmer Suspensions

Jonathan Ónody, DLR-MP: Dense microswimmer systems in model porous media

Karsten Tell, DLR-MP: Wave Propagation in Granular Packings

Sebastian Pitikaris, DLR-MP: Mechanical Properties of 2D Granular Packings

Jan Haeberle, DLR-MP: Triboelectric Charging of Surface-treated Granular Media

Olfa Lopez, DLR-MP: Handling and 3D printing granular matter in microgravity

Alexandre Meurisse, DLR-MP: Sintering lunar regolith

11 Third-Party Funding

European Space Agency (ESA) – AO 1999, selected flight experiments

Microstructure formation in casting of technical alloys under diffusive and magnetically controlled convective conditions (MICAST)
L. Ratke, coordinator; G. Müller (D); Y. Fautrelle (F); M. D. Dupony (F); A. Roosz (HUN); G. Zimmermann (D); J. Lacaze (F)
rated *excellent*

Metastable Solidification of Composites: Novel Peritectic Structures and In-Situ Composites (METCOMP)
M. Kolbe, coordinator; G. Eggeler (D); L. Granaszy (HUN); **D. M. Herlach**; A. Ludwig (A); M. Rappaz (CH)
rated *excellent*

High Precision Thermophysical Property Data of Liquid Metals for Modelling of Industrial Solidification Processes (THERMOLAB)
H. J. Fecht, coordinator (D); L. Battezzati (I); **J. Brillo**; A. Passerone (I); E. Ricci (I); S. Seetharaman (S); R. Aune (S); J. Etay (F)
rated *outstanding*

Study and modelling of nucleation and phase selection phenomena in undercooled melts: Application to hard magnetic alloys of industrial relevance (MAGNEPHASE)
W. Löser, coordinator (D); L. Granasy (HUN); R. Hermann (D); **D. Holland-Moritz**; **T. Volkmann**; J. Fransaer (B); rated *very good*

Solidification along a Eutectic Path in Ternary Alloys (SETA)
S. Rex, coordinator (D); L. Froyen (B); G. Faivre (F); H. Nguyen-Thi (F); **L. Ratke**
rated *excellent*

Thermophysical Properties of Liquid Metals for Industrial Process Design (ThermoProp)
H.-J. Fecht, coordinator (D); R. Wunderlich (D); L. Battezzati (I); **J. Brillo**; J. Etay (F); E. Ricci (I); S. Seetharaman (S)
consolidation of ESA MAP project AO 1999, 2004, and 2009 – rated *outstanding*

European Space Agency (ESA) – AO 2000, selected flight experiments

Investigations of thermophysical properties of Si in the melt and in the undercooled state under microgravity conditions (SEMITHERM)
K. Samwer, coordinator (D): B. Damaschke (D); **J. Brillo**; E. Ricci (I); E. Arato (I); T. Hibiya (JPN); W. von Ammon (D); T. Tsukuda (JPN); T. Fuhiwara (JPN)
rated *very good*

Magnetohydro-dynamics of levitated drops
R. Wunderlich, coordinator (D); G. Gerbeth (D); **I. Egry**; J. Priede (LV); J. Etay (F); Y. Fautrelle (F)
rated *very good*

European Space Agency (ESA) – AO 2004, selected flight experiments

In-situ X-ray Monitoring of Advanced Metallurgical Processes under Microgravity and Terrestrial Conditions (XRMON)
R. H. Mathiesen, coordinator (N); G. Zimmermann (D): H. Nguyen-Thi (F); L. Froyen (F); **M. Kolbe/F. Kargl**; C.-A. Gandin (F); D. Browne (IRL); F. García-Moreno (D)
rated *excellent*

Chill Cooling for the Electro-Magnetic Levitator in Relation with Continuous Casting of Steel (CCEMLCC)
C.-A. Gandin, coordinator (F); **D. M. Herlach**; **T. Volkmann**; V. Uhlenwinkel, H. Henein, D. Juul Jensen (DK); M. Kallio, F. Costes, M. Bobadilla
rated *excellent*

Non-equilibrium multiphase transformations: eutectic solidification, spinoidal decomposition and glass formation (MAGNEPHASE)
P. Galenko, coordinator; **D. M. Herlach**; R. Parfeniev (RUS); B. Melekh (RUS); M. Volkov (RUS); A. Ivanov (RUS)
rated *excellent*

Electrical Resistivity measurements of high temperature metallic melts (RESISTIVITY)
G. Lohöfer, coordinator; G. Pottlacher (A)
rated *excellent*

European Space Agency (ESA) – AO 2009, selected flight experiments

Thermophysical properties of liquid metallic alloys – modelling of industrial solidification processes and development of advanced products (THERMOLAB – ISS)
H.-J. Fecht, coordinator (D); L. Battezzati (I); **J. Brillo**; A. Dommann (CH); U. Erb (CDN); J. Etay (F); H. Fukuyama (JPN); T. Hibiya (JPN); R. Hyers (USA); T. Ishikawa (JPN); J. Z. Jiang (CHN); K. Kelton (USA); G. W. Lee (ROK); W. Lojkowski (PL); I. Manna (IND); D. Matson (USA); S. Ozawa (JPN); K. Pericleous (UK); E. Ricci (I); S. Seetharaman (S); T. Tanaka (JPN); R. Valiev (RUS); M. Watanabe (JPN); R. Wunderlich (D)

rated *outstanding*

Thermophysical properties and solidification behaviour of undercooled Ti-Zr-Ni liquids showing an icosahedral short-range order (ICOPROSOL)
D. Holland-Moritz, coordinator; R. Hyers (USA); K. Kelton (USA); **G. Lohöfer**
rated *excellent*

Gravity dependence of CET in peritectic TiAl alloys (GRADECET)
U. Hecht, coordinator (D); D. Daloz (F); L. Gránásy (HUN); A. Griesche (D); J. Lapin (SK); S. McFadden (IRL); **A. Meyer**; M. Rebow (PL); L. Sturz (D); G. Tegze (HUN); M. Zaloznik (F)
rated *excellent*

Thermophysical properties of liquid alloys under oxygen influence (OXYTHERM)
J. Brillo, coordinator; E. Arato (I); H. Fritze (D); H. Fujii (JPN); L. Hennet (F); G. Kaptay (HUN); R. Novakovic (I); S. Ozawa (JPN); E. Ricci (I); M. Watanabe (JPN)
rated *excellent*

Peritectic alloy rapid solidification with electromagnetic convection (PARSEC)
T. Volkmann, coordinator; J. Fransaer (B); R. Hyers (USA); M. Krivilev (RUS); W. Löser (D); D. Matson (USA); K. Pericleous (UK)
rated *excellent*

Liquid phase separation in metallic alloys (LIPHASE)
M. Kolbe, coordinator; L. Battezzati (I); **J. Brillo**; D. Chatain (F); S. Curiotto (F); J. Gao (CHN); H. Yasuda (JPN)
rated *excellent*

Compaction and Sound Transmission in Dense Granular Media (COMPGRAN)
M. Sperl, coordinator; R. Behringer (USA); E. Clement (F); S. Luding (NL); M. Schroeter (D)
rated *excellent*

Influence of diffusive and convective mass transport on microstructure formation in Al-based alloys (DIFFSOL)
A. Griesche, coordinator (D); H. Emmrich (D); **J. Horbach**; G. Kaptay (HUN); **A. Meyer**; B. Nestler (D); H. Nguyen-Thi (F); Y. Fautrelle (F); X. Ruiz (E); Z. Saghir (CDN); V. M. Shevtsova (B); R. Siquieri (D); **T. Voigtmann**; G. Zimmermann (D)
rated *very good*

Non-equilibrium solidification, modelling for microstructure engineering of industrial alloys (NEQUISOL III)
D. M. Herlach, coordinator; U. Fritsching (D); C.-A. Gandin (F); H. Henein (CDN); V. Uhlenwinkel (D)
rated *very good*

Liquid phase diffusion in semiconductors (LIPIDIS)
S. Dost, coordinator (CDN); B. Lent (CDN); T. Masaki (JPN); **A. Meyer**; **F. Kargl**; B. Nestler (D); Z. Saghir (CDN); A. Senchenkov (RUS); H. Struchtrup (CDN); D. Vizman (ROM); A. Croll (D); E. Dieguez (E); T. Duffar (F); A. Egorov (RUS)
rated *very good*

Gravitational effects on heat and mass transport phenomena in directional solidification of upgraded metallurgical silicon for photovoltaic applications (SISSI)
T. Duffar, coordinator (F); J. Friedrich, coordinator (D); J. Baruchel (F); M. Bellmann (N): S. Binetti (I); T. Carlberg (S); A. Croll (D); J. Derby (USA); E. Dieguez (E); S. Dost (CDN); F. Dupret (B); H. Emmerich (D); A.-J. Faber (NL); C.-A. Gandin (F); J.-P. Garandet (F); M. Gonik (RUS); **A. Meyer**; **F. Kargl**; K. Kakimoto (JPN); N. Mangelinck (F); W. Miller (D); B. Nestler (D)
rated *outstanding*

Soft Matter Dynamics
M. Sperl (coordinator), D. Langevin (F); R. Hohler (F); R. Miller (D); L. Liggieri (IT)
rated *excellent*

ESA Topical Teams

Atomic Transport in Liquids and Semiconductors (ATLAS)
A. Griesche, coordinator (D); **A. Meyer**; J.-P. Garandet (F); Z. Saghir (CDN); W. Miller (D); W. Wołczyński (PL); A. Mialdun, D. Melnikov, I. Ryzhkov, V. Shevtsova, S. Van Vaerenbergh (B); J. Agren (S); J. Friedrich (D); F. Faupel (D); H. Emmerich (D); B. Nestler (D); G. Wilde (D)

Solidification of Containerless Undercooled Melts SOL–EML
D. M. Herlach (coordinator), **P. Galenko, D. Holland-Moritz, M .Kolbe, T. Volkmann**; J. Fransaer (B); G. Phanikumar (IND); Ch.-A. Gandin (F); J. Gao, L. Granasy (HUN); H. Henein (CDN); R. W. Hyers (USA); K. F. Kelton (USA); W. Löser (D); D. M. Matson, T. Okutani (JPN): K. Pericleous (UK); M. P. Volkov (RUS); H. Yasuda (JPN)

Space Grains
E. Falcon, coordinator (F); S. Aumaître (F); R. Behringer (USA); M. Berhanu (F); E. Clément (F); J. Crassous (F); D. Durian (USA); P. Evesque (F); S. Fauve (F); A. Garcimartin (E); Y. Garrabos (F); M. Hou (CHN); X. Jia (F); C. Lecoutre (F); F. Ludewig (B); S. Luding (NL); S. Merminod (F); E. Opsomer (B); D. Ozcodi (E); M. Schroeter (D); **M. Sperl**; R. Stannarius (D); N. Vandewalle (B); **P. Yu**

ESA User Support

MSL-LGF and MSL-SQF Experiment Preparation and Operations Support
S. Steinbach (2006–2011)

Support of TEMPUS/EML Parabolic flight and TEXUS campaigns
S. Schneider (2015–2016)

FRC Support for Columbus Multi User Facilities, USOC Implementation and Operations, EML
S. Schneider

FRC Support for Columbus Multi User Facilities, USOC Implementation and Operations, MSL
S. Steinbach

FRC Support for Columbus Multi User Facilities, USOC Implementation and Operations, TEMPUS 24
D. Heuskin

FRC Support for Columbus Multi User Facilities, USOC Implementation and Operations, TEMPUS 25
S. Klein

Industry

Herstellung Öfen (Graphit, Al2O3) mit Flugproben für MAXUS-9
F. Kargl (SSC; 2014–2016)

Density measurements of binary allloys
J. Brillo (Japanische Stahlindustrie; 2015–2016)

European Union

RegoLight – Sintering Regolith with Solar Light
M. Sperl; Space Application Services (B); Liquifier Systems Group (A); Comex S.A. (F); Bollinger (A) (2015–2017)

Bundesministerium für Bildung und Forschung (BMBF)

Verbundvorhaben Magnetische Aktormaterialien mit reduziertem Gallium-Anteil (MAREGA), Teilvorhaben Thermophysikalische Eigenschaften Magnetischer Ga-reduzierter Formgedächtnislegierungen
J. Brillo (2016–2019)

Verbundvorhaben Klimaschutz, Teilvorhaben 2: Direkteinspritzventilentwicklung (MULTDIRIN)
D. Neuhaus (2016–2017)

Deutsche Forschungsgemeinschaft (DFG)

Nonlinear mechanical response of supercooled melts under applied stress
Th. Voigtmann; M. Fuchs, Universität Konstanz
Project in the Research Unit FOR1394: Nonlinear Response to Probe Vitrification (2010–2013; renewed 2013–2016)

Slow dynamics in homogeneously driven granular systems
M. Sperl; A. Zippelius, Universität Göttingen
Project in the Research Unit FOR1394: Nonlinear Response to Probe Vitrification (2010–2013; renewed 2013–2016)

Electrostatic levitation investigation of the temperature rheological and volumetric changes of Molten Zr-based bulk metallic glass forming alloys
A. Meyer; R. Busch, Universität Saarbrücken (2012–2015; renewed 2015–2018)

Crystal growth velocity in deeply undercooled melts of pure Zr and glass forming Zr-based alloys
D. M. Herlach; B. Nestler, KIT; R. Liu, Yanshan University, Qinhuangdao, China (2013–2016)

Active microrheology of dense microswimmer suspensions
Th. Voigtmann (2014–2017)

Presshärten von Rohren durch granulare Medien
P. Born, M. Sperl; A. E.Tekkaya, Universität Dortmund (2014–2017)

Other

FixDust Herstellung von Proben für Spulenbedampfungsprojekt der ESA
S. Klein (Universität Konstanz, 2014–2016)

Knudsen-EML
S. Klein, D. Heuskin (TU Clausthal, 2016)

12 Author Index

Page numbers in **bold face** indicate corresponding authors. Page numbers in *italic type* indicate coauthors. Authors affiliated with the institute appear in **bold face**.

DLR at a glance

DLR is the national aeronautics and space research centre of the Federal Republic of Germany. Its extensive research and development work in aeronautics, space, energy, transport and security is integrated into national and international cooperative ventures. In addition to its own research, as Germany's space agency, DLR has been given responsibility by the federal government for the planning and implementation of the German space programme. DLR is also the umbrella organisation for the nation's largest project management agency.

DLR has approximately 8000 employees at 20 locations in Germany: Cologne (headquarters), Augsburg, Berlin, Bonn, Braunschweig, Bremen, Bremerhaven, Dresden, Goettingen, Hamburg, Jena, Juelich, Lampoldshausen, Neustrelitz, Oberpfaffenhofen, Oldenburg, Stade, Stuttgart, Trauen, and Weilheim. DLR also has offices in Brussels, Paris, Tokyo and Washington D.C.

Institute of Materials Physics in Space

Research at DLR's Institute of Materials Physics in Space is devoted to the exploration of the fundamental mechanisms that underly liquid properties and solidification processes. Through the absence of gravitationally driven phenomena, like convection and sedimentation, investigations in weightlessness provide well-defined experimental conditions. This enables accurate measurements that allow for a benchmarking of simulation and theory, as well as a parametrization and a further development of earth-bound experiments. Embedded in a closely associated and strong ground based program with simulation, theory and experiments, the institute's research in space comprises key experiments towards an understanding of the physical mechanisms involved. This in turn forms the basis for a quantitative description of solidification processes and a computer assisted materials design from the melt.

DLR **Deutsches Zentrum für Luft- und Raumfahrt** e.V.
in der Helmholtz-Gemeinschaft

Institut für Materialphysik im Weltraum
51170 Köln

www.dlr.de/mp
e-mail: materialphysik@dlr.de